MECHANICS OF NANOSCALE BEAMS IN LIQUID ELECTROLYTES:

BEAM DEFLECTIONS, PULL-IN INSTABILITY, AND STICTION

A Dissertation

by

JAE SANG LEE

Submitted to the Office of Graduate Studies of
Texas A&M University
in partial fulfillment of the requirements for the degree of

DOCTOR OF PHILOSOPHY

December 2008

Major Subject: Aerospace Engineering

MECHANICS OF NANOSCALE BEAMS IN LIQUID ELECTROLYTES:

BEAM DEFLECTIONS, PULL-IN INSTABILITY, AND STICTION

A Dissertation

by

JAE SANG LEE

Submitted to the Office of Graduate Studies of
Texas A&M University
in partial fulfillment of the requirements for the degree of

DOCTOR OF PHILOSOPHY

Approved by:

Chair of Committee,	James G. Boyd IV
Committee Members,	Dimitris C. Lagoudas
	Zoubeida Ounaies
	Won-Jong Kim
Head of Department,	Helen L. Reed

December 2008

Major Subject: Aerospace Engineering

ABSTRACT

Mechanics of Nanoscale Beams in Liquid Electrolytes: Beam Deflections, Pull-in

Instability, and Stiction. (December 2008)

Jae Sang Lee, B.S., Seoul National University;

M.S., Texas A&M University

Chair of Advisory Committee: Dr. James G. Boyd IV

The pressure between two parallel planar surfaces at equal electric potentials is derived

using the modified Poisson-Boltzmann (MPB) equation to account for finite ion size.

The effects of finite ion size are presented for a z:z symmetric electrolyte and compared

with the pressure derived by the classical Poisson-Boltzmann (PB) equation.   The

pressures predicted by the two models differ more as the bulk ion concentration, surface

potential, and ion size increase. The ratio of the pressures predicted by the two models is

presented by varying the ion concentration, surface potential, ion size and distance of

separation. The ratio of pressures is relatively independent of the distance of separation

between the two surfaces.

An elastic beam suspended horizontally over a substrate in liquid electrolyte is

subjected to electric, osmotic, and van der Waals forces. The continuous beam structure,

not a discrete spring, which is governed by four nondimensional parameters, is solved

using the finite element method. The effects of ion concentration and electric potentials

to the pull-in instability are especially focused by parametric studies with a carbon

nanotube cantilever beam. The pull-in voltage of a double-wall carbon nanotube suspended over a graphite substrate in liquid can be less than or greater than the pull-in voltage in air, depending on the bulk ion concentration. The critical separation between the double-walled carbon nanotube (DWCNT) and the substrate increases with the bulk ion concentration. However, for a given bulk ion concentration, the critical separation is independent of the electric potentials. Furthermore, the critical separation is approximately equal in liquid and air.

Stiction, the most common failure mode of the cantilever-based devices, is studied in a liquid environment, including elastic energy, electrochemical work done, van der Waals work done and surface adhesion energy. We extend the classical energy method of the beam peeling for micro-electro-mechanical systems (MEMS) in the air to an energy method for nano-electro-mechanical systems (NEMS) in liquid electrolyte. We demonstrate a useful numerical processing method to find the parameters to free the stiction of the beams and to obtain the detachment length of the beams.

DEDICATION

To my parents, sisters, friends, JIVE, tjdud and allornon.

TABLE OF CONTENTS

LIST OF FIGURES

FIGURE   Page

FIGURE   Page

LIST OF TABLES

1. INTRODUCTION

1.1. Background

This dissertation concerns nanomachines ranging in size from several nanometers to several hundred nanometers, operating in liquid electrolytes. Figure 1 depicts the status, by scale, of micro and nano engineering [1]. Note that there is a region between several nanometers and several hundred nanometers that is not supported by a well-developed state-of-the-art in engineered devices. Molecular machines smaller than several nanometers using a bottom-up approach are the subject of intense research. At a larger scale, Micro Electromechanical Systems (MEMS) using a top-down approach are now a well-understood subject. In contrast, very little research has been done to design, fabricate, and test machines from several nanometers to several hundred nanometers to operate in liquid electrolytes.

There are many applications of nanotechnology that require nanocomponents to be placed in liquid electrolytes, either in packaging the components before use, in service, or both. Indeed, the wet-dry interface is a fundamental aspect of bio-nano technology.

Obvious applications include: (1) Body fluids are typically 0.1M ionic solutions, mainly NaCl and KCl. (2) Water always contains some concentrations of H^+ and OH^- ions. (3) Single walled carbon nanotubes (SWCNT) are supplied as colloidal dispersions in ionic liquids. (4) Some concepts for making SWCNT electronic circuits

_____
This dissertation follows the style of *Journal of Micromechanics and Microengineering*.

require that the SWCNTs be positioned and attached in the liquid phase.
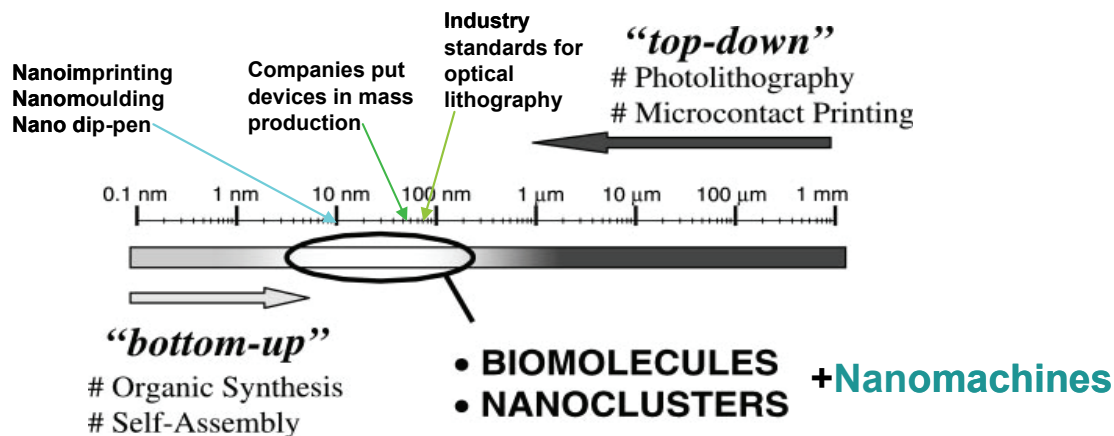
Figure 1. The gap that currently exists in the engineering of small-scale devices [1]

(5) Mechano-chemistry concepts use nanomachines to manipulate macromolecules such as dendrimers and proteins and serve as "active" catalysts that bring reactants together in configurations that do not naturally occur with high frequency in solution. (6) Nanostructured electrochemical devices include fuel cells, batteries, supercapacitors, hydrogen storage, electroactive polymer actuators, and devices using electrophoresis, electroosmosis, or electrocapillarity. (7) Nanodevices are sometimes processed using wet etching. (8) Finally, individual nanodevices must be packaged, often in liquids.

Micro and nanofabrication processes are planar technologies. Therefore, many micro and nano devices consist of beams and plates suspended horizontally over a substrate. On the microscale, suspended beams or plates serve as the active component of accelerometers, rate gyroscopes, pressure sensors, chemical sensors, electrical switches, optical switches, adaptive optical devices, resonators, electrostatic actuators,

valves, and pumps as shown in Figures 2-9. It is reasonable to assume that suspended

beams will play a similarly important role on the nanoscale [2].

(a)   (b)
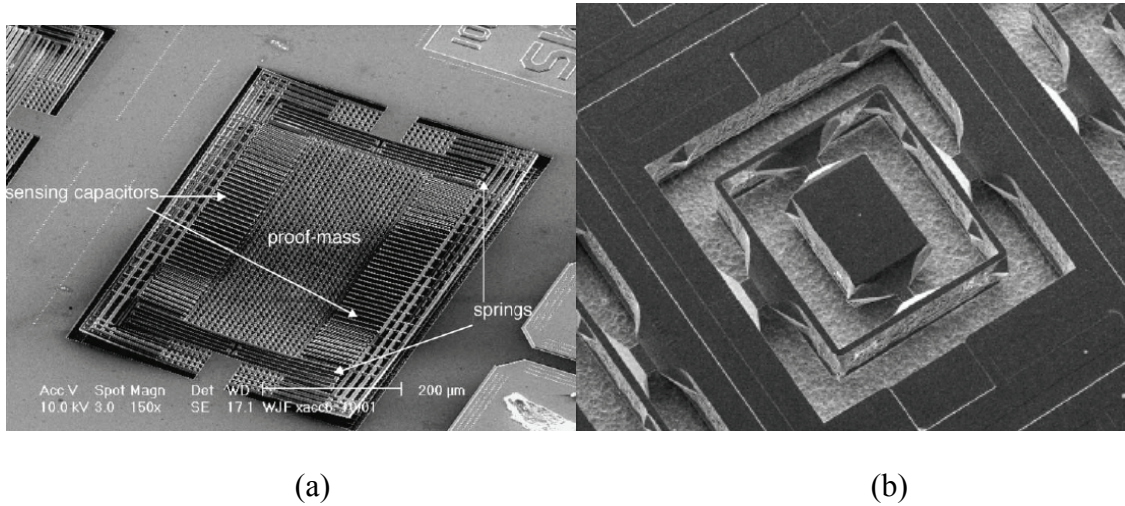
Figure 2. (a) Accelerometer [3], (b) gyroscope [4]

(a)   (b)
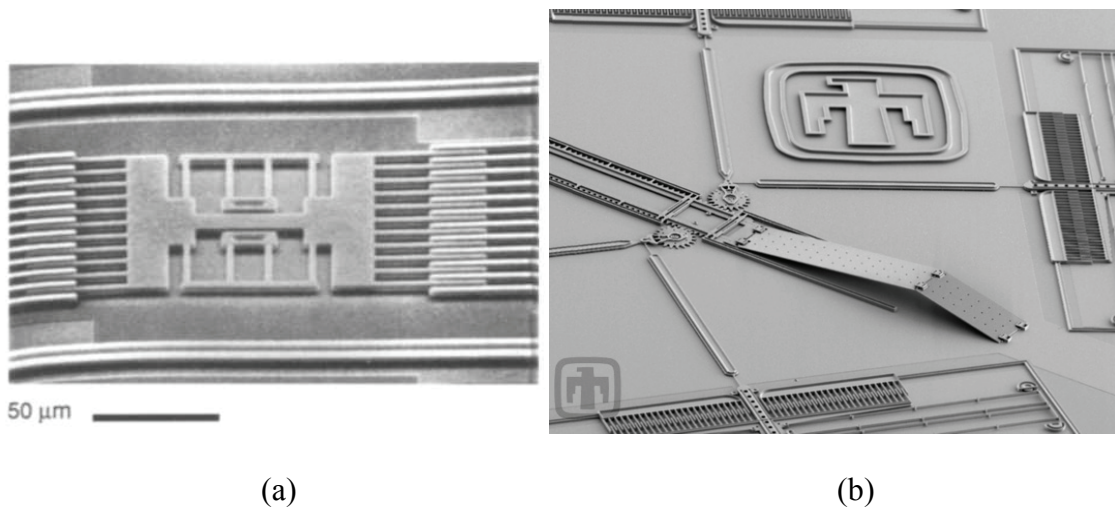
Figure 3. (a) Resonator [5], (b) actuator [6]
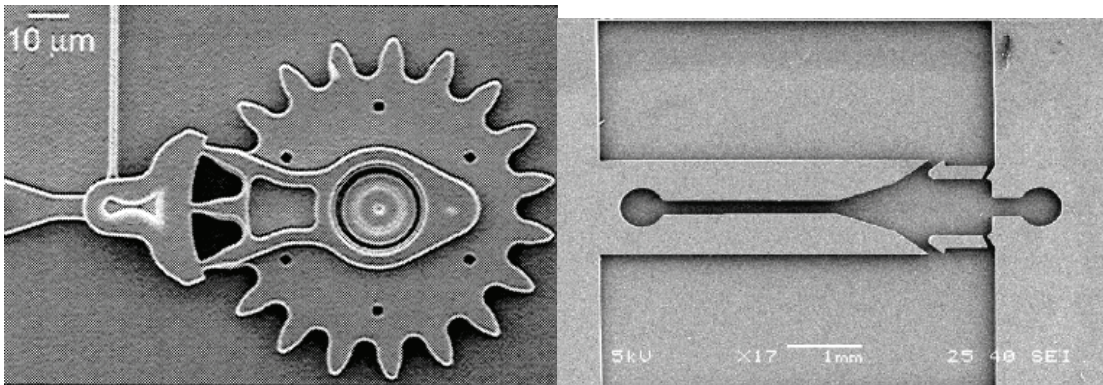
(a)   (b)

Figure 4. (a) Gear [7], (b) pump [8]
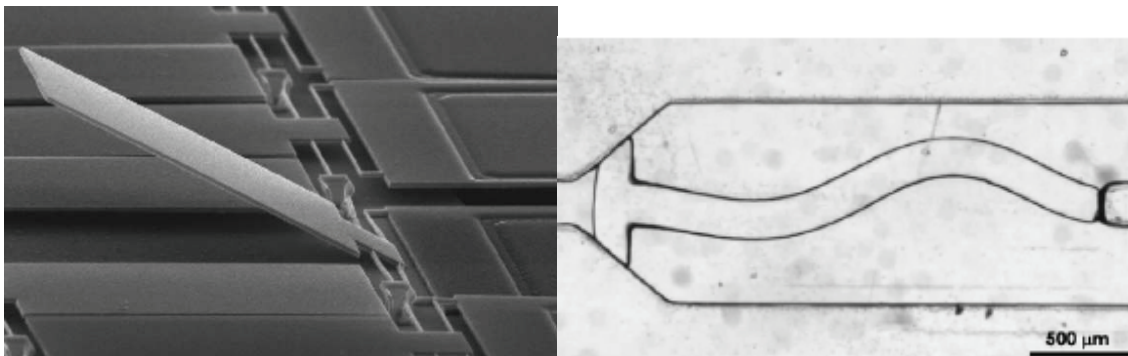
(a)   (b)

Figure 5. (a) Micro mirror [9], (b) micro valve [10]

(a)   (b)
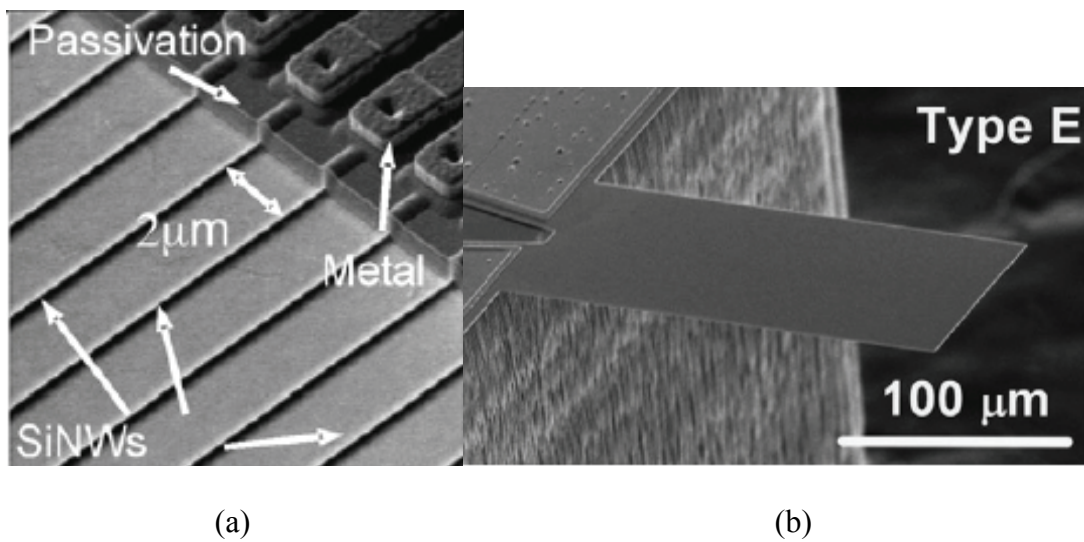
Figure 6. (a) Bio sensor [11], (b) force sensor [12]

(a)   (b)
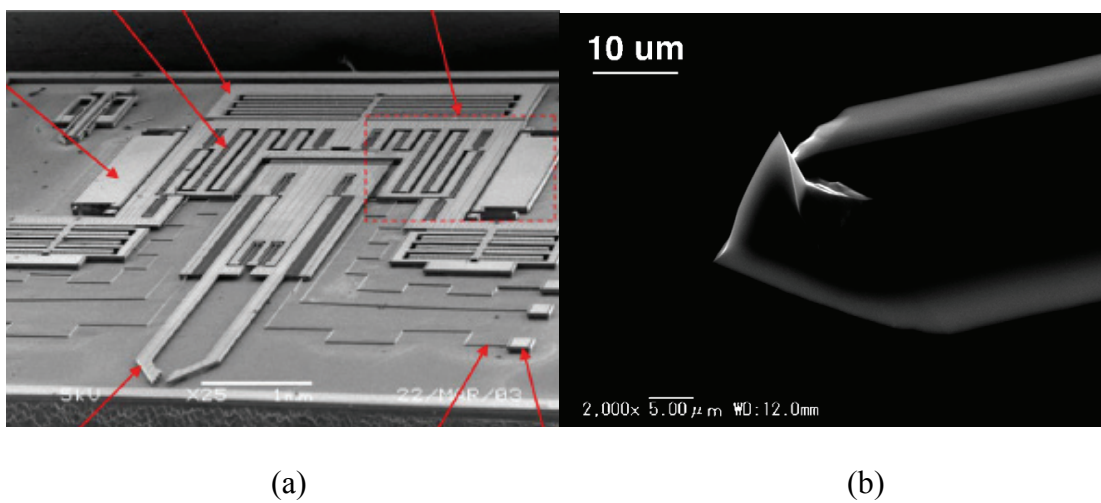
Figure 7. (a) Electrostatic gripper [13], (b) nanoknife [14]

(a)   (b)
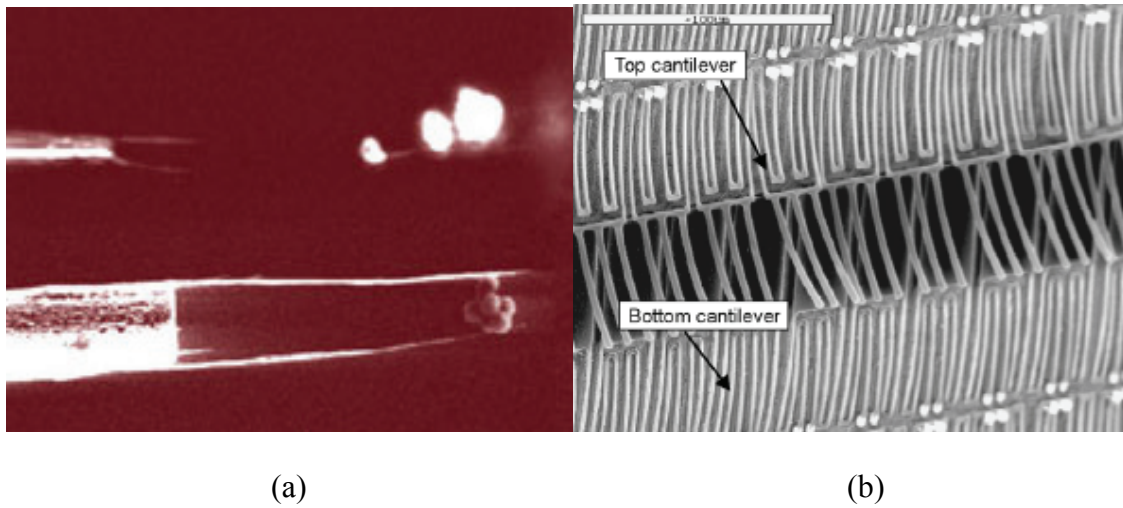
Figure 8. (a) Nanotube tweezers [15], (b) thermal actuator and sensor [16]

(a)   (b)
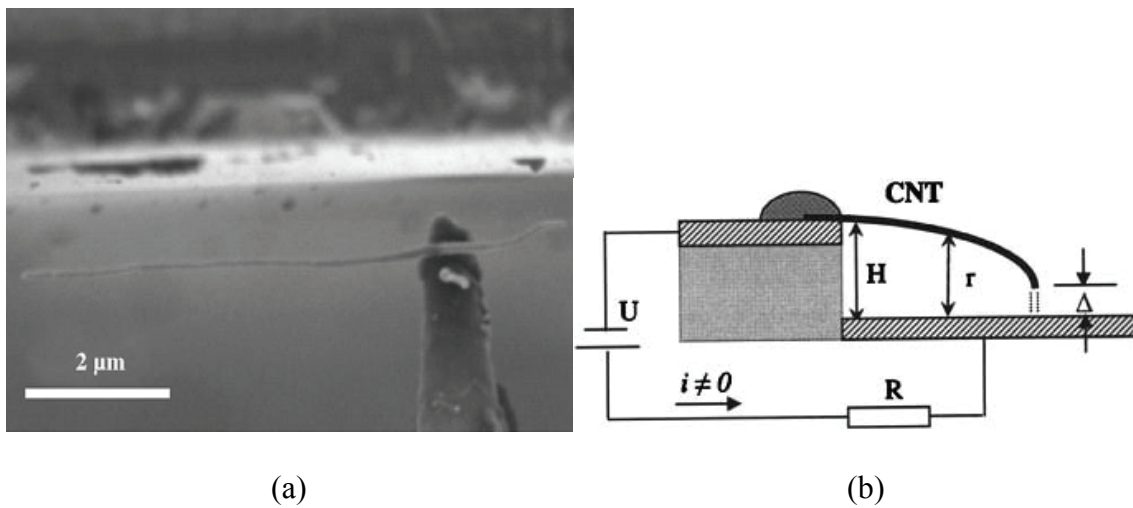
Figure 9. (a) Nanotube switch, (b) schematic of nano switch [17]

Nanomachines will probably eventually perform the functions of valves, actuators, switches, grippers, tweezers, gears, linkages, belts, punches, cutters, and manipulators for picking and placing, moving, sorting, separating, weaving, sewing, cutting, bonding, and releasing. The author believes that bottom-up fabrication methods

will probably not be able to manufacture machines in the size range of several nanometers to several hundred nanometers. Fortunately, top-down fabrication methods are rapidly being improved. It may soon be possible to affordably produce massive arrays of nanomachines. The electronics industry standard for optical lithography is now ~70nm, and companies have recently put 45nm devices into mass production. E-beam lithography has a resolution of 10nm. Nanoimprinting, nanomoulding, and nano dip-pen lithography are all being rapidly commercialized with feature sizes down to 10nm and are dramatically cheaper than e-beam lithography.

1.2. Contribution of the Dissertation

This dissertation brings together the work of the colloidal science community and the MEMS and NEMS electrostatic device community.

This research is the first study of the deflection, pull-in instability, and stiction of nanoscale beams in liquid electrolyte that includes the following features: elastic forces, electrostatic forces, osmotic forces, van der Waals forces, and adhesion (stiction) forces, in which the beam is modeled as a continuous structure, i.e. not a discrete spring.

This research is the first study of the electric and osmotic pressures between two parallel planar surfaces in a liquid electrolyte that accounts for the finite size of ions using the model of Borukhov *et* al [18]

2. ELECTROCHEMICAL FORCES, FINITE ION SIZE, AND MECHANICAL

EQUILIBRIUM

2.1. Introduction

The calculation of the pressure between two parallel planar surfaces is a classical problem of colloid science. The total pressure is the sum the electric pressure and the mechanical pressure. The classical derivation of the pressure relies on the Gouy-Chapman theory of the diffuse double layer [19], [20] , which uses the following assumptions: (1) the ions are point charges, i.e. they have infinitesimal dimensions; (2) the solution is an ideal solution; (3) the chemical potential is independent of pressure; and (4) the solution is in chemical equilibrium. These assumptions, together with the Gauss law, yield a nonlinear differential equation, known as the Poisson-Boltzmann (PB) equation, for the electric potential distribution. The derivation of the PB equation can be found in standard texts on electrochemistry [21] and colloidal science [22]. Verwey and Overbeek were the first to solve the PB equation for the potential as a function of position between two infinite parallel plates at the same electric potential [23].

The electric potential obtained from the PB equation can be used to calculate the electric pressure. The mechanical pressure difference between two points is called the osmotic pressure, which is derived by applying the principle of chemical equilibrium to the chemical potential of the solvent. The osmotic pressure is usually linearized using the assumption of a dilute solution.

This classical theory does not account for the finite size of the ions and therefore predicts unrealistically high ion concentrations and electric fields near the surface [22][24]. The standard method of accounting for finite ion size is to define a thin (approximately one ion monolayer) layer, known as the Stern layer, near the surface that acts as a standard dielectric capacitor in that it is impenetrable to ions and the electric field is uniform in this layer [25]. The regular PB equation applies outside of this layer, yielding an ionic distribution known as the diffuse layer. A more modern approach to including the effects of finite ion size rely on either Monte Carlo simulations or integral equations that must be solved numerically [26].

Borukhov *et al* modified the PB equation to account for finite ion size, resulting in much more realistic ion concentrations near the surface [18], [26]. To our knowledge, this modified theory has not been used to calculate the pressure. The objective of the research of this section is to calculate the total pressure obtained from the theory of Borukhov *et al* and compare these results to the total pressure given by the classical theory.

2.2. Governing Equations

Two parallel planar surfaces at potential ψ_1 and ψ_2 are separated by a gap of width D (figure 10). Unless otherwise stated, it is assumed that all field variables are functions of x.
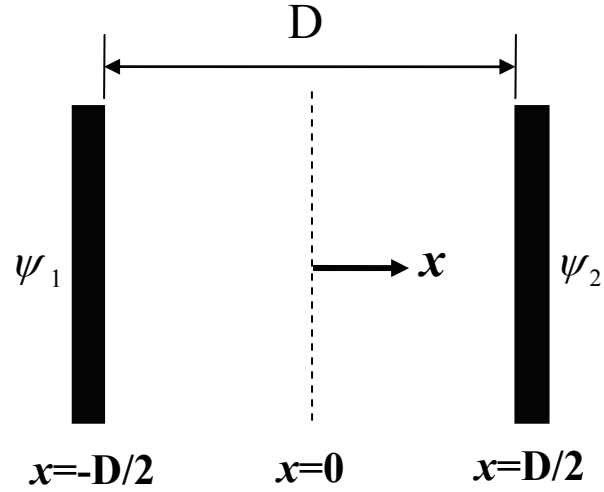
Figure 10. Diagram showing two plates and coordinate system

The total pressure, P^{total}, is the sum of the mechanical pressure, P, and the electric pressure, P^e. Mechanical equilibrium requires that the total pressure be uniform between the plates:

$$0 = -\frac{dP}{dx} + f = -\frac{d(P+P^e)}{dx} = -\frac{dP^{total}}{dx} \tag{1}$$

where f is the electric body force, and P is commonly called the osmotic pressure. Thus, mechanical equilibrium requires that the osmotic pressure between two points equal the difference in the electric pressure between the two points. The electric body force is given by the product of the free charge density, q, and the electric field:

$$0 = -\frac{dP}{dx} - q\frac{d\psi}{dx} = -\frac{dP}{dx} - \sum_{i=1}^{N} ez_i c_i \frac{d\psi}{dx} \tag{2}$$

where N is the total number of species, $e = 1.602 \times 10^{-19}$ in C is the electron charge, z_i is

the charges of species i, c_i in m^{-3} is the number density concentration of species i, and

ψ in volts is the electrical potential. Equation (1) and (2) can be combined to yield

$$dP = -dP^e = -\left(\sum_{i=1}^{N} ez_i c_i\right) d\psi \tag{3}$$

The Gauss law is given by

$$\frac{d^2\psi}{dx^2} = -\frac{q}{\varepsilon} = -\frac{1}{\varepsilon}\sum_{i=1}^{N} ez_i c_i \tag{4}$$

Electrochemical equilibrium requires that

$$0 = \frac{d\mu_s}{dx} \tag{5}$$

where μ_s in J is the electrochemical potential of species s. equations (1) – (5) are

independent of material properties. Therefore, an equation of state is needed to specify

the material:

$$\mu_s = \mu_s\{P, c_i, \psi\} \tag{6}$$

Equations (2) and (4) – (6) provide 2+2N equations to determine, the 2+2N unknowns P,

ψ, c_s, and μ_s as functions of x.

2.3. Derivation of the Total Pressure Difference

Borukhov *et al* derived the modified ion concentration by minimizing the

phenomenological total free energy of a system assuming that the size of ions and the

solvent are equal [26]. The modified ion concentrations also can be derived from the

electrochemical equilibrium. The electrochemical potential of a species s in a mixed

solution can be expressed by [18]:

$$\mu_s = \mu_s^0 + v_s P + kT \ln(a_s) + z_s e\psi \tag{7}$$

where μ_s^0 in J is the initial electrochemical potential of species s when $P = 0$, $a_s = 1$

and $\psi = 0$, P in N/m^2 is the hydrostatic pressure, $k = 1.38054 \times 10^{-23}$ in J/K is the

Boltzmann constant, T in K is the absolute temperature, a_s is the activity of species s.

The activity of species in a solution is usually related to its number fraction or its

relative concentration in the solution by means of an activity coefficient, which is [27]:

$$a_s = \frac{\Upsilon_s N_s}{N_w + \sum N_j} = \frac{\Upsilon_s c_s}{c_w + \sum c_i} \tag{8}$$

where Υ_s is the activity coefficient of species s, N_s is the number of species s in the

solution, N_w is the number of the solvent in the solution, c_w in m^{-3} is the number

concentration of the solvent. The summation is applied to all the solute species

involved in the solute on.

Since only differences in potential are physically meaningful, only relative values

of the electrochemical potential are important. It is of particular interest to inspect the

change of the electrochemical potential of a species in the unit volume solution with

respect to its concentration change. Note that for any solution the concentrations of

species and solvent satisfy [28]:

$$c_w v_w + \sum c_i v_i = 1 \tag{9}$$

where v_w in m^3 is the volume of the solvent and v_i in m^3 is the volume of species i. Hence, any change in the concentration of one particular species will result in the changes of the concentrations of other species, as well as the solvent.

Assume that the solution discussed here is an ideal solution, which means that the free energy change on mixing is only due to the change in entropy [28]. Then, $\Upsilon_s = 1$ and by Borukhov assumption, $v_s = v$ for all species s. Therefore, the equation (7-9) can be rewritten as:

$$vc_w + v\sum c_i = 1 \tag{10}$$

$$a_s = \frac{c_s}{c_w + \sum c_i} = \frac{vc_s}{vc_w + v\sum c_i} = vc_s \tag{11}$$

$$\mu_s = \mu_s^0 + vP + kT \ln(vc_s) + z_s e\psi \tag{12}$$

For z:z electrolyte,

$$\mu_+ = \mu_+^0 + vP + kT \ln(vc^+) + ze\psi \tag{13}$$

$$\mu_- = \mu_-^0 + vP + kT \ln(vc^-) - ze\psi \tag{14}$$

$$\mu_w = \mu_w^0 + vP + kT \ln(vc_w) \tag{15}$$

where μ_+, μ_- and μ_w in J are the total electrochemical potential of the positive ion, the negative ion and the solvent respectively , μ_+^0, μ_-^0 and μ_w^0 in J are the initial electrochemical potential of the positive ion, the negative ion and the solvent respectively when $P = 0$ and c^+ is the concentration of positive ion, c^- is the concentration of negative ion and z is the valence of ions. The electrical term is not included for the solvent because the solvent (water) carries no net charge $z_w = 0$.

Equation (15) can be rewritten with regarding to the ion concentrations by equation (10):

$$\mu_w = \mu_w^0 + vP + kT \ln(1 - v(c^+ + c^-)) \tag{16}$$

The differentiation of equation (13), (14) and (16) leads to the electrochemical equilibrium for each species:

$$d\mu_+ = vdP + kT\frac{dc^+}{c^+} + zed\psi = 0 \tag{17}$$

$$d\mu_- = vdP + kT\frac{dc^-}{c^-} - zed\psi = 0 \tag{18}$$

$$d\mu_w = vdP - kT\frac{v(dc^+ + dc^-)}{1 - v(c^+ + c^-)} = 0 \tag{19}$$

Solving the simultaneous equations (17-19) leads to the ion concentrations in equation (20) which are identical with the ion concentrations derived by Borukhov *et al.*

$$c^\pm = \frac{c_b \exp\left(\mp \frac{ze\psi}{kT}\right)}{1 - 2c_b v + 2c_b v \cosh\left(\frac{ze\psi}{kT}\right)} \tag{20}$$

where c_b is the concentration of ion in bulk. When substituted into the Gauss law, the ion concentrations, equation (20), give the modified PB (MPB) equation

$$\frac{d^2\psi}{dx^2} = \frac{2ze}{\varepsilon}\frac{c_b \sinh\left(\frac{ze\psi}{kT}\right)}{1 - 2c_b v + 2c_b v \cosh\left(\frac{ze\psi}{kT}\right)} \tag{21}$$

The MPB equation can be solved for $\psi\{x\}$, which can then be substituted into equation (3) to obtain the electric pressure difference between two points.

Electrochemical equilibrium, equation (19) yield the osmotic pressure difference,

$$dP = kT \frac{dc^+ + dc^-}{1 - v(c^+ + c^-)} \tag{22}$$

The ion concentrations, equation (20), can be used in equation (22) and (3) to obtain the osmotic pressure difference and the electric pressure difference resulting in equation (23) and (24)

$$dP = \left(\frac{2zec_b \sinh\left(\frac{ze\psi}{kT}\right)}{1 - 2c_b v + 2c_b v \cosh\left(\frac{ze\psi}{kT}\right)} \right) d\psi \tag{23}$$

$$dP^e = -\left(\frac{2zec_b \sinh\left(\frac{ze\psi}{kT}\right)}{1 - 2c_b v + 2c_b v \cosh\left(\frac{ze\psi}{kT}\right)} \right) d\psi \tag{24}$$

Therefore, from inspection of equations (23) and (24), it is apparent that the model of Borukhov *et al* satisfies mechanical equilibrium at every point.

If the solution is dilute, that is $\sum vc_i \ll 1$, $vc_w \approx 1$, equation (22) can be further simplified into equation (25) which is identical to the classical osmotic pressure difference in dilute solution.

$$dP = kT(dc^+ + dc^-) \tag{25}$$

The ion concentration equation (20) is also simplified into equation (26) which leads the MPB equation into the classical PB equation in equation (27).

$$c^\pm = c_b \exp\left(\mp \frac{ze\psi}{kT} \right) \tag{26}$$

$$\frac{d^2\psi}{dx^2} = \frac{2zec_b}{\varepsilon}\sinh\left(\frac{ze\psi}{kT}\right) \qquad (27)$$

2.4. Total Pressure between Two Identically Charged Parallel Surfaces in Liquid Electrolyte

The total pressure difference at any position x between two identically charged plates in an electrolyte solution is rewritten as follow by combining equation (1)-(3) and (22)

$$\frac{dP_x^{total}}{dx} = kT\frac{dc^+/dx + dc^-/dx}{1-v(c^+ + c^-)} - \varepsilon\frac{d\psi}{dx}\frac{d}{dx}\left(\frac{d\psi}{dx}\right) \qquad (28)$$

$$x=-\infty \qquad\qquad x=0 \quad x=D/2 \qquad\qquad x=\infty$$
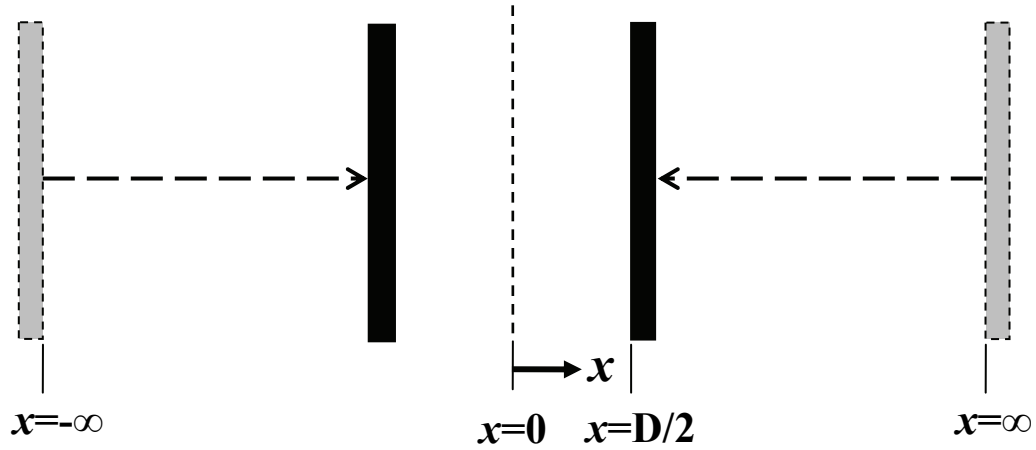
Figure 11. Schematic of parallel plates

The change in pressure at x on bringing two plates together from infinity ($x' = \infty$) to $x' = D/2$, as shown in figure 11, at constant temperature is therefore

$$\int_{x'=\infty}^{x'=D/2} dP_x^{total} = \int_{x'=\infty}^{x'=D/2}\left[kT\frac{dc^+ + dc^-}{1-v(c^+ + c^-)} - \varepsilon\frac{d\psi}{dx}d\left(\frac{d\psi}{dx}\right)\right] \qquad (29)$$

This becomes

$$P_x^{total}(D) - P_x^{total}(\infty) = -\left[\frac{\varepsilon}{2}\left(\frac{d\psi}{dx}\right)^2_{x(D)} - \frac{\varepsilon}{2}\left(\frac{d\psi}{dx}\right)^2_{x(\infty)} \right]$$
$$- \frac{kT}{v}\left[\ln(1 - vc_x^+(D) - vc_x^-(D)) - \ln(1 - vc_x^+(\infty) - vc_x^-(\infty)) \right] \tag{30}$$

Turning to the ionic distribution, differentiating equation (20) and using equation (21) we can obtain:

$$\frac{d}{dx}\left(\frac{kT}{v}\ln(1 - vc^+ - vc^-) \right) = \frac{d}{dx}\left(\frac{kT}{v}\ln \frac{1 - 2c_b v}{1 - 2c_b v + 2c_b v\cosh\left(\frac{ze\psi}{kT}\right)} \right)$$

$$= -ze\frac{d\psi}{dx} \frac{2c_b \sinh\left(\frac{ze\psi}{kT}\right)}{1 - 2c_b v + 2c_b v\cosh\left(\frac{ze\psi}{kT}\right)} \tag{31}$$

$$= -\frac{d\psi}{dx}\left(\varepsilon\frac{d^2\psi}{dx^2} \right)$$

Therefore

$$\frac{kT}{v}\left[\ln(1 - vc_x^+ - vc_x^-) - \ln(1 - vc_0^+ - vc_0^-) \right] = \int_0^x -\frac{\varepsilon}{kT}\frac{d\psi}{dx}d\left(\frac{d\psi}{dx}\right)$$
$$= -\frac{\varepsilon}{2}\left(\frac{d\psi}{dx}\right)^2_x + \frac{\varepsilon}{2}\left(\frac{d\psi}{dx}\right)^2_0 \tag{32}$$

Because the electric field in the mid plane ($x = 0$) is zero due to the symmetry, equation (32) leads to

$$\frac{kT}{v}\ln(1 - vc_x^+ - vc_x^-) = \frac{kT}{v}\ln(1 - vc_0^+ - vc_0^-) - \frac{\varepsilon}{2}\left(\frac{d\psi}{dx}\right)^2_x \tag{33}$$

Substituting equation (33) into equation (30) and putting $P_x(\infty) = 0$, yields

$$P_x(D) = \frac{kT}{v}\left[\ln(1-2c_bv) - \ln(1-vc_0^+ - vc_0^-)\right] \tag{34}$$

Equation (34) shows that the total pressure is uniform across the gap and independent of position x as expected by the mechanical equilibrium.

From the natural log series expansion (35), the equation (34) can be written as equation (36)

$$\ln(1+\chi) = \chi - \frac{1}{2}\chi^2 + \frac{1}{3}\chi^3 - \frac{1}{4}\chi^4 + \cdots \tag{35}$$

$$P_x(D) = \frac{kT}{v}\left[\left(-2c_bv - \frac{(2c_bv)^2}{2} - \cdots\right) - \left(-(vc_0^+ + vc_0^-) - \frac{(vc_0^+ + vc_0^-)^2}{2} - \cdots\right)\right] \tag{36}$$

If the solution is in dilute, the higher order terms in equation (36) vanish and yield to equation (37) which is identical to the classical total pressure in dilute solution.

$$P_x(D) = kT\left[(c_0^+ + c_0^-) - 2c_b\right] \tag{37}$$

2.5. Results and Discussion

The ions and solvent are modeled as cubes of dimension a, such that $v = a^3$. It is assumed that the two surfaces are at equal potentials, i.e. $\psi_1 = \psi_2$. The COMSOL, the commercially available software, is used to solve the nonlinear PB and MPB equations.

The method of Borukhov et al place limits on the ion size by equation (10). Because the concentrations and volume of species in equation (10) are always positive, the following condition must be satisfied:

$$0 \le v(c^+ + c^-) \le v(c_w + c^+ + c^-) = 1 \text{ and } 0 \le v = a^3 \le \frac{1}{c^+ + c^-} \tag{38}$$

The ion concentrations given by equation (20) can be used in equation (38) to obtain

$$0 \le a \le \sqrt[3]{\frac{1}{2c_b}} \tag{39}$$

in which the maximum ion size depends on the bulk ion concentration, as shown in figure 12.
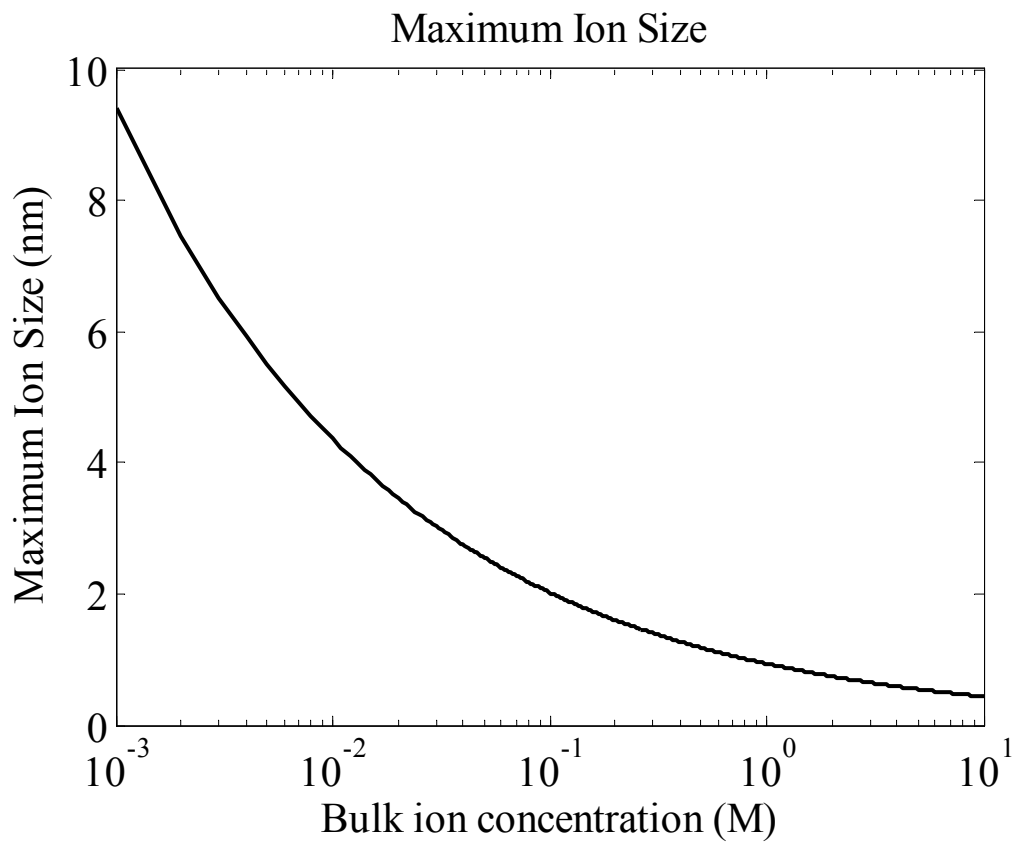
Figure 12. Maximum ion size for the MPB method of Borukhov *et al*

The maximum ion size is the largest ion size possible when the unit volume is full with only ions.

Figures 13-15 show the total pressure calculated by the classical model and Borukhov model as a function of surface separation. For a bulk concentration of 0.001M and a surface potential of 25mV, the two models predict almost identical pressures. It means that the Borukhov method and the classical method are almost identical in dilute ion concentration and low electric potential. The two models differ more as the bulk ion concentration, surface potentials, and ion size increase.
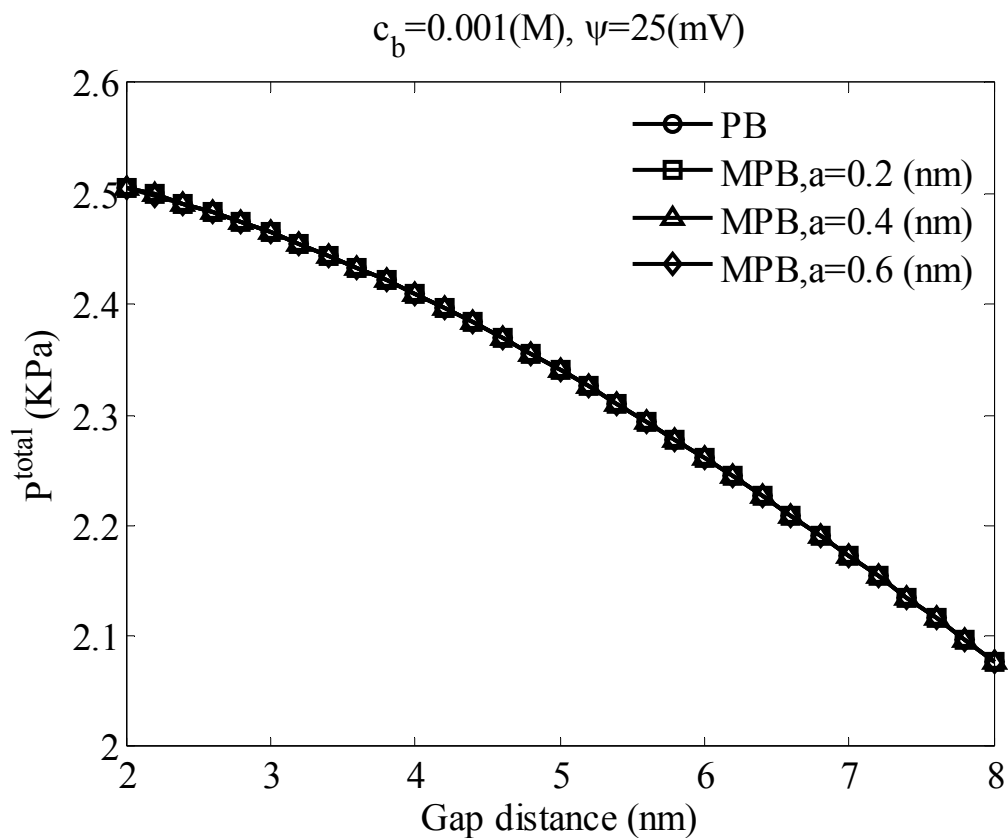
Figure 13. Total pressure between two parallel plates versus gap distance when $c_b = 0.001\text{M}$ and $\psi_1 = \psi_2 = 25\,\text{mV}$
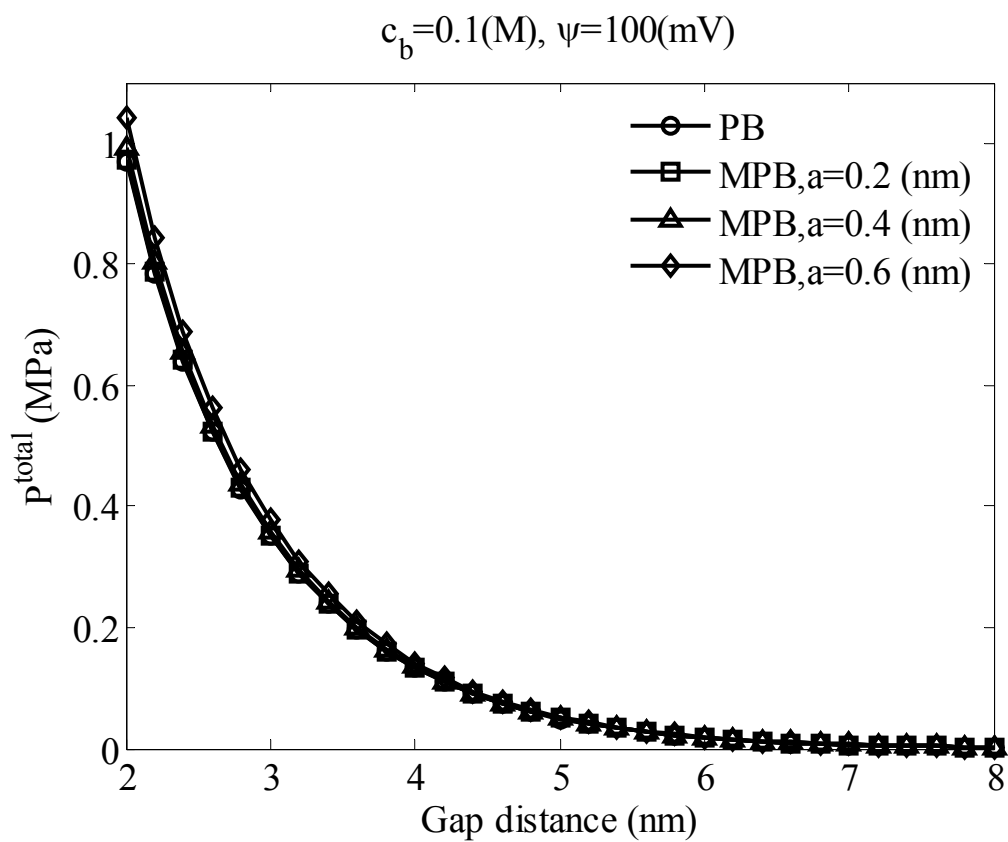
Figure 14. Total pressure between two parallel plates versus gap distance when $c_b = 0.1\,\mathrm{M}$ and $\psi_1 = \psi_2 = 100\,\mathrm{mV}$
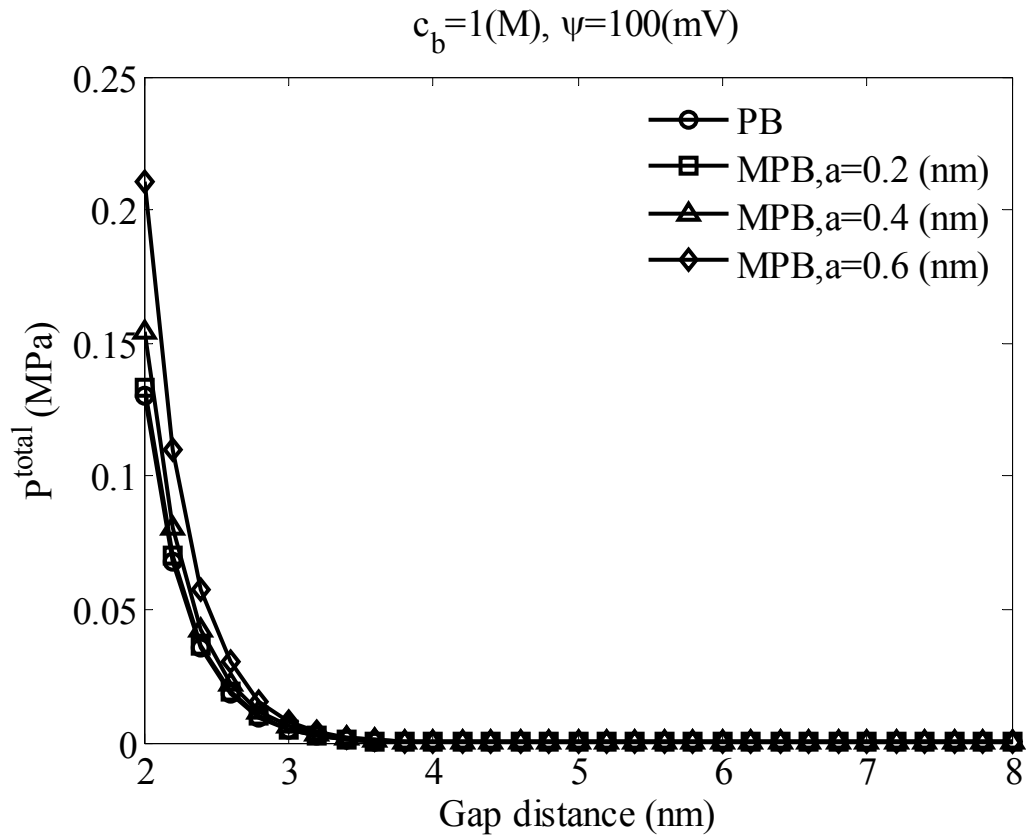
Figure 15. Total pressure between two parallel plates versus gap distance when $c_b = 1\,\text{M}$ and $\psi_1 = \psi_2 = 100\,\text{mV}$

In relatively high ion concentrations and high electric potential, the total pressure calculated by the Borukhov method was larger than that calculated by the classical method and increased as the ion size increased as shown in Figures 14-15. The ion size effect to the total pressure looks prominent in small gap distance region. Because of the scale difference, it is difficult to see the effect of the ion size to the total pressure when the gap distance is larger than 4nm in Figures 14-15. So the ratio between the total pressure calculated by the MPB method and the total pressure calculated by the PB method is given in Figures 16-18 as a function of gap distance.
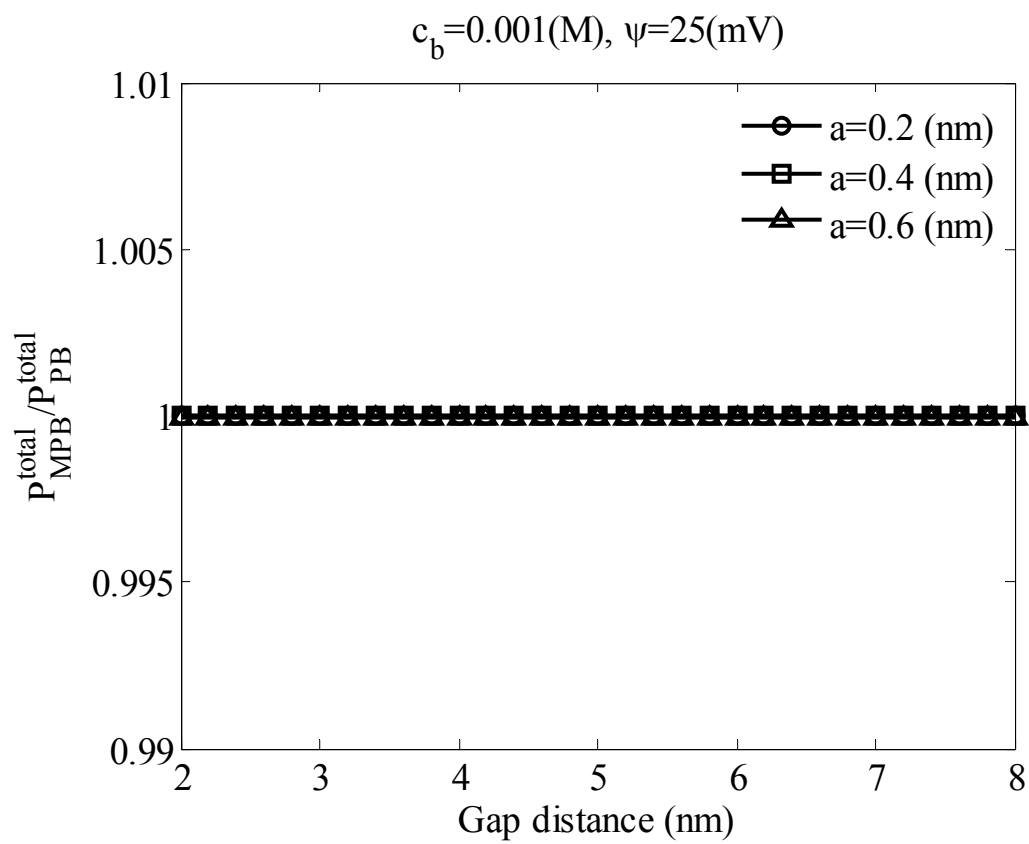
Figure 16. Total pressure ratio versus gap distance when $c_b = 0.001\mathrm{M}$ and $\psi_1 = \psi_2 = 25\,\mathrm{mV}$
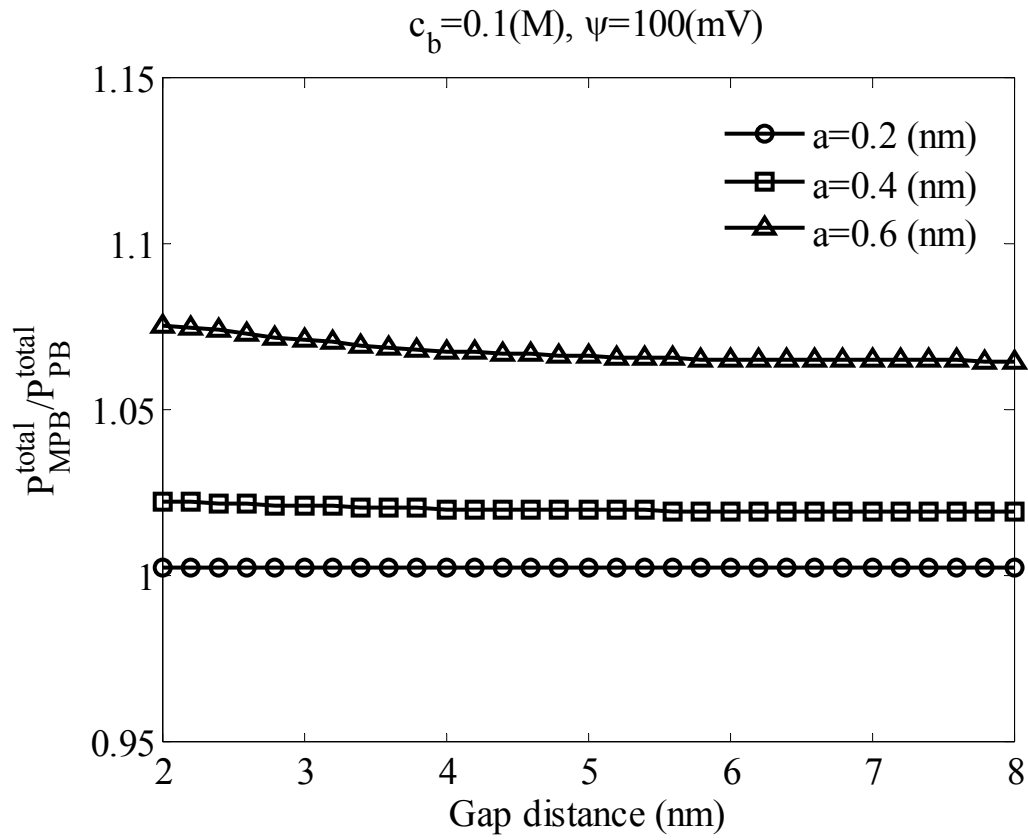
Figure 17. Total pressure ratio versus gap distance when $c_b = 0.1\,\mathrm{M}$ and $\psi_1 = \psi_2 = 100\,\mathrm{mV}$
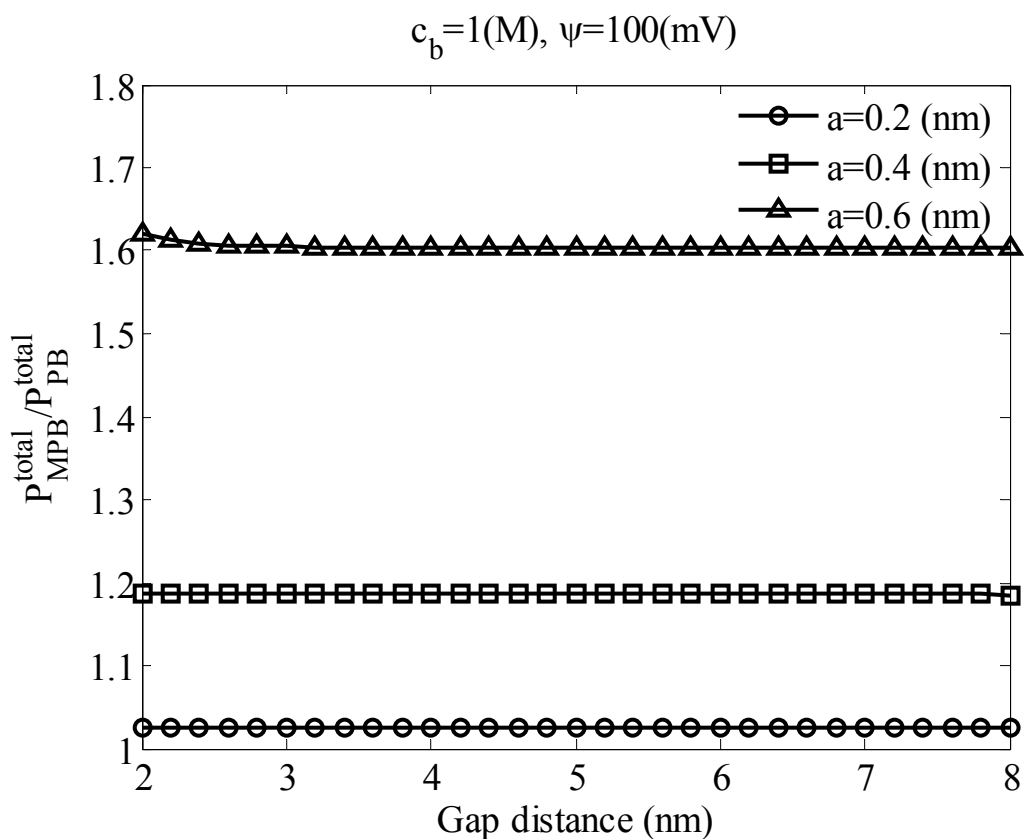
Figure 18. Total pressure ratio versus gap distance when $c_b = 1\,\mathrm{M}$ and $\psi_1 = \psi_2 = 100\,\mathrm{mV}$

The ratio of the total pressure calculated by the MPB method and the total pressure calculated by the PB method is given in Figures 16-18 as a function of gap distance. The pressure ratio was independent of gap distance except for the small gap distance region with large ion size as shown in Figures 16-18.
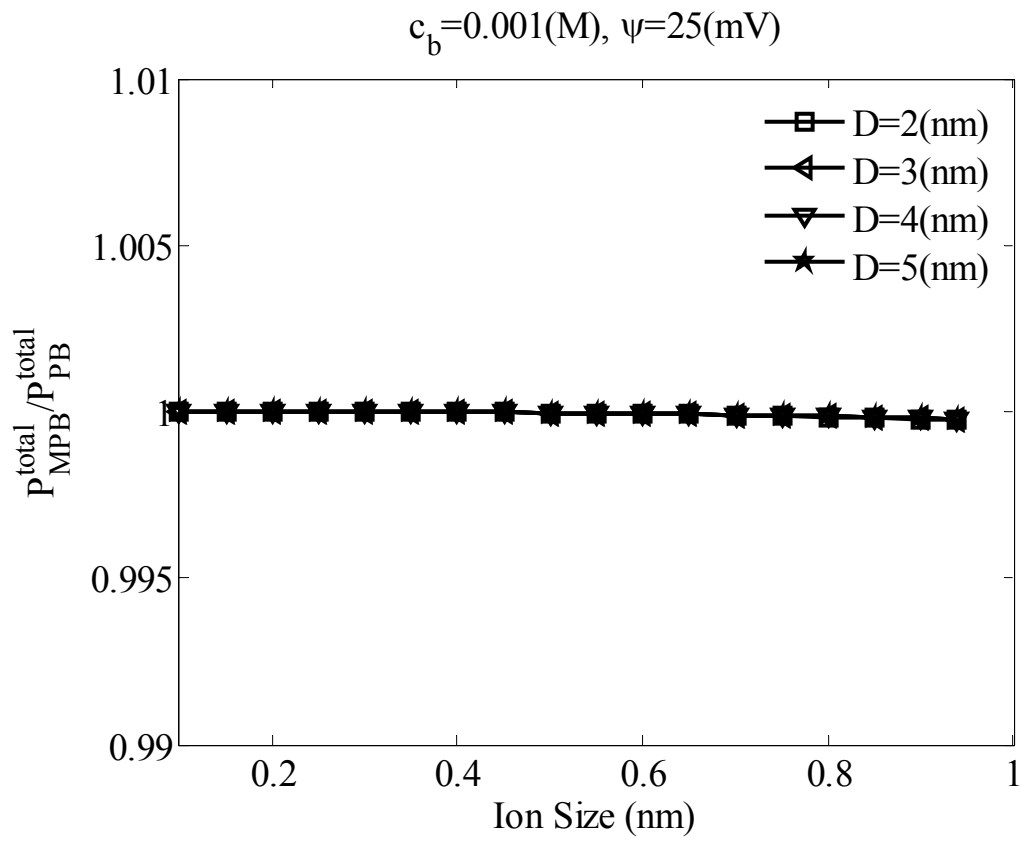
Figure 19. Total pressure ratio versus ion size when $c_b = 0.001\text{M}$ and $\psi_1 = \psi_2 = 25\,\text{mV}$
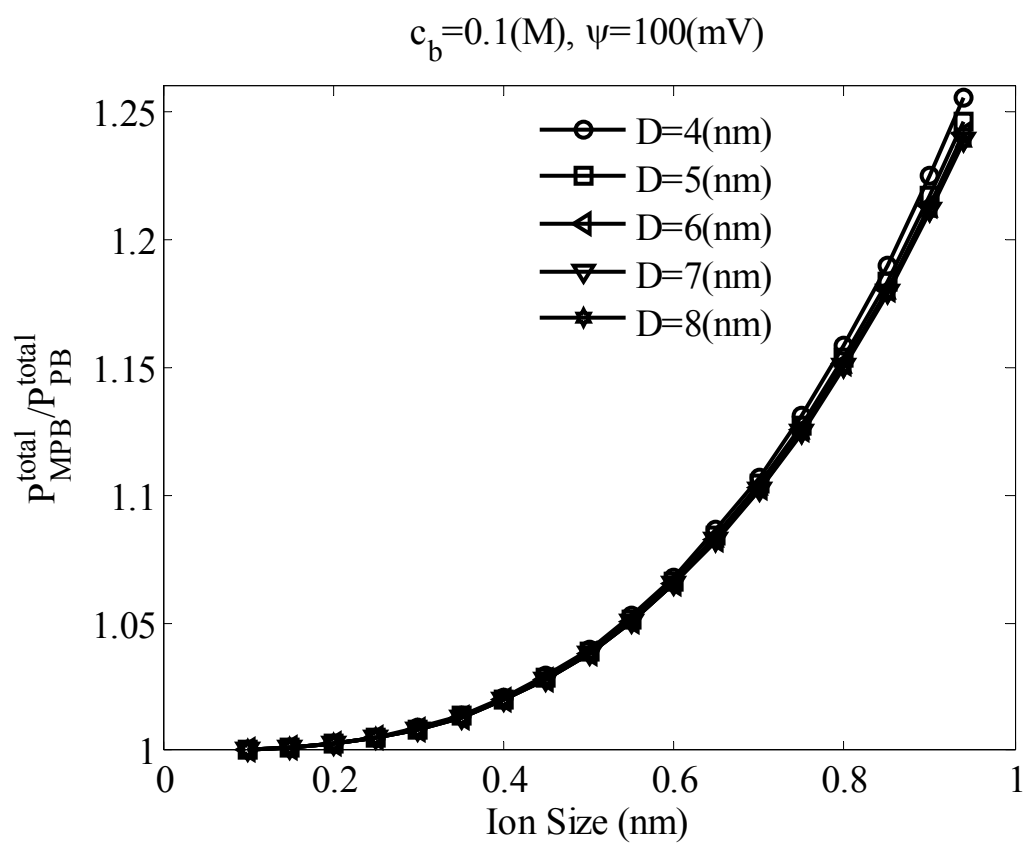
Figure 20. Total pressure ratio versus ion size when $c_b = 0.1\text{M}$ and $\psi_1 = \psi_2 = 100\text{mV}$
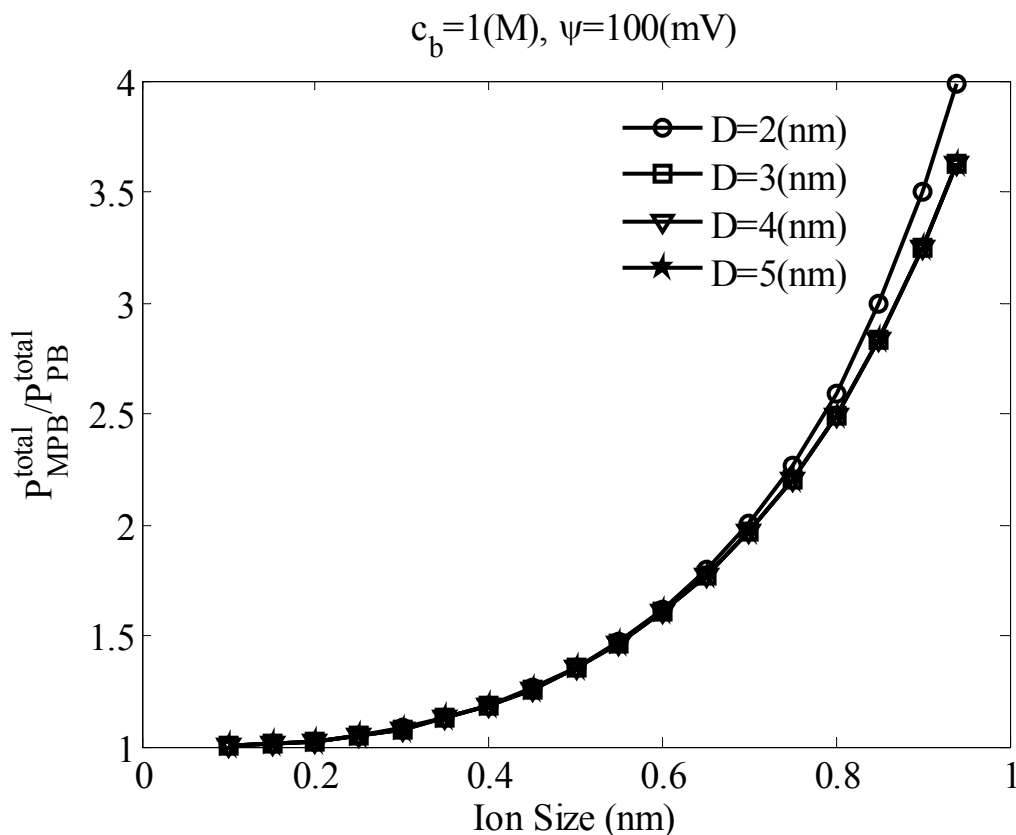
Figure 21. Total pressure ratio versus ion size when $c_b = 1\text{M}$ and $\psi_1 = \psi_2 = 100\text{mV}$

Figures 19-21 show the total pressure ratio as a function of ion size. As shown in figure 19, the total pressure ratio is not significantly affected much by the ion size when the bulk ion concentration is only 0.001M and the surface potential is only 25mV. However, as seen in Figures 20-21, for relatively high ion concentrations and high surface potentials, the total pressure ratio increases significantly as the ion size increases. The total pressure ratio was independent of the surface separation distance except for very small separations.

The pressure between two parallel planar surfaces at equal electric potentials is derived using the MPB equation. This model is also valid for arrays of parallel plates and two large spheres of radii R_1 and R_2 with a small distance D apart (figure 22) by Derjaguin approximation given by equation (40) [24].
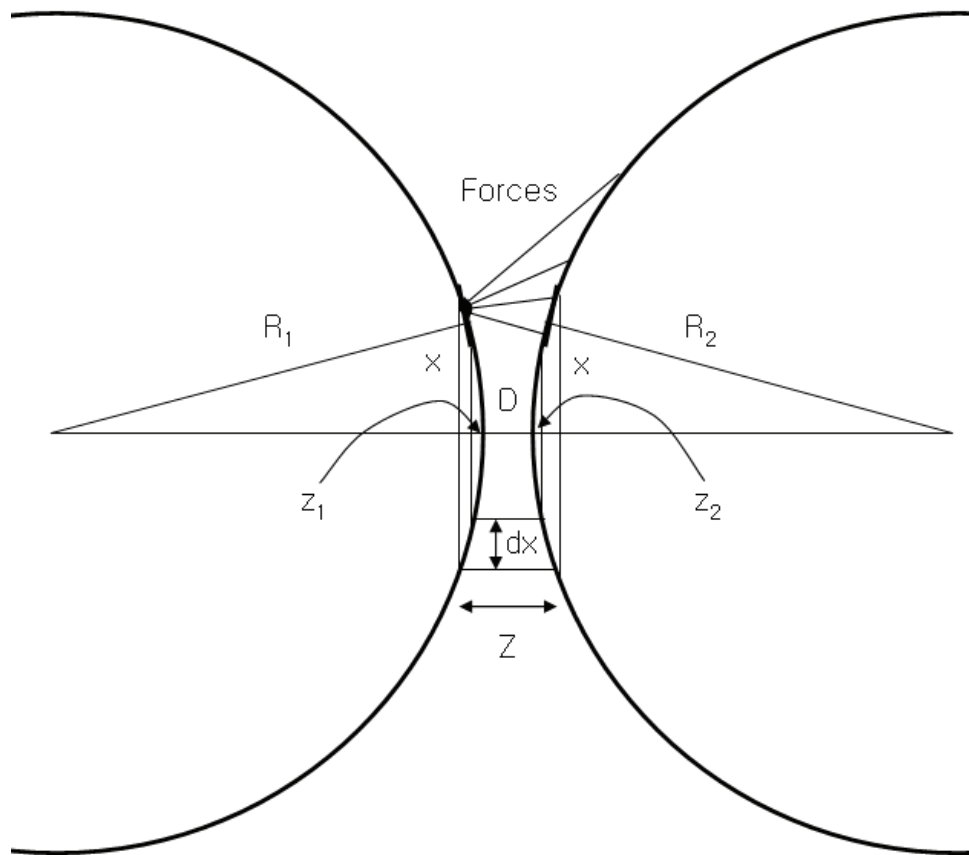
Figure 22. Derjaguin approximation [24]

$$F(D)_{\text{sphere}} \approx 2\pi \left(\frac{R_1 R_2}{R_1 + R_2} \right) W(D)_{\text{planes}} \qquad (40)$$

This equation, known as the Derjaquin approximation, gives for the force between two spheres in terms of the energy per unit area of two flat surfaces at the same

separation D. It is applicable to any type of force law, whether attractive, repulsive or oscillatory, so long as the range of the interaction and the separation D is much less than the radii of the spheres [24]. The Derjaguin approximation also can be applied to the two orthogonal cylinders.

2.6. Summary

The pressure between two parallel planar surfaces at identical electric potentials is calculated using both the classical PB equation and the modified PB equation of Borukhov *et al* to account for finite ion size. Results are presented for a z:z symmetric electrolyte. The pressure predicted by the two models differ more as the bulk ion concentration, surface potential, and ion size increase. For a bulk ion concentration of 0.001M and a surface potential of 25mV, the two models predict almost identical pressure. However, for a bulk ion concentration of 1M and a surface potential of 100mV, the MPB predicted a pressure that is 60 percent higher than the PB for an ion size of 0.6nm. For a bulk ion concentration of 1M and a surface potential of 100mV and an ion size of 0.9nm, the MPB predicted a pressure that is four times higher than the PB. The ratio of the pressures predicted by the two models is relatively independent of the separation of the two plates.

3. BEAM DEFLECTIONS AND PULL-IN INSTABILITY

3.1. Introduction

Nanobeams that change their configuration in response to changes in ion concentrations can serve as both sensors and actuators.

It has long been demonstrated that long (micron length), thin (one micron or less), cantilevered beams will bend if the surface stress on one side of the beam changes. The beam surface is functionalized with the proper chemical coating, and this coating will expand or contract in response to a change in the ion concentration of the liquid. The expansion or contraction alters the surface stress, thereby bending the beam. Many applications have been proposed for these beams, including actuators [29]. More recently, Pinnaduwage and coworkers demonstrated that the surface stress-induced bending of a cantilever beam can be used to measure binding energy [30].

In addition to surface stresses, van der Waals forces and electrostatic forces also play an important role in the mechanics of nanoscale objects. In gas or vacuum, parallel plate electrostatic actuators undergo a "snap-down" or "pull-in" instability in which the two electrodes spontaneously come into contact when the distance between the two actuators is less than 2/3 of the initial distance. The most recent and rigorous study of these "pull-in" instabilities is provided in the sequence of papers by Degani and Nemirovsky [31].

Actuators similar to parallel plate actuators have been extended to the nanoscale. Kim and Lieber [15] developed "nanotweezer" NEMS based on carbon nanotubes for

manipulation and interrogation of nano-structures. The tweezers have two carbon nanotubes attached to a glass rod. The potential difference between the two carbon nanotubes produces an attractive electrostatic force that can overcome the elastic restoring force of the carbon nanotubes in closing the tweezers. The nanotweezers were used to manipulate polystyrene nanoclusters containing fluorescent dye molecules. Akita and Nakayama [32] performed similar experiments and analysis for nanotweezers consisting of carbon nanotubes in an AFM. Two nanotube arms were fixed at the most appropriate position on the silicon cantilever tips used as the substrate of the nanotweezers for the AFM.

Van de Waals forces do not significantly affect MEMS devices. However, van der Waals forces are important on the nanoscale. Dequesnes *et al* [33] analytically studied the pull-in instability of carbon nanotube switches, which are essentially tweezers, using a continuum model for three coupled energies: the elastic energy, the van der Waals energy, and the electrostatic energy.

Rotkin [34] considered the effect of the van der Waals force on the pull-in instability and obtained analytical expressions for the pull-in gap and voltage of a general model. Lin and Zhao [35] studied the dynamic behavior of nanoscale electrostatic actuators by considering the effect of the van der Waals force. In these investigations, a one degree of freedom lumped parameter model has been used. Asghar Ramezani *et al* [36] investigated the pull-in parameters of the cantilever type nanoscale electrostatic switches considering van der Waals force using a distributed parameter model.

Electrostatic MEMS actuators and other microstructures are typically used in gas or vacuum. There has been less work devoted to developing MEMS to operate in liquids. Electrostatic actuators do not work in liquids if the electrode separation is as great as one micron. This is because the electric double layers disable the electrostatic force between the two electrodes. Sounart and Michalske [37] tested a MEMS comb drive electrostatic actuator in various liquids, including ethylene glycol, HeOH, isopropyl alcohol, EtOH, EG, H_2O, and MeNO. Applied DC voltages were below the threshold that initiates electrolysis and electrochemical reactions. It was demonstrated that minute concentrations of ionic impurities were sufficient to disable the actuators. However, when an AC voltage was applied, actuation was achieved above a critical frequency that varied by four orders of magnitude among the liquids tested. Rollier *et al* [38], [39] performed an analytical and experimental study of MEMS parallel-plate electrostatic actuators with AC drive signals in liquids. They demonstrated that the stable range of motion can be extended to beyond two-thirds of the initial separation, and even suppressed entirely.

The double layer does not disable electrostatic actuators when the two electrodes are separated by distances that are small enough to allow the two double layers to interact. In liquid electrolytes, the interaction of electric double layers alters the electrostatic force and also introduces an osmotic force. The mechanics of two electrodes separated by nanometers has been modeled using discrete springs, including the following forces: elastic, osmotic, electric, and van der Waals. The primary motivation for this work is the use of atomic force microscopy to measure the forces between solid

surfaces in liquid electrolytes, in which the AFM cantilever beam is modeled as a discrete spring. These experiments are usually performed to measure the zeta potential and/or determine force-distance or force-voltage relations [40]-[46]. However, voltage-distance relations are necessary to design electrostatic actuators that operate in liquid electrolytes. Boyd and Kim [47] recently provided voltage-distance relations for nanoscale electrostatic actuators in liquid electrolytes. However, the spring was modeled as a discrete point, not a continuous elastic structure.

It is believed that the research presented herein is the first study of nanoscale beams in liquid electrolytes in which the beam is modeled as a continuous elastic structure acted upon by electric, osmotic forces, and van der Waals forces. The objectives of this research are to identify the non-dimensional parameters that affect the beam deflection and pull-in instability, and then determine the critical values of ion concentration and surface potential that will cause the pull-in instability.

The governing equations are presented in section 3.2. Results for a gas (or vacuum) and a liquid electrolyte are presented in sections 3.4 and 3.5, respectively. Results for a liquid electrolyte include case studies of a silicon nanoswitch and a double wall carbon nanotube switch.

3.2. Governing Equations

A cantilever beam separated from a fixed substrate by a liquid electrolyte is shown in figure 23. The beam is assumed to be prismatic, homogeneous, and comprised of an isotropic linear elastic material. The cantilever beam bends due to the attractive van der

Waals force and the electrochemical force, which can be either attractive or repulsive depending on the surface electric potentials. At a critical "pull-in" voltage, the cantilever beam becomes unstable and spontaneously contacts the substrate.
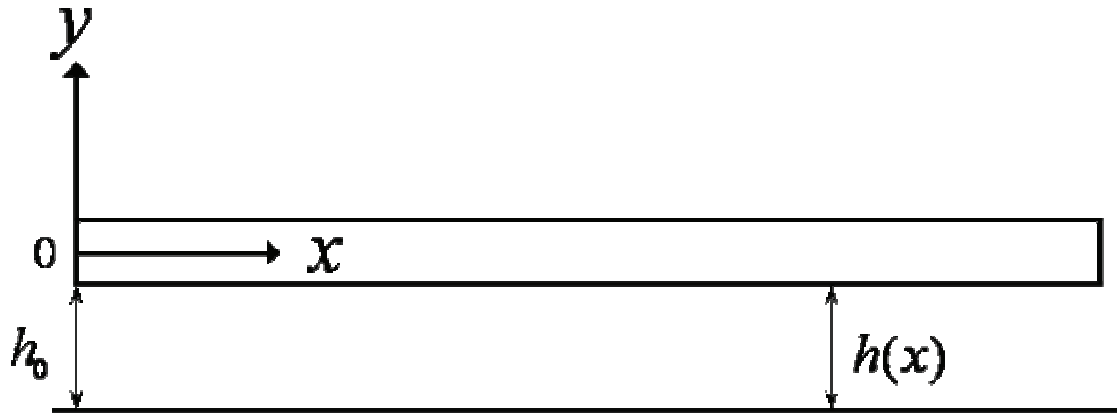
Figure 23. Nano cantilever beam

The beam is modeled using simple beam theory, also known as Euler-Bernoulli beam theory,

$$\tilde{E}I\frac{d^4u}{dx^4} = f_{vdW} + f_{EC} \tag{41}$$

where u is the deflection of the beam, x is the position along the beam measured from the clamped end, w is the width of the beam, t is the thickness of the beam, I is the moment of inertia of the beam cross section, and $\tilde{E}$ is the effective modulus. The effective modulus $\tilde{E}$ becomes the Young's modulus E for narrow beams ($w < 5t$) and becomes the plate modulus $E/(1-v^2)$, where v is the Poisson ratio, for wide beam

($w \geq 5t$) [48]. f_{vdW} and f_{EC} are the van der Waals and electrochemical force per unit length of the beam, respectively. The boundary conditions are

$$u(0) = \frac{du(0)}{dx} = 0 \tag{42}$$

$$\frac{d^2u(L)}{dx^2} = \frac{d^3u(L)}{dx^3} = 0 \tag{43}$$

3.2.1. van der Waals force

The van der Waals force results from the interaction between instantaneous dipole moments of atoms. The van der Waals force is significant when separation is less than the retardation length which corresponds to the transition between the ground and the excited states of the atom. The attraction is proportional to the inverse cube of the separation and is affected by material properties. The van der Waals force per unit length between two parallel plates is given by [24]

$$f_{vdW} = -\frac{A_h w}{6\pi(h_0 + u)^3} \tag{44}$$

where h_0 is the initial gap between the beam and the ground plane, and A_h is the Hamaker constant.

3.2.2. Electrochemical force

The electrochemical force per unit beam length f_{EC} is the sum of the electrical force per unit beam length f_E and chemical (or osmotic) force per unit beam length f_C:

$$f_{EC} = f_E + f_C \tag{45}$$

The chemical force is due to the difference in the osmotic pressure of the interstitial solution (P_i) and the bulk solution (P_0) with which it is in contact. For a dilute solution,

$$f_C = (P_i - P_0)w \tag{46}$$

By combining the general expression for the osmotic pressure of an electrolyte solution and the ionic concentrations c^+ and c^- at equilibrium

$$P = kT\sum c_k, \qquad c^+ = c_b \exp(-\frac{ez\psi}{kT}), \qquad c^- = c_b \exp(\frac{ez\psi}{kT}) \tag{47a-c}$$

where c_b is the bulk ion concentration, e is the electronic charge, z is the absolute value of the valence, ψ is the electric potential, k is the Boltzmann constant, T is the absolute temperature, and we have assumed that the bulk potential is zero. Then, the chemical force can be written as

$$f_C = 2c_b kTw(\cosh\left(\frac{ze\psi}{kT}\right) - 1) \tag{48}$$

The electric force is

$$f_E = -\frac{1}{2}\varepsilon\varepsilon_0 |\nabla\psi|^2 \tag{49}$$

where ε is the relative permittivity of the dielectric medium and ε_0 is the permittivity of free space. The electric field can be obtained from the Gauss law written in the form of the Poisson-Boltzmann equation given by

$$\nabla^2\psi = -\frac{1}{\varepsilon\varepsilon_0}(zec^+ - zec^-) = \frac{2zec_b}{\varepsilon\varepsilon_0}\sinh(\frac{ze\psi}{kT}) \tag{50}$$

The Poisson-Boltzmann equation provides accurate results when concentrations do not exceed 1M and surface potentials are less than 200mV.

Figure 24 shows the two electrode plates and coordinate system separated with distance h. One of the electrode plates is segment of the cantilever beam and the other is segment of the substrate.
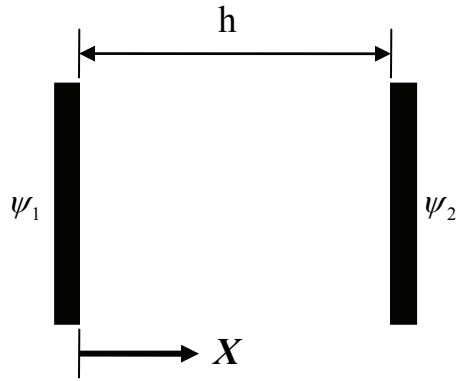
Figure 24. Diagram showing two plates and coordinate system

Because the Poisson-Boltzmann equation is highly nonlinear, it can not have analytical closed form solutions. But, by the low electric potential assumption, it can be linearized given by

$$\frac{d^2\psi}{dX^2} = \frac{2z^2e^2c_b}{\varepsilon\varepsilon_0 kT}\psi \qquad (51)$$

The solution to the linearized Poisson-Boltzmann equation (51) for two parallel plates separated by a gap of distance h with the boundary conditions $\psi(X=0)=\psi_1$ and $\psi(X=h)=\psi_2$ is

$$\psi = \psi_1 \cosh(\kappa X) + \frac{\psi_2 - \psi_1 \cosh(\kappa h)}{\sinh(\kappa h)} \sinh(\kappa X) \tag{52}$$

The electrochemical force per unit length is given by substituting equation (52) into equation (48) and (49) yielding to

$$f_{EC} = w\varepsilon\varepsilon_0\kappa^2 \frac{\psi_1^2}{\sinh^2(\kappa h)} \left[\frac{\psi_2}{\psi_1}\cosh(\kappa h) - \frac{1}{2}\left[1 + \left(\frac{\psi_2}{\psi_1}\right)^2\right]\right] \tag{53}$$

where $1/\kappa^2 = \varepsilon\varepsilon_0 kT / 2e^2 z^2 c_b$, and $1/\kappa = \lambda_{DL}$ is the Debye length.

It should be noted here that the fringing field correction is not considered in this model. Neglecting the fringing field makes the analysis simpler and still provides useful insights. The electrostatic force considering the fringing field effect is larger than that neglecting it. So, it should be noted that the electrostatic force in our model is underestimated. The fringing field effect will be briefly introduced in section 3.3.

Consequently, the governing equation has eleven design parameters ; ψ_1, ψ_2, c_b, T, A_h, ε, $\tilde{E}$, h_0, w, t and L.

3.2.3. Nondimensional parameterization of the model

For convenience, the model is written in nondimensional form. The chemical and electrical forces per unit beam length can be written in terms of the nondimensional potential $\phi = ez\psi / kT$ as

$$f_C = 2c_b kTw(\cosh\phi - 1) \tag{54}$$

and

$$f_E = -\frac{c_b kTw}{\kappa^2}|\nabla\phi|^2 \tag{55}$$

The linearized nondimensional Poisson-Boltzmann equation is given by

$$\nabla^2\phi = \kappa^2\phi \tag{56}$$

With the solution to the equation (56) for the boundary conditions $\phi(x = 0) = \phi_1$ and $\phi(x = h) = \phi_2$, the electrochemical force is given by

$$f_{EC} = 2wc_b kT\phi_1^2 \frac{1}{\sinh^2(\kappa h)}\left[\frac{\phi_2}{\phi_1}\cosh(\kappa h) - \frac{1}{2}\left[1 + \left(\frac{\phi_2}{\phi_1}\right)^2\right]\right] \tag{57}$$

Introducing the nondimensional variables

$$h^* = \frac{h}{h_0} = \frac{h_0 + u}{h_0}, \quad x^* = \frac{x}{L} \tag{58}$$

The following nondimensional form is obtained :

$$\frac{d^4 h^*}{dx^{*4}} = F_{vdW} + F_{EC} \tag{59}$$

$$F_{vdW} = -\frac{\alpha}{h^{*3}} \tag{60}$$

$$F_{EC} = \frac{\beta}{\sinh^2(\xi_0 h^*)} \left[\frac{\phi_2}{\phi_1} \cosh(\xi_0 h^*) - \frac{1}{2} \left[1 + \left(\frac{\phi_2}{\phi_1} \right)^2 \right] \right] \qquad (61)$$

where $\xi_0 = \kappa h_0$. The nondimensional parameters appearing in equation (60-61) are

$$\alpha = w \frac{A_h}{6\pi h_0^4} \frac{L^4}{\tilde{E}I}, \qquad \beta = w \frac{2c_b kT \phi_1^2}{h_0} \frac{L^4}{\tilde{E}I} \qquad (62)$$

Consequently, the governing equation has the following four nondimensionalized parameters α, β, ξ_0 and ϕ_2 / ϕ_1.

The governing equations are solved using the finite element software available from COMSOL.

3.2.4. Detachment length

The maximum length of the MEMS/NEMS structure that does not stick to the substrate without the application of external voltage is called the detachment length, which is a basic design parameter for MEMS/NEMS [49].

The detachment length of the cantilever beam in the air can be obtained by the critical value of α. That is, the detachment length of the cantilever beam that will not adhere to the substrate due to the van der Waals force is [49]

$$L_{max} = h_0 \sqrt[4]{\frac{\pi \tilde{E} t^3 \alpha_c}{2 A_h}} \qquad (63)$$

As an alternative case, if the length of the switch is known, one can calculate the minimum gap between the switch and the substrate to ensure that the switch does not adhere to the substrate due to the van der Waals force [49],

$$h_{0\min} = L\sqrt[4]{\frac{2A_h}{\pi \tilde{E} t^3 \alpha_c}} \tag{64}$$

From equation (62) and (64), the minimum gap between the switch and the substrate in liquid to ensure that the switch does not adhere to the substrate is give by

$$h_{0\min} = \sqrt[3]{\frac{\beta}{12\pi kT\alpha_c} \frac{A_h}{n_\infty \phi_1^2}} \tag{65}$$

3.3. Fringing Field Effect

In many electrostatic actuators that are fabricated by current micromachining processes, the gap between the electrodes is not negligible relative to the lateral dimensions of the deformable capacitor. Therefore, fringing fields are considerable and must be accounted for when modeling the electrostatic forces.

Generally speaking, the exact value of the electrostatic force cannot be found in a closed form and can only be calculated by numerical methods based on the MPB equation. However, it needs a 3-D analysis to consider the fringing field effect and it is too costly. Approximate relations have been found that use a capacitor model to calculate the electrostatic force.

3.3.1. Capacitance of general dielectric capacitor

The exact value of the capacitance of a capacitor also cannot be found in a closed form. For the parallel-plate capacitor with finite plate thickness as shown in figure 25, the capacitance per unit length considering the fringing fiends is given in equation (66) [50].
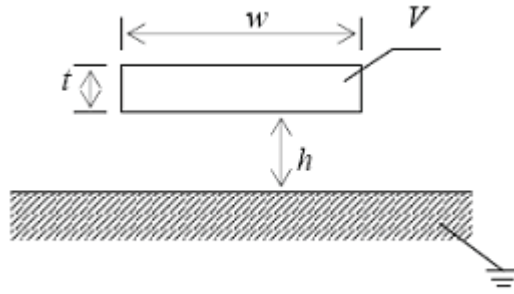
Figure 25. Electrostatic capacitor [50]

$$C = \varepsilon \frac{w}{h}\left[1 + \frac{2h}{\pi w}\ln\left(\frac{\pi w}{h}\right) + \frac{2h}{\pi w}\ln\left(1 + \frac{2t}{h} + 2\sqrt{\frac{t}{h} + \frac{t^2}{h^2}}\right)\right] \qquad (66)$$

Once C is known, the electrostatic force per unit length on the movable electrode neglecting the effect of thickness can be found as

$$f_E = -\frac{1}{2}\frac{\partial C}{\partial h}V^2 = \frac{\varepsilon w V^2}{2h^2}(1 + 0.65\frac{h}{w}) \qquad (67)$$

3.3.2. Double-layer capacitance

The electrochemical double-layer is assumed to be a series of two capacitors as shown in figure 26. C_S and C_d denote the compact Stern layer capacitance and the diffuse layer capacitance, respectively.
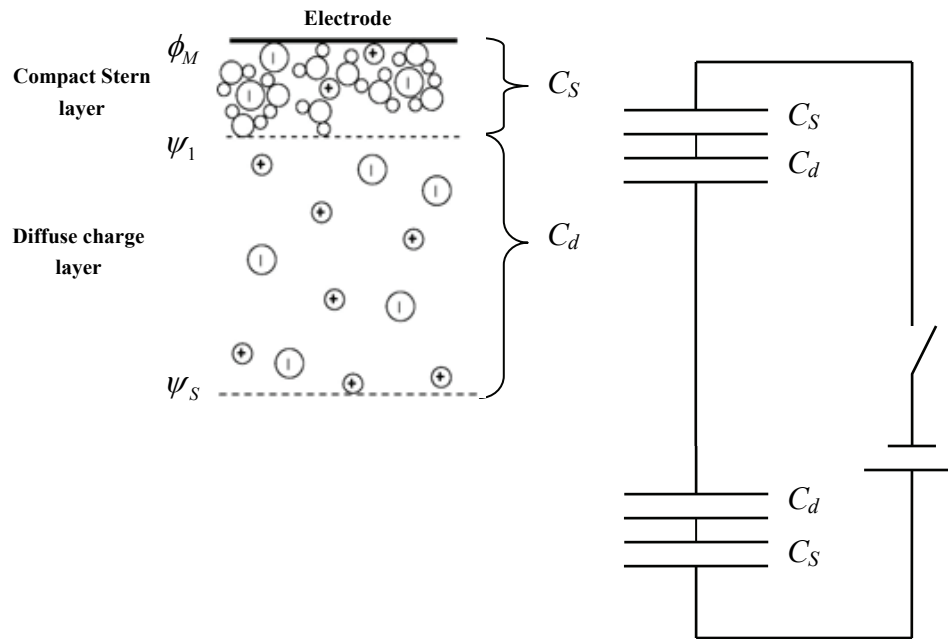
Figure 26. Double-layer capacitance

The total capacitance of the double layer, C_{DL}, is then

$$\frac{1}{C_{DL}} = \frac{1}{C_S} + \frac{1}{C_d}$$ (68)

The Helmholtz type compact layer capacitance is

$$C_S = \frac{\varepsilon}{a} w$$ (69)

where a is the Helmholtz layer thickness which is generally assumed to be an ion size.

Chapman gave a simple form for the charge-voltage relation of the diffuse-layer capacitor, which, upon differentiation, yields a simple formula for the nonlinear differential capacitance of the diffuse layer [20]

$$C_D = \frac{\varepsilon}{\lambda_{DL}} w \cosh\left(\frac{ze(\psi_1 - \psi_S)}{2kT}\right) \tag{70}$$

where $\lambda_{DL} = \left(\varepsilon\varepsilon_0 kT / 2e^2 z^2 c_b\right)^{1/2}$ is the Debye length.

Equations (68-70) lead to the total double-layer capacitance as

$$C_{DL} = \frac{\dfrac{\varepsilon}{a}\dfrac{\varepsilon}{\lambda_{DL}}\cosh\left(\dfrac{ze(\psi_1 - \psi_S)}{2kT}\right)}{\dfrac{\varepsilon}{a} + \dfrac{\varepsilon}{\lambda_{DL}}\cosh\left(\dfrac{ze(\psi_1 - \psi_S)}{2kT}\right)} w \tag{71}$$

This double-layer capacitance is a function of a potential at the interface between the compact layer and diffuse layer, ψ_1, and a potential at the interface between the diffuse layer and bulk solution, ψ_S, which need to be obtained by solving nonlinear PB equation numerically.

A more simplified model is the linear Debye-Hückel model. The double-layer capacitance is simply given as the dielectric constant of solvent divided by the Debye length,

$$C_{DL} = \frac{\varepsilon}{\lambda_{DL}} w \tag{72}$$

The double-layer capacitance considering the fringing field can be written as equation (73) from equation (66).

$$C_{DL} = \varepsilon \frac{w}{\lambda_{DL}}\left[1 + \frac{2\lambda_{DL}}{\pi w}\ln\left(\frac{\pi w}{\lambda_{DL}}\right) + \frac{2\lambda_{DL}}{\pi w}\ln\left(1 + \frac{2t}{\lambda_{DL}} + 2\sqrt{\frac{t}{\lambda_{DL}} + \frac{t^2}{\lambda_{DL}^2}}\right)\right] \tag{73}$$

The electrostatic force per unit length on the movable electrode neglecting the effect of thickness is then,

$$f_E = -\frac{1}{2}\frac{\partial C_{DL}}{\partial \lambda_{DL}}(\phi_M - \psi_S)^2 = \frac{\varepsilon w(\phi_M - \psi_S)^2}{2\lambda_{DL}{}^2}(1 + f_f) \qquad (74)$$

where the fringing correction factor is

$$f_f = 0.65\frac{\lambda_{DL}}{w} \qquad (75)$$

The fringing field effect decreases as the ratio of the Debye length to the capacitor width, λ_{DL}/w, decreases as shown in figure 27.
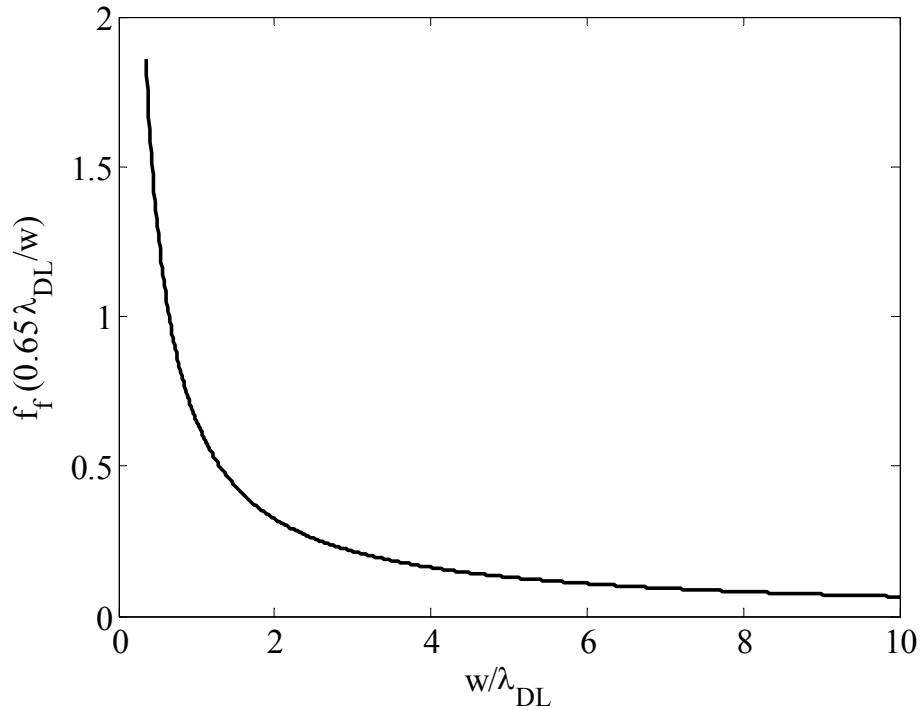

Figure 27. Fringing field correction factor vs w/λ_{DL}

The Debye length is a function of bulk ion concentration. It increases as the bulk ion concentration decreases. In room temperature, the Debye lengths are 0.3nm and 0.97nm when the ion concentration is 1M and 0.1M, respectively. General dimensions of

cantilever beam width and initial gap distance between the beam and substrate we are interested in are around 5nm, which lead the aspect ratio, w / λ_{DL}, to 16 and 5 for ion concentration of 1M and 0.1M, respectively. The fringing field effects are 5% for 1M and 13% for 0.1M. The fringing field effect is significant and increases as the ion concentration decreases.

The double-layer capacitor model will not be valid for low ion concentration. The Debye length is about 3nm when the bulk ion concentration is 0.01M. If the initial gap distance between the cantilever beam and the substrate is 5nm, the double-layer lengths from each electrode are overlapped. So, the double-layer capacitor model is very limited to be used in our nano beam model.

3-D numerical simulations should be a future work to consider the accurate electrostatic force including the fringing field effects.

3.4. Results for Gas or Vacuum

Before solving problems in liquids, the model and finite element solution will first be tested against published solutions for the bending of cantilever beams in gas or vacuum.

The case of zero electrochemical force, $\beta = 0$, is first considered. If the gap between the cantilever beam and the substrate is small enough, the beam can collapse onto the ground plane due to the van der Waals force. The critical value of α is determined from a plot of α versus the normalized tip deflection u_0, figure 28.

$$u_0 = \frac{u}{h_0}\bigg|_{(x^*=1)} \tag{76}$$
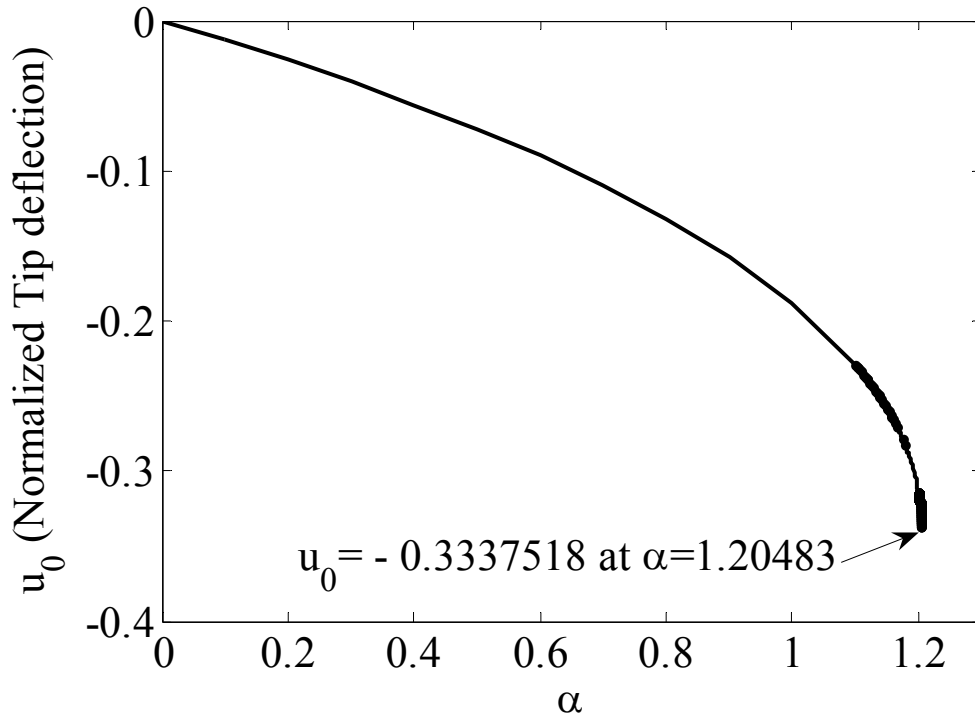
Figure 28. α versus u_0 when $\beta = 0$

From this figure, one finds the critical value of $\alpha_c = 1.20483$ which occurs at $u_{0c} = -0.3375$. This is very close to the overestimated close-form solutions assuming an appropriate shape function for the beam deflection to evaluate the integrals by Ramezani *et al* [36], the critical value of $\alpha_c = 1.313$ and $u_{0c} = -0.359$.

The case in which the beam is a double-wall carbon nanotube (DWCNT) suspended above a graphite substrate is next considered. Dequesnes *et al* [33] studied the pull-in voltage characteristics of nanotube electromechanical switches, suspended over a graphitic ground electrode with parameterized continuum models for three coupled energy domains: the elastostatic energy domain, the electrostatic energy domain and the

van der Waals energy domain. They showed that their numerical simulations based on continuum models closely match the experimental data reported for carbon nanotube-based nanotweezers. In this section, our FEA results will be verified by comparing them to the results of Dequesnes *et al* [33].
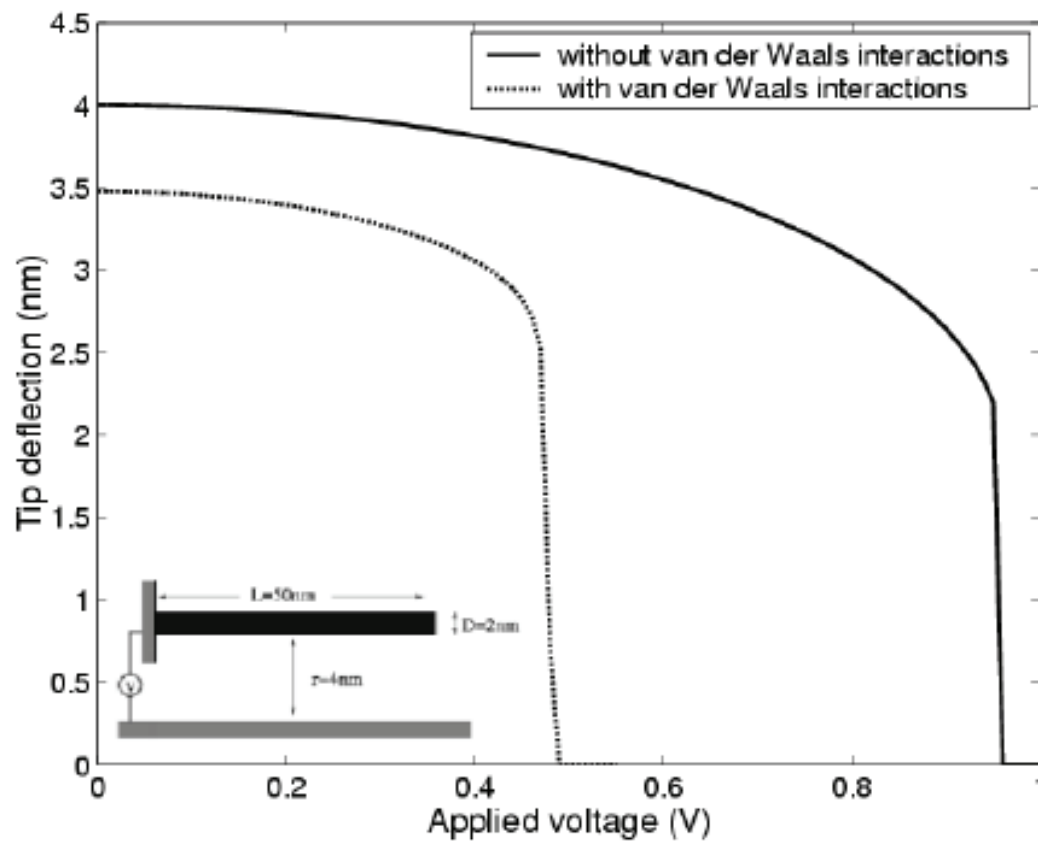

Figure 29. Dequesnes *et al* results for a cantilever beam [33]
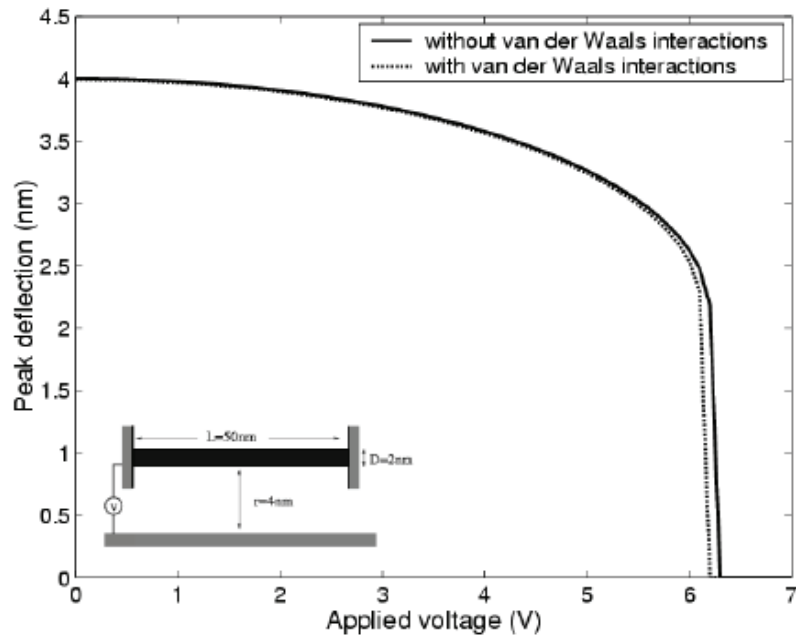
Figure 30. Dequesnes *et al* results for a fixed-fixed beam [33]
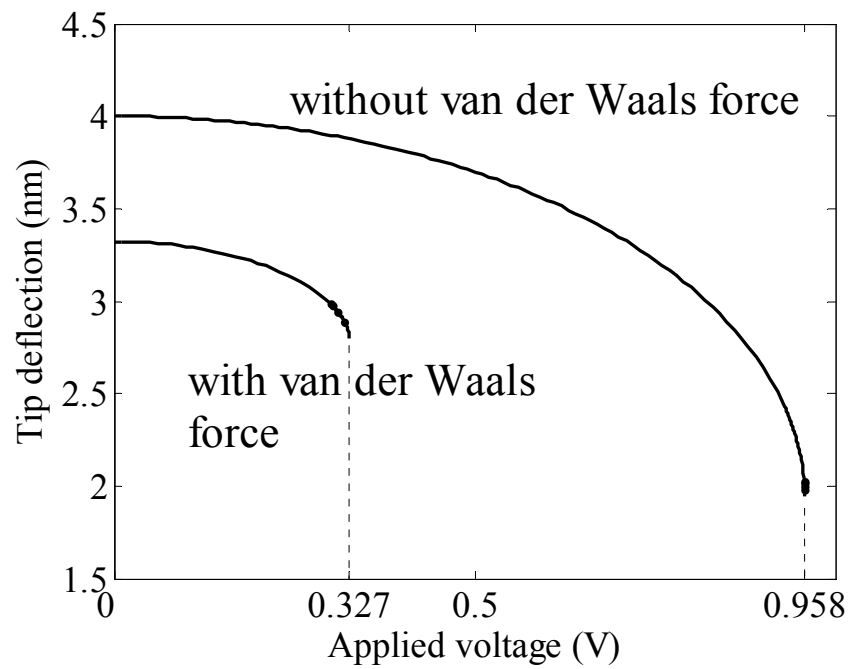
Figure 31. FEA results for a cantilever beam
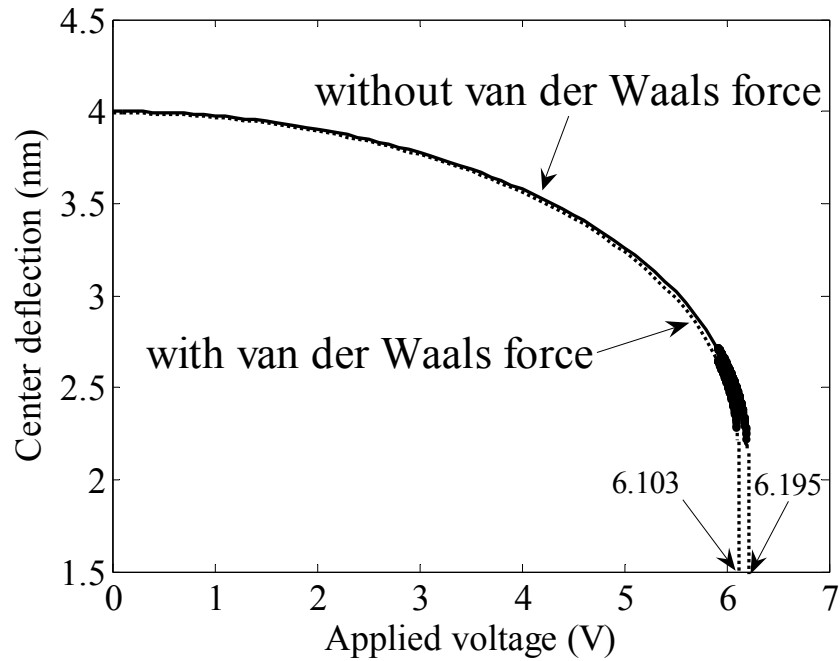
Figure 32. FEA results for a fixed-fixed beam

As shown in Figures 29-32, the FEA results are closely matched with Dequesnes *et al's* [33] numerical results for DWNT cantilever switch (figure 29) and DWNT fixed-fixed switch (figure 30), which is 50nm long and has a diameter of 2nm and is positioned 4nm above the ground plane. The pull-in voltages are compared in table 1.

Table 1. Pull-in voltage comparison

Pull-in voltage (V) Beam type/ results		Without van der Waals force	With van der Waals force
Cantilever switch	Dequesnes	0.97	0.48
	Present FEA	0.958	0.328
Fixed-fixed switch	Dequesnes	6.3	6.2
	Present FEA	6.195	6.013

3.5. Results for Liquid Electrolyte

3.5.1. No van der Waals force

Neglecting the van der Waals force is a common practice in MEMS literatures. When there is no effect of the van der Waals force, β is plotted as a function of u_0 for various ξ_0 and ϕ_2/ϕ_1 values. Van der Waals force is always attractive. But the electrochemical force can be attractive or repulsive according to ξ_0 and ϕ_2/ϕ_1. When the electrochemical force is attractive, i.e. $F_{EC} < 0$, the total force is always attractive and the cantilever beam bends toward the ground. In other words, α and β have critical values which make the pull-in behavior. When the electrochemical force is repulsive, i.e. $F_{EC} > 0$, the total force can be attractive or repulsive. The total force is attractive, i.e. $F_{total} = F_{vdW} + F_{EC} < 0$, when $|F_{vdW}| > |F_{EC}|$. In this case, the cantilever beam still bends toward the ground and α has critical values. However, the total force is repulsive, i.e. $F_{total} = F_{vdW} + F_{EC} > 0$ when $|F_{vdW}| < |F_{EC}|$, the cantilever beam bends away form the substrate, and there is no pull-in instability. Figure 33 shows the region in which the electrochemical force is repulsive. For visual simplicity, attractive forces are not shown.

(a)

(b)
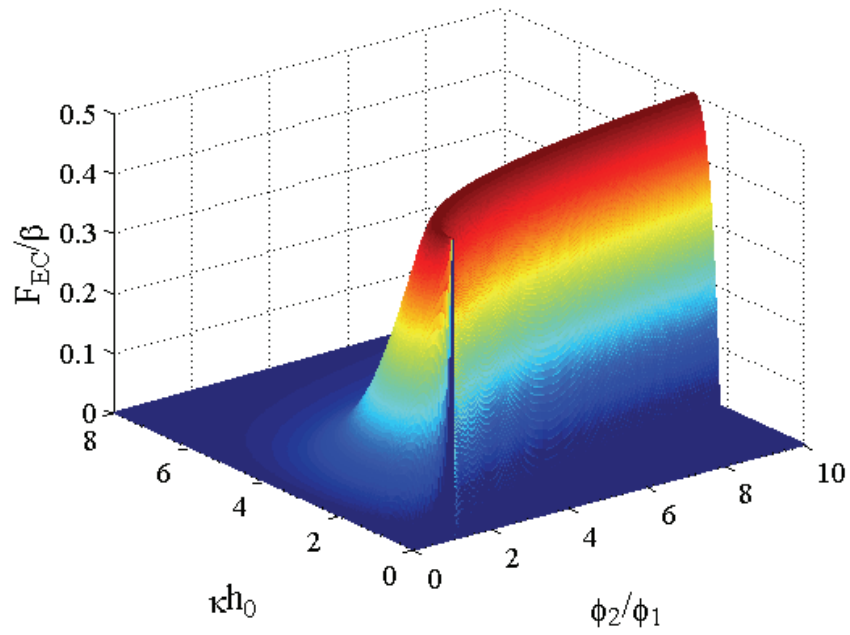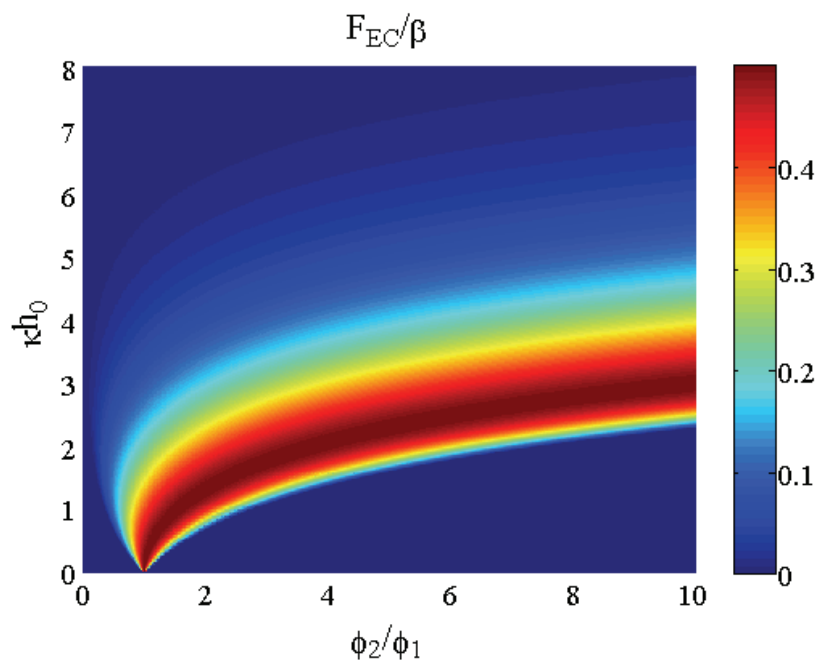
Figure 33. F_{EC}/β distributions according to ξ_0 and ϕ_2/ϕ_1

For attractive forces, Figures 34-37 give the critical values of β with various combinations of ξ_0 and ϕ_2/ϕ_1 when $\alpha = 0$, i.e. there is no van der Waals force.
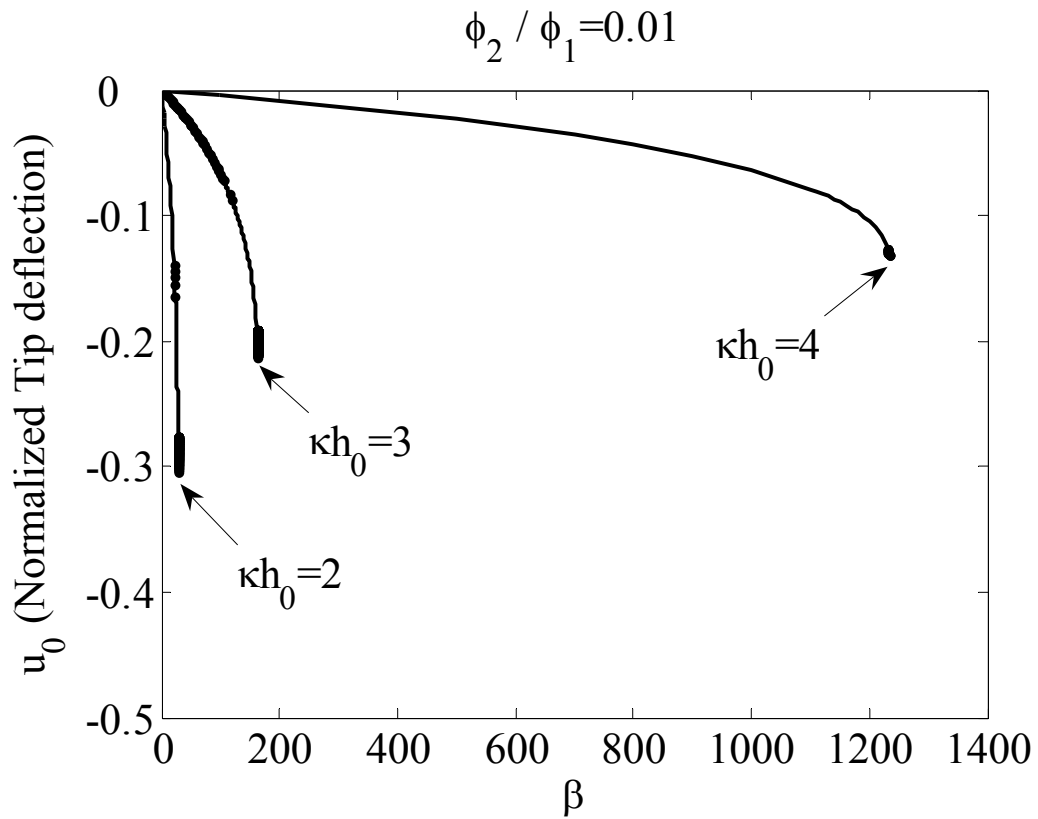
$$\phi_2 / \phi_1 = 0.01$$

Figure 34. β versus u_0 with various combinations of ξ_0 when $\phi_2/\phi_1 = 0.01$
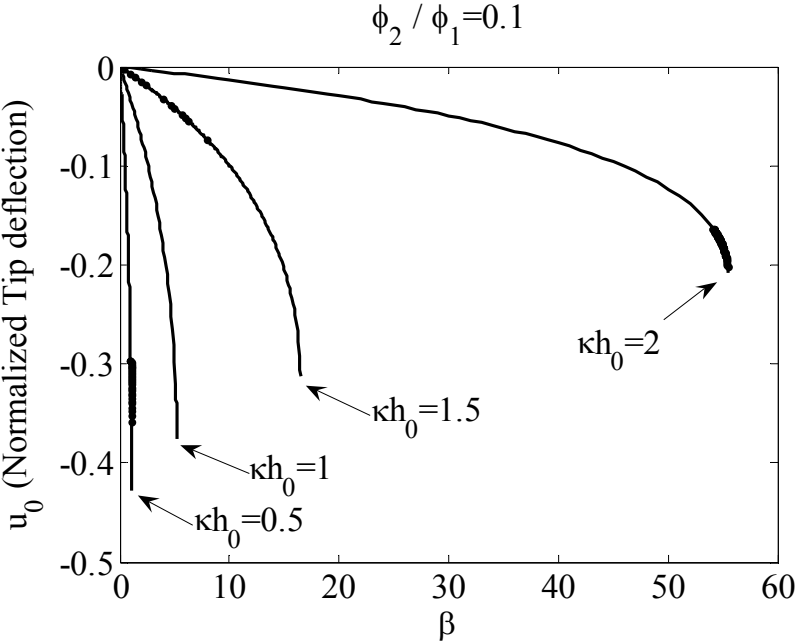
Figure 35. β versus u_0 with various combinations of ξ_0 when $\phi_2 / \phi_1 = 0.1$
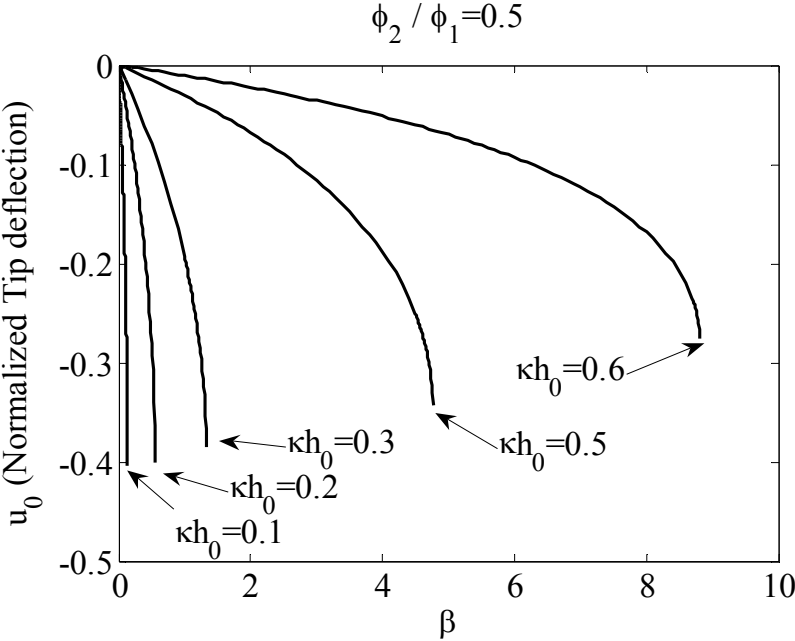
Figure 36. β versus u_0 with various combinations of ξ_0 when $\phi_2 / \phi_1 = 0.5$
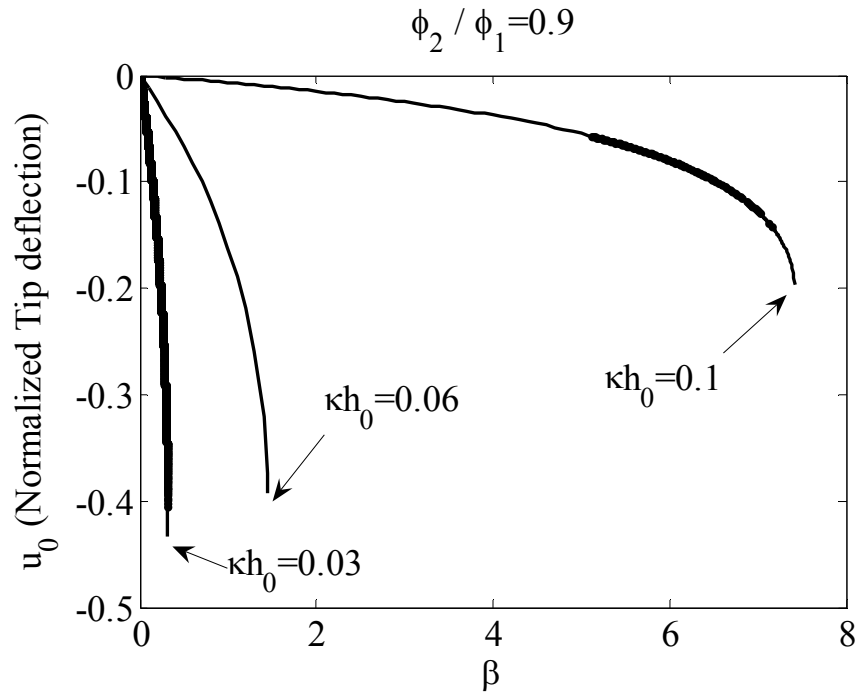
$$\phi_2 / \phi_1 = 0.9$$

Figure 37. β versus u_0 with various combinations of ξ_0 when $\phi_2 / \phi_1 = 0.9$

3.5.2. Presence of both electrochemical and van der Waals forces

In general case that the electrochemical and van der Waals interactions exist simultaneously, the effects of each force on the pull-in parameters of the nano cantilever beam are investigated. Assuming that $\xi_0 = 4$ and $\phi_2 / \phi_1 = 0.01$, α is plotted versus u_0 for various β values in figure 38.

Figure 38. α versus u_0 with various β

In the case of $\beta = 400$, the critical value of $\alpha_c = 0.6811$ which occurs at $u_{0c} = -0.2263$. Table 2 shows the parametric study results for various cases. Other parametric study results are summarized in table 2.

Table 2. Parametric study results

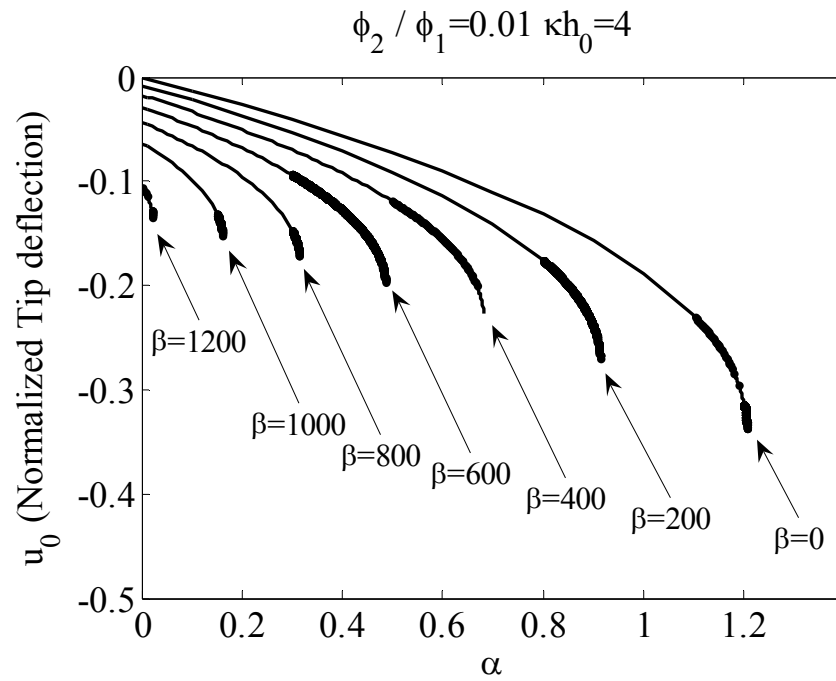|	α	β	ϕ_2 / ϕ_1	κh_0	u_0
1	0	4.05	0.01	1	-0.39978
2	0	27.692	0.01	2	-0.305848
3	0	162.009	0.01	3	-0.212862
4	0	1233.2	0.01	4	-0.133896
5	0	∞	0.01	5	positive
6	0	1.096	0.1	0.5	-0.428081
7	0	5.22	0.1	1	-0.376256
8	0	16.47	0.1	1.5	-0.312423
9	0	55.46	0.1	2	-0.207381
10	0	∞	0.1	2.5	positive
11	0	0.1359	0.5	0.1	-0.432657
12	0	0.562	0.5	0.2	-0.425367
13	0	1.346	0.5	0.3	-0.408152
14	0	4.772	0.5	0.5	-0.347872
15	0	8.811	0.5	0.6	-0.27732
16	0	∞	0.5	0.7	positive
17	0	0.3148	0.9	0.03	-0.433764
18	0	1.444	0.9	0.06	-0.393216
19	0	7.42	0.9	0.1	-0.197486
20	0	∞	0.9	0.2	positive
21	1.20483	0			-0.337518
22	0.913	200	0.01	4	-0.270582
23	0.6811	400	0.01	4	-0.226315
24	0.4855	600	0.01	4	-0.198299
25	0.3141	800	0.01	4	-0.173761
26	0.1609	1000	0.01	4	-0.153566
27	0.0219	1200	0.01	4	-0.136415

3.5.3. Case study with silicon nanoswitch

A cantilever type nanoswitch made of silicon is considered as an example with the known parameters in table 3.

Table 3. Geometrical parameters of a nanoswitch

Geometrical parameter	Value (nm)
L	200
t	10
h_0	10
Material parameter (Silcon)	Value
E	110 (GPa)
A_h	1×10^{-20} (J)
Input parameter	Value
ϕ_1	1.5576 ($\Psi_1 = 40mV$)
c_b	Input value
ϕ_2 / ϕ_1	Input value

For given known parameters, the four nondimensionalized parameters are $\alpha = 0.0093$, $\beta = 86.4878 c_b \phi_1^2$, $\xi_0 = 32.5691\sqrt{c_b}$ and ϕ_2 / ϕ_1. The normalized tip deflection, F_{EC} and F_{vdW} are plotted with various c_b and ϕ_2 / ϕ_1 values in Figures 39-42. T*he beam deflection is not a monotonic function* of the ratio ϕ_2 / ϕ_1 and κh_0, i.e. as ϕ_2 / ϕ_1 and κh_0 are increased, the beam bends upward and then downward.
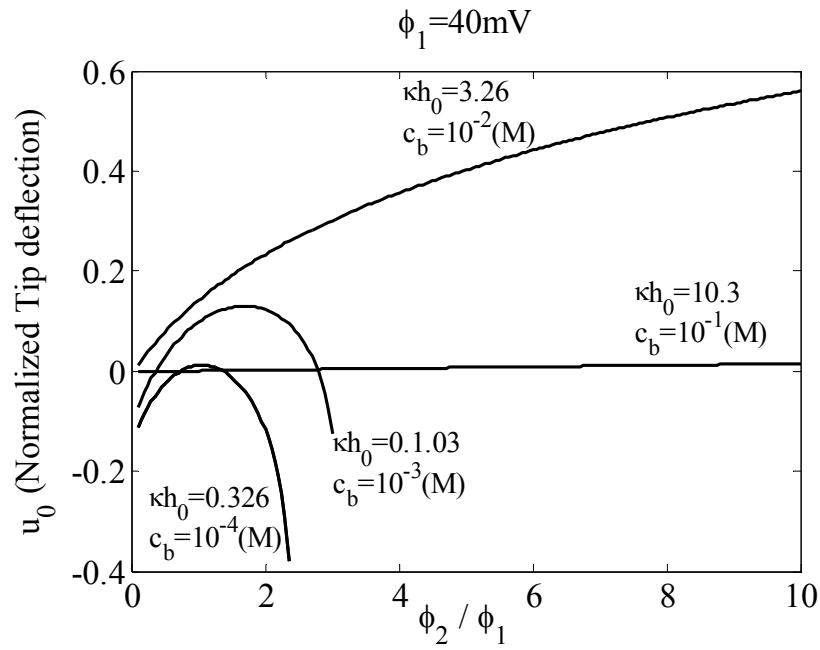
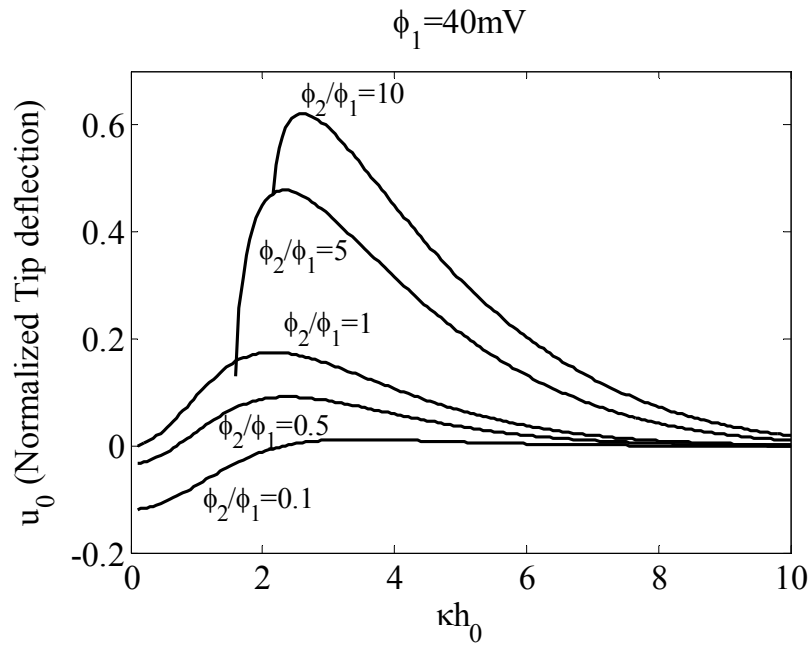Figure 39. u_0 versus ϕ_2 / ϕ_1 with various c_b when $\phi_1 = 40\text{mV}$

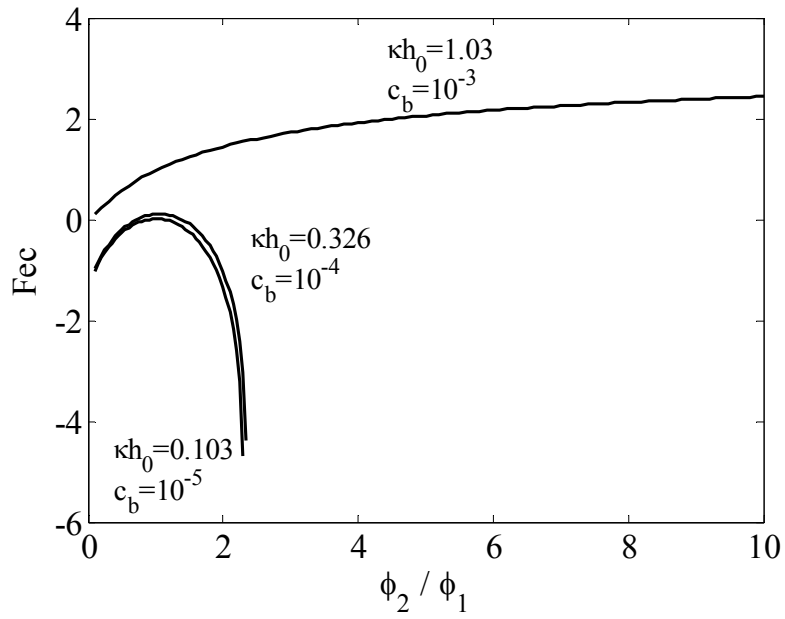Figure 40. u_0 versus κh_0 with various ϕ_2 / ϕ_1 when $\phi_1 = 40\text{mV}$

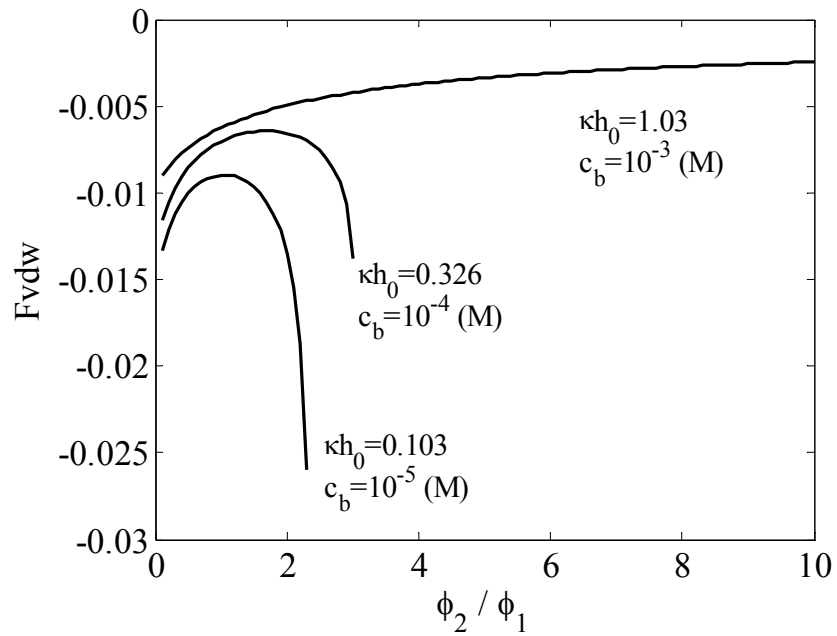Figure 41. F_{ec} versus ϕ_2 / ϕ_1 with various c_b

Figure 42. F_{vdw} versus ϕ_2 / ϕ_1 with various c_b

3.5.4. Case study with DWNT

The DWNT cantilever beam switch in the liquid electrolyte which has the same geometrical parameters with the DWNT cantilever in section 3.3.1 is studied in this section. The parameters are shown in table 4. The bulk ion concentration and the temperature are fixed as $c_b = 0.01\text{M}$ and $T = 298\text{K}$, respectively.

Table 4. Geometrical parameters of a DWCNT

Geometrical parameter	Value (nm)
L	50
D (Diameter)	2
h_0	4
Material parameter	Value
E	1.2 (TPa)

Figures 43-44 show the DWNT tip deflection as a function of the electric potential applied to the DWNT, ψ_1, when the applied potential to the bottom plane, ψ_2, is set to be same magnitude but opposite sign, $\psi_2 = -\psi_1$. It should be noted that the effect of the electrolyte to the van der Waals force is not considered. The pull-in voltage of the DWNT in liquids electrolyte, $\Delta\psi$, was 0.074V, about five times smaller than the pull-in voltage of the DWNT in the air.
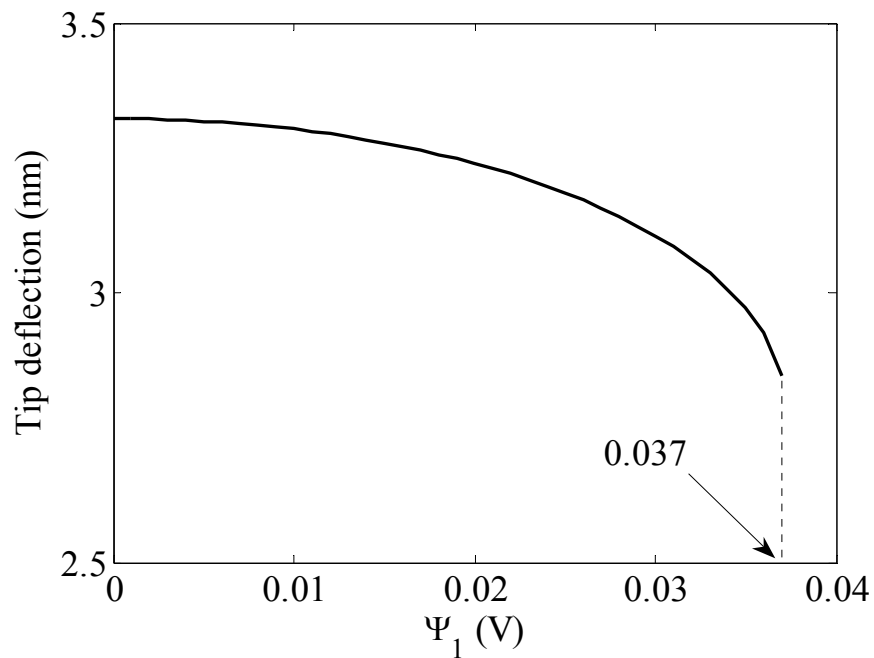
Figure 43. DWNT tip deflection vs ψ_1
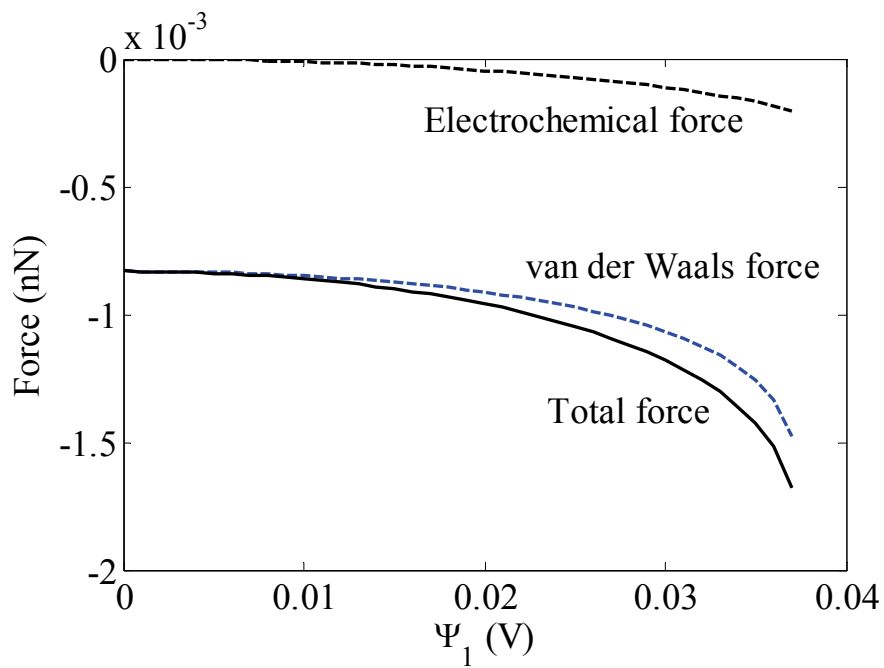
Figure 44. Forces vs ψ_1
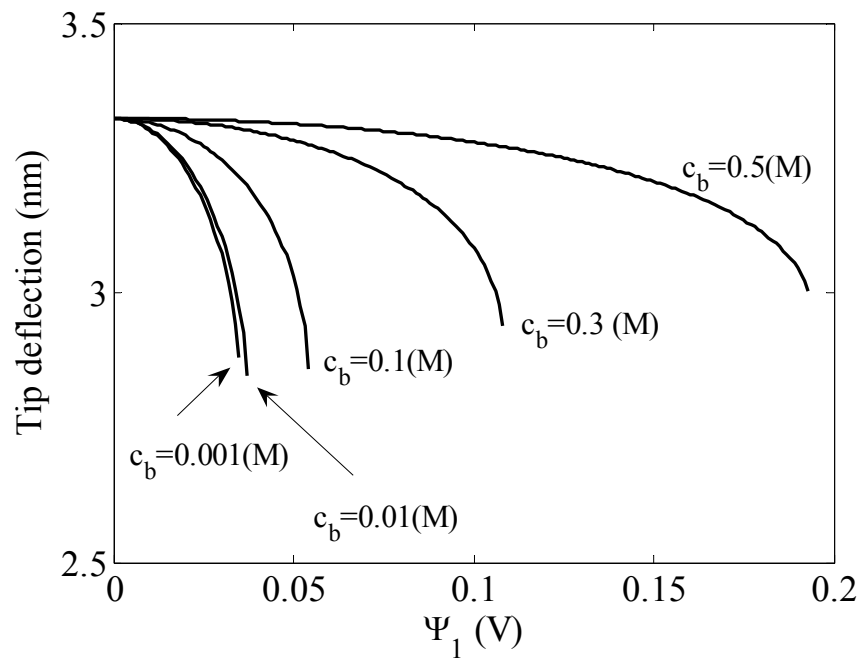
Figure 45. DWNT tip deflection vs ψ_1

The DWNT tip deflections as a function of ψ_1 with various values of bulk ion concentration are plotted in figure 45. As the bulk ion concentration increases, the pull-in voltage increased. When the bulk ion concentration was 0.5 M, the pull-in voltage was larger than that in the air.
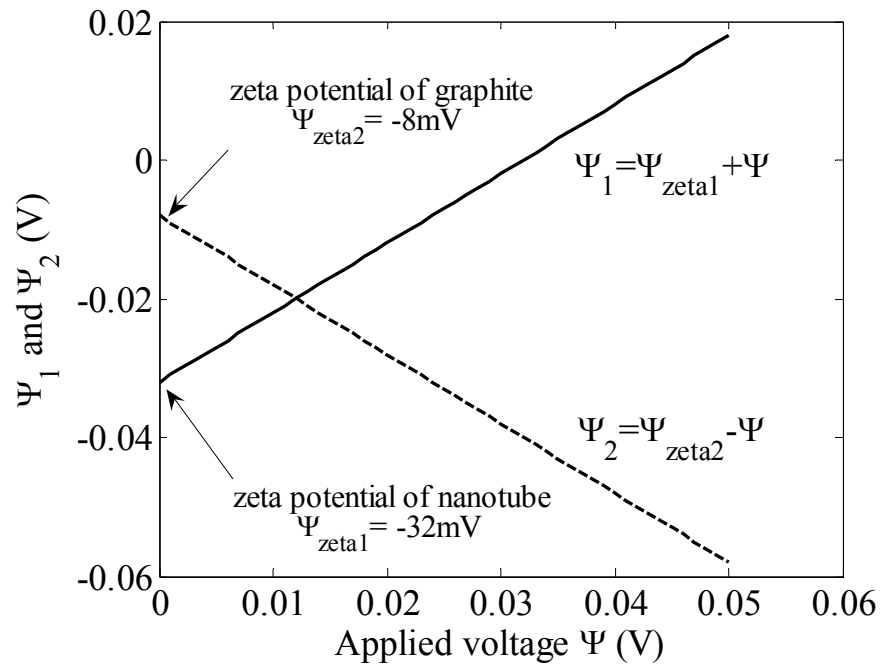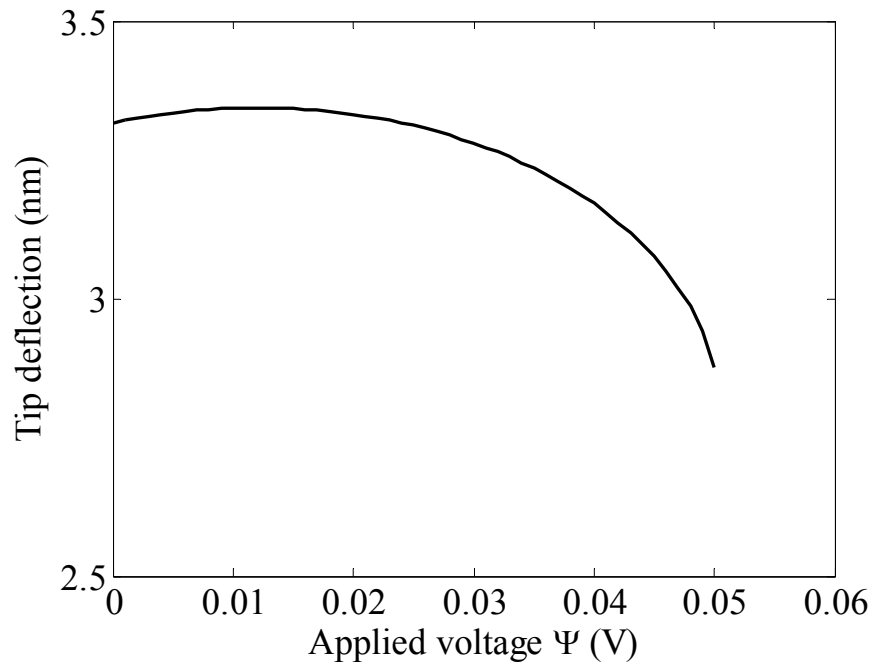
Figure 46. (a) Applied voltage and (b) tip deflection of DWCNT case 1
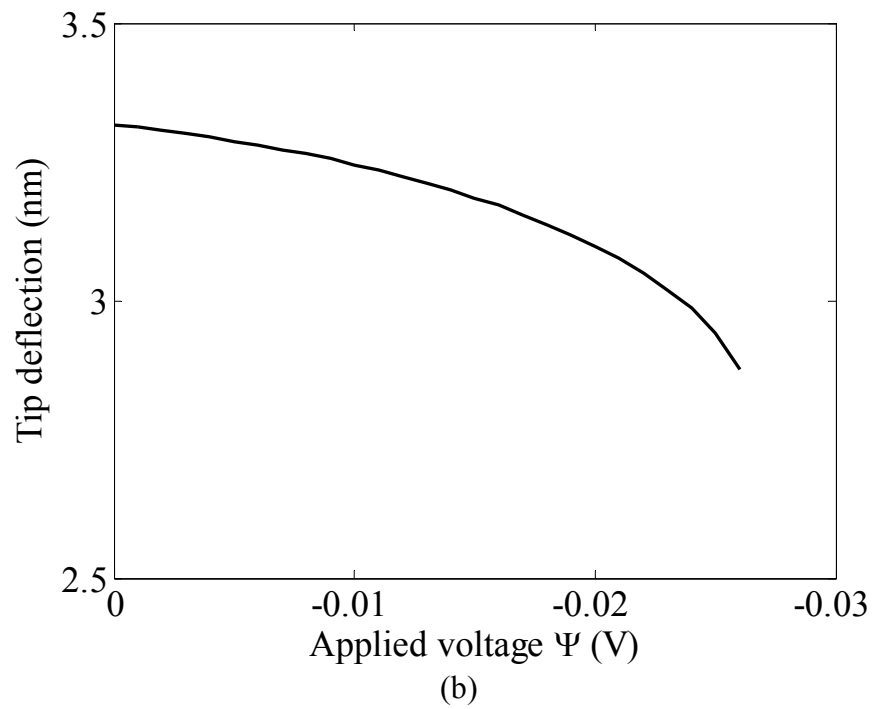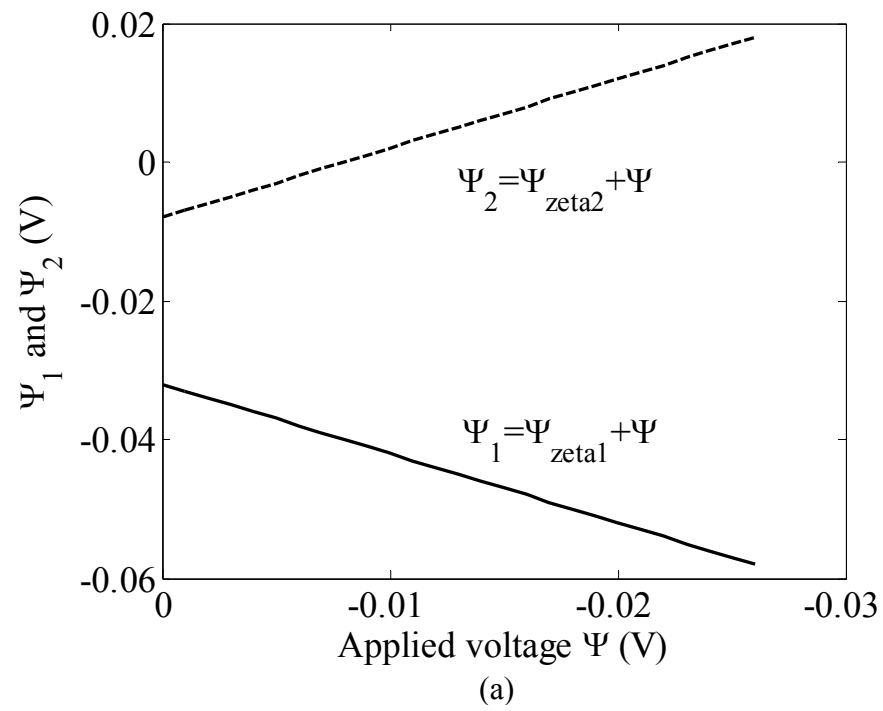
Figure 47. (a) Applied voltage and (b) tip deflection of DWCNT case 2
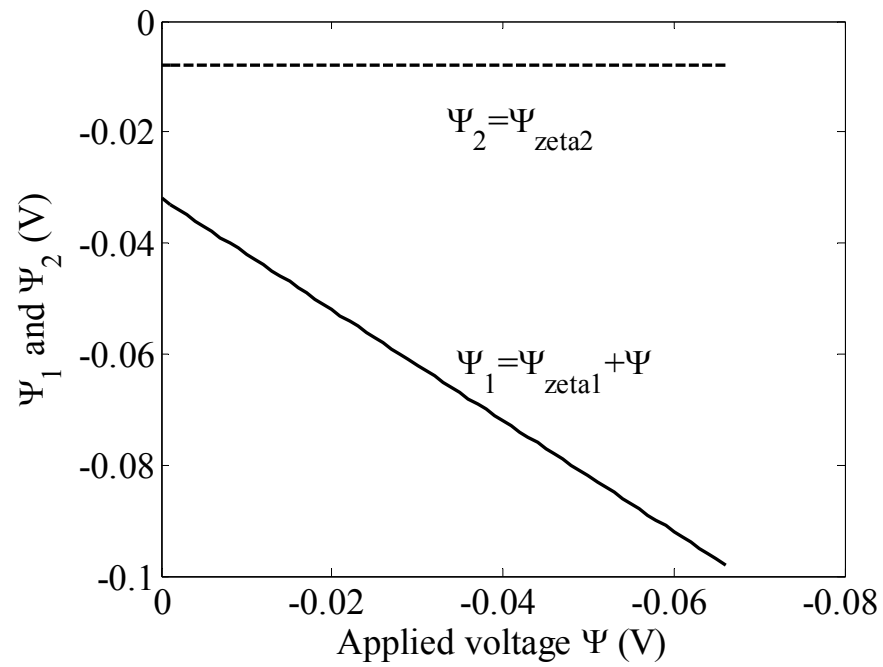
(a)
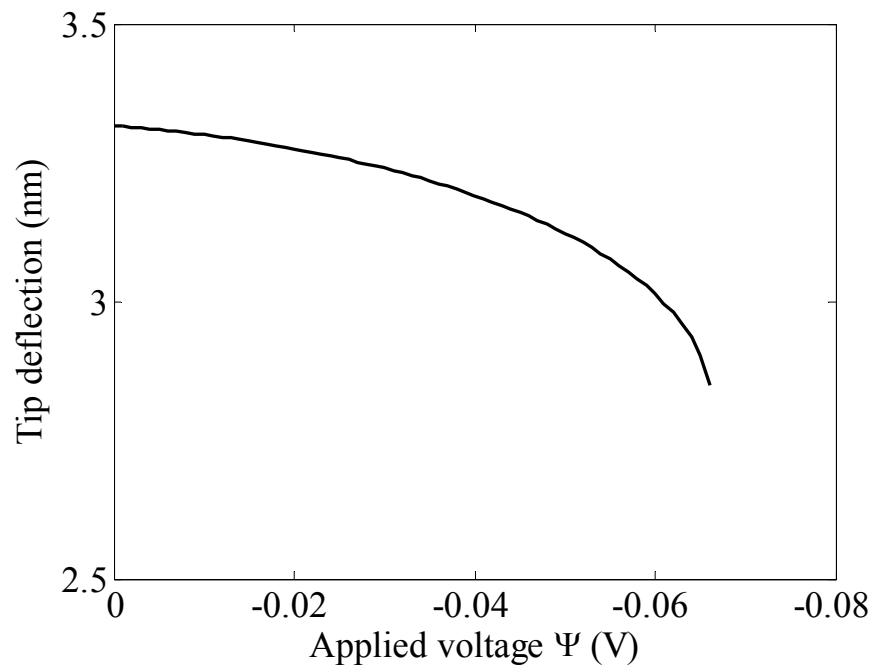
(b)

Figure 48. (a) Applied voltage and (b) tip deflection of DWCNT case 3

Figures 46-48 show three different cases for the tip deflection of the DWNT cantilever beam in liquids when the bulk ion concentration is 0.1 M. Note that the critical tip deflection is the same as $u_{Tip} = 2.875$ with different electric potentials.

3.6. Summary

A beam suspended horizontally over a substrate was modeled using simple beam theory. The linearized Poisson-Boltzmann equation was used to determine the electric potential distribution between the beam and the substrate. The electric potential was then used to determine the electric force, the ion concentrations, and the (linearized) osmotic force. The van der Waals force was included. It was determined that the problem is governed by four nondimensional parameters. The governing equations were solved using the COMSOL finite element software. For a gas or vacuum, the finite element results were verified by comparing to published results.

NEMS operating in gas requires an understanding and analysis of three coupled energy domains: elastostatics, electrostatics and van der Waals interactions. NEMS in liquid electrolyte requires an understanding additional energy domain, the osmotic force due to the ion concentration differences. This additional osmotic force is the main factor that distinguish the NEMS in liquids from the NEMS in gas.

The electric force between the beam and substrate is always attractive and the osmotic force is always repulsive. The sum of these two forces, the electrochemical force, is usually attractive. However, the electrochemical force can be repulsive for a narrow range of the ion concentration, the initial separation and surface potentials. This

was demonstrated for the case of a silicon nanoswitch, in which the beam may bend up or down, depending on the values of the nondimensional parameters. Furthermore, T*he beam deflection is not a monotonic function* of the ratio ϕ_2 / ϕ_1 and κh_0, i.e. as ϕ_2 / ϕ_1 and κh_0 are increased, the beam bends upward and then downward.

A DWCNT switch suspended over a graphite substrate was studied in both gas and liquid. The pull-in voltage of the DWCNT in a liquid with bulk concentration of 0.01M is about five times smaller than the pull-in voltage in air. However, the pull-in voltage increases as the bulk ion concentration increases. For a bulk ion concentration of 0.5M, the pull-in voltage was larger in liquid than in air. The critical separation between the DWCNT and the substrate increases with the bulk ion concentration. However, for a given bulk ion concentration, the critical tip separation is independent of the electric potentials. Furthermore, the critical tip separation is about the same in liquid and air.

4. STICTION

4.1. Introduction

Suspended surface micro or nano structures are being used in the manufacturing of pressure and acceleration sensors such as airbag accelerometers for automobiles, active optical elements for projection displays, microrelays, gyros, optical switches and memory devices [2]. These structures are typically made by forming a layer of the plate or beam material on top of a sacrificial layer of another material and etching the sacrificial layer. Under certain fabrication conditions and in-use conditions, such structures can collapse and permanently adhere to their underlying substrates [51]. This is a fundamental failure mode in microelectromechanical systems (MEMS) and nanoelectromecahnical systems (NEMS).

By definition, stiction is a term for the unintentional adhesion of compliant microstructure surfaces when restoring forces are unable to overcome interfacial forces such as capillary, electrostatic, van der Waals, Casimir forces, and other kinds of chemical forces [52]. The types of forces that influence microscale devices are different from those that influence devices with conventional scale. This is because the size of a physical system bears a significant influence on the physical phenomena that dictate the dynamic behavior of that system [53]. For example, larger-scale systems are influenced by inertia effects to a much greater extent than smaller-scale systems, while smaller systems are more influenced by surface effects. Therefore, surface effects induce strong

adhesion, friction and wear are major problems limiting both the fabrication yield and operation lifetime of many MEMS and NEMS devices [54].

The stiction problem for devices can be divided into two categories: release-related stiction and in-use stiction. Release-related stiction occurs during the process of the sacrificial layer removal in fabrication of structures, and such stiction is caused primarily by capillary forces. In-use stiction usually occurs when successfully released structures are in operation [2].

After many years of intense research, the MEMS community has developed design rules and manufacturing methods to avoid stiction. van Spengen *et al* presented a theoretical model for stiction in MEMS due to the van der Waals forces [55]. There is a standard test (called the peel test) for measuring the adhesion (or stiction) energy of MEMS in gases. An array of cantilever beams are made such that they are parallel to, and separated from, a substrate. The beams are identical except for their length. The beams that are longer than the critical length bond to the substrate. The beams that are shorter than the critical length do not bond to the substrate. The adhered length of the beam is determined by minimizing the total energy, which is comprised of the elastic energy and the surface energy [56]. Atomic force microscopy is also used to directly measure the force of adhesion, or stiction energy, between two solids.

Stiction of NEMS in liquids is a new subject. We are unaware of any publications concerning this topic.

The objectives of this section are to identify the parameters that affect the beam stiction and conduct a parametric study to answer practical questions such as: under what

conditions can the standard beam stiction test (called the peel test) used in gas, also be used in liquids? How can the test be modified for liquids? What is the ion concentration that will free a stuck beam? If stiction occurs in a gas, will submersion in a liquid electrolyte free the beam? What is the ionic concentration hysteresis between pull-in and stiction release? In other words, after a given ionic concentration results in pull-in and stiction, what ionic concentration will free the beam?

4.2. Modeling

4.2.1. Modeling of the beam in gas by Mastrangelo and Hsu

Mastrangelo and Hsu [56] developed the beam model which is adhered to the bottom substrate in the air as following.
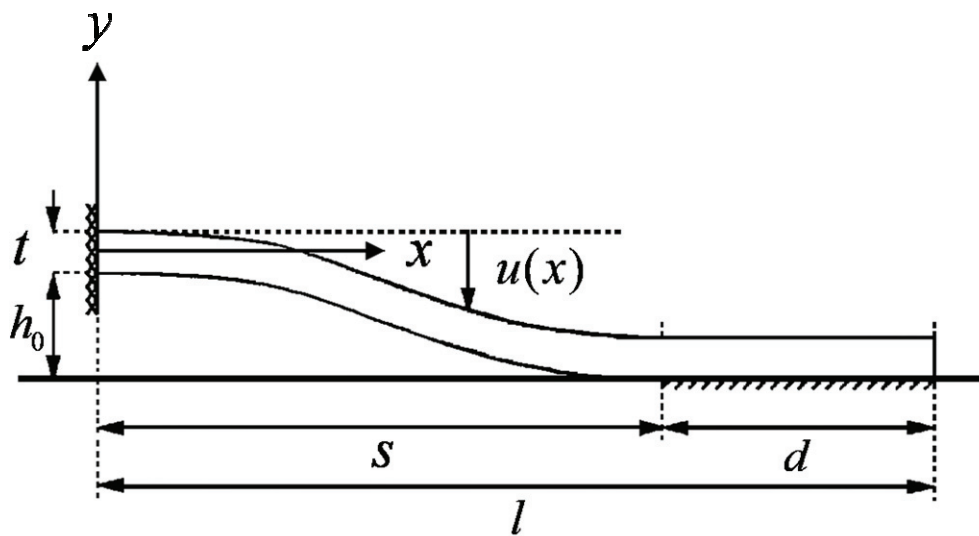

Figure 49. Cantilever beam adhering to its substrate

Figure 49 shows a cantilever beam of length l, width w, thickness t, height h_0, and Young's modulus E. The beam is adhering to the substrate a distance $d = l - s$ from the tip of the cantilever beam. Mastrangelo and Hsu assumed there is no external force applied to the beam. Since there is no external force acting on the beam, its deflection $u(x)$ is the solution of Euler-Bernoulli beam equation

$$EI \frac{d^4 u}{dx^4} = 0, \ I = \frac{wt^3}{12} \tag{77a-b}$$

where I is the moment of inertia of the beam respect to the z axis. The boundary conditions for equation (77) are given as

$$\left. \frac{du}{dx} \right|_0 = \left. \frac{du}{dx} \right|_s = 0, \ u(0) = 0, \ u(s) = -h_0 \tag{78a-c}$$

The solution of equation (77) is

$$u(x) = -h_0 \frac{x^2}{s^2} \left(3 - 2 \frac{x}{s} \right) \tag{79}$$

The shear deformation of the tip of the cantilever beam is not allowed with the slope boundary condition $du/dx = 0$ at $x = s$. However, shear deformation is important especially when s approaches l. Since the adhered distance, d, is very small, the tip of the cantilever beam "pivots" changing the elastic energy of the beam substantially just before detachment. This effect is considered as shown in figure 50. The beam is divided into two regions, adhesion free region and adhered region.
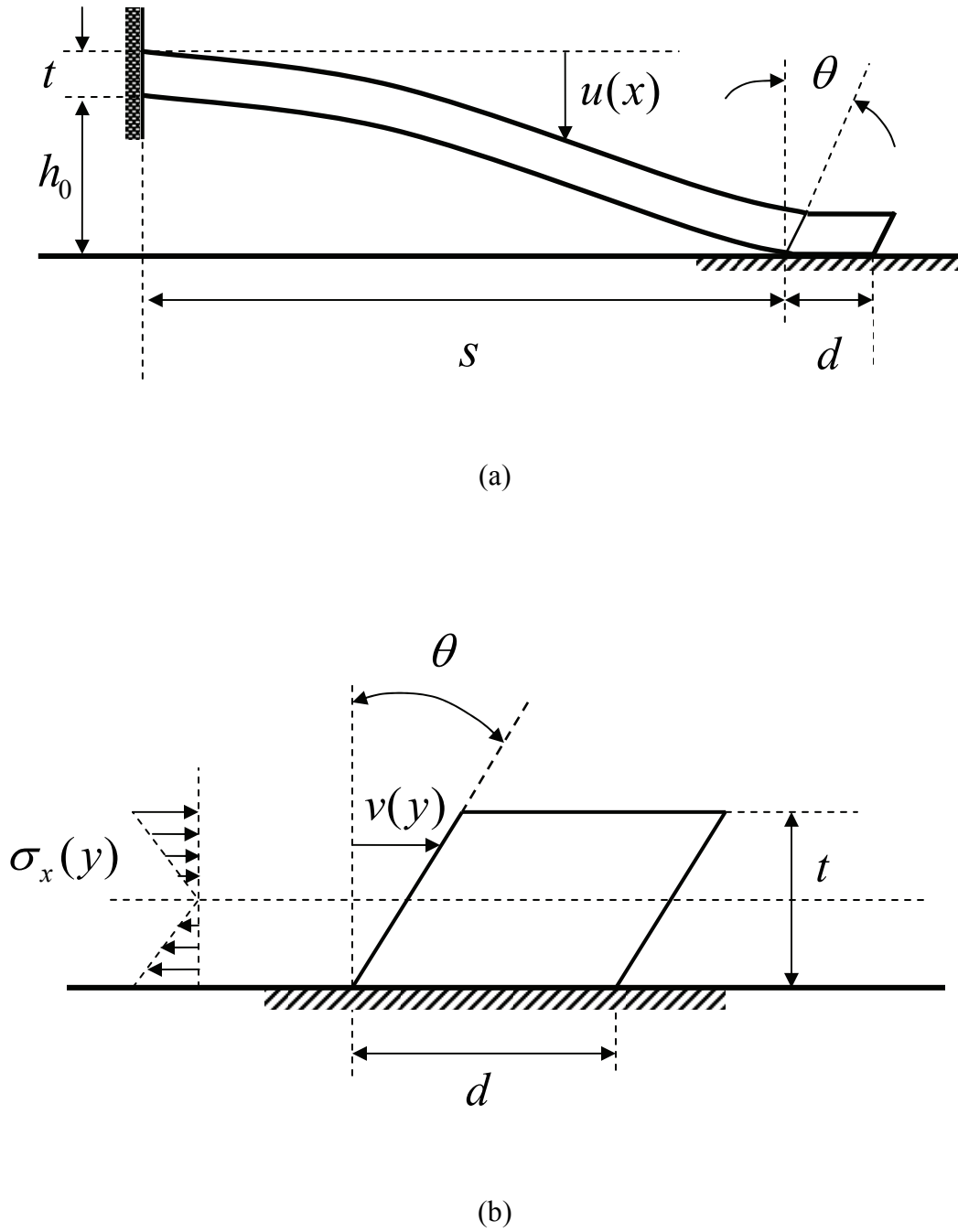
(a)

(b)

Figure 50. Shear deformations at the beam tip

There is no external force acting on the adhesion free region of the beam for $0 \leq x \leq s$, so the equation (77) is solved subject to the boundary condition of equation (78) and the modified slope condition at $x = s$,

$$\left.\frac{du}{dx}\right|_s = \theta = \frac{hm}{s} \tag{80}$$

where θ is the shear angle of the tip as shown in figure 50, and m is a non-dimensional number. The deflection of the beam segment solved subject to the modified slope boundary condition is given as

$$u(x) = -h_0 \frac{x^2}{s^2}\left((3-m)+(m-2)\frac{x}{s}\right) \tag{81}$$

The short segment $s \leq x \leq l$ corresponding to the beam tip experiences shear deformations. The shear of the tip $v(y)$ is induced by the horizontal stress of the beam $\sigma_x(y)$. The differential equation for $v(y)$ is

$$\frac{d^2v}{dy^2} = -\frac{M_z}{EI_t} - \frac{3}{2}\frac{q}{GA}, \quad I_t = \frac{wd^3}{12} \tag{82a-b}$$

where I_t is the moment of inertia of the beam tip, $G = E/2(1+v)$ the shear modulus, and $A = wd$. The moment M_z and load q of figure 50 are

$$M_z(y) = -\int_y^t q(y_0)(y_0 - y)dy_0 \tag{83}$$

$$q(y) = \frac{2q_0}{t}(y - \frac{t}{2}) = \sigma_x(y)w \tag{84}$$

$$q_0 = \frac{M_0 wt}{I} \tag{85}$$

Equation (82) is solved subject to the shear boundary conditions $v(0) = (dv/dy)\big|_0 = 0$.

The solution for the shear angle of the tip θ is

$$\theta \approx \frac{v(t)}{t} = \frac{32}{5} \frac{M_0 t}{Ewd^3} \left[1 + \frac{15}{32} \left(\frac{d}{t} \right)^2 \left(\frac{E}{G} \right) \right] \tag{86}$$

Note that θ is proportional to the moment M_0. The beam deflection of equation (81) is used to find M_0.

$$M_0 = -EI \frac{d^2u}{dx^2}\bigg|_s = \frac{2EIh}{s^2}(3 - 2m), \quad m = \frac{\theta s}{h} \tag{87}$$

Substituting equation (87) into equation (86), the $m(s)$ is found.

$$m = \frac{\frac{16}{5} \left(\frac{t}{d} \right)^3 \left(\frac{t}{s} \right) \left[1 + \frac{15}{32} \left(\frac{d}{t} \right)^2 \left(\frac{E}{G} \right) \right]}{1 + \frac{32}{15} \left(\frac{t}{d} \right)^3 \left(\frac{t}{s} \right) \left[1 + \frac{15}{32} \left(\frac{d}{t} \right)^2 \left(\frac{E}{G} \right) \right]} \tag{88}$$

Note that m is in the range of $0 < m < 3/2$. The equation (81) should be used instead of equation (79).

4.2.2. Minimization of energy and peel number in gas

Elastic bending energy stored in the beam is given by

$$U_E = \frac{EI}{2} \int_0^s \left(\frac{d^2u}{dx^2} \right)^2 dx = \frac{6EIh^2}{s^3} \left(1 - m + \frac{1}{3}m^2 \right) \tag{89}$$

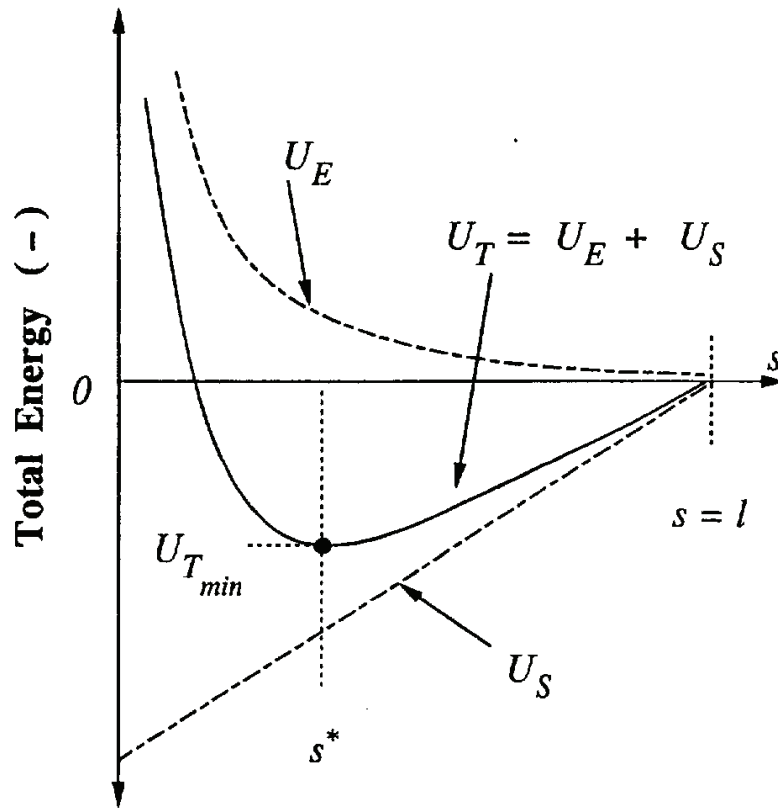Note that U_E decreases with increasing m for $0 \le m \le 3/2$.

Figure 51. Typical energy curves for the beam peeling problem in the air [56]

The interfacial adhesion energy in $s \leq x \leq l$ is the surface energy per unit area of the bond γ_s times the area of contact

$$U_S = -\gamma_s w(l-s) \tag{90}$$

where $\gamma_s = \gamma_1 + \gamma_2 - \gamma_{12}$ is the Dupré adhesion or work of adhesion between the cantilever and the substrate, with γ_1 and γ_2 being the surface energies of the two bodies and γ_{12} the interface energy. The parameter γ_s has units of J/m^2. The sign of U_s is negative

because it is a binding energy. The total energy (or free energy) of the system is the sum of the elastic energy and surface energy.

$$U_T = U_E + U_s \tag{91}$$

Figure 51 shows a typical curve of $U_T(s)$. This curve has minimums corresponding to the equilibrium s^* which is found by setting $dU_T/ds = 0$ and $d^2U_T/ds^2 > 0$.

The maximum cantilever beam length that will not stick to the substrate, or detachment length l_{max}, is defined as

$$l_{max} = s^* = \left(\frac{3}{8} \frac{Et^3h^2}{\gamma_s} \right)^{1/4} \tag{92}$$

To study the stiction of movable MEMS microstructures to the substrate, a dimensionless number, termed peel number, was proposed by Mastrangelo and Hsu [56]. The peel number, N_p, is the ratio of elastic strain energy stored in the deformed microstructure to the work of adhesion between the microstructure and the substrate. If $N_p>1$, the restored elastic strain energy is greater than the work of adhesion, and the microstructure will not stick to the substrate. If, on the other hand, $N_p \leq 1$, the deformed microstructure does not have enough energy to overcome the adhesion between the beam and the substrate. For a long slender cantilever of thickness t, length l and elastic modulus E suspended at a distance h from the substrate, illustrated in figure 52(a), the peel number is

$$N_p = \frac{3Et^3h^2}{2s^4\gamma_s} \tag{93}$$

For a short cantilever beam with just its tip stuck to the substrate, shown in figure 52(b), the corresponding peel number is
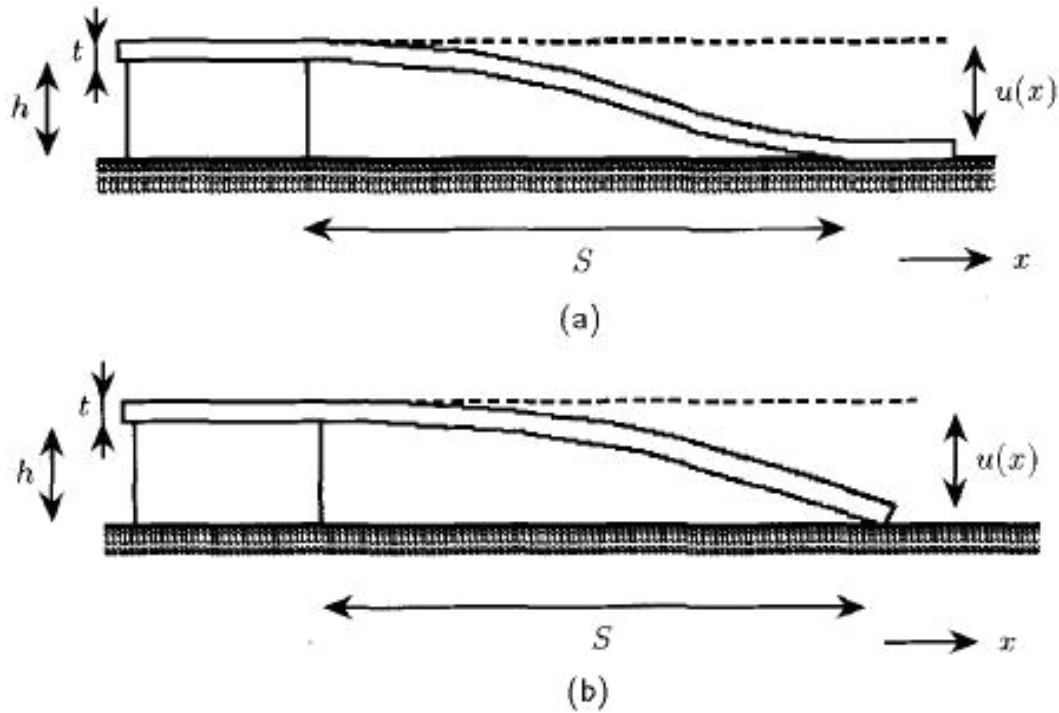
$$N_p = \frac{3Et^3h^2}{8l^4\gamma_s} \tag{94}$$

Figure 52. (a) S-shaped cantilever (b) Arc-shaped cantilever

The elastic contact of the cantilever and substrate with interface roughness is considered by Zhao [52]. The surface roughness is represented by asperities, which are modeled as spherical caps with the same radius of curvature R, and the heights of these asperities obey the Gaussian distribution

$$\varphi(z) = \frac{1}{\sqrt{2\pi}\sigma} \exp\left(-\frac{z^2}{2\sigma^2}\right) \tag{95}$$

where σ is the standard deviation of the distribution of asperity heights. The corresponding peel number for cantilever beam adhesion to a rough surface is

$$\bar{N}_p = \frac{N_p}{f(\theta)} \tag{96}$$

where N_p is the peel number for smooth contact, $\bar{N}_p$ is the peel number considering the rough contact, and $f(\theta)$ is a dimensionless roughness function reflecting the influence of surface roughness on stiction, and θ is the adhesion parameter.

The design parameters are modified accordingly, for example, the maximum cantilever beam length that will not stick to the substrate, or detachment length considering surface roughness, can be modified to

$$l'_{max} = \left(\frac{3Et^3h^2}{8\gamma_s f(\theta)} \right)^{1/4} \tag{97}$$

The difference between l'_{max} and l_{max} is $f(\theta)$. Noticing the fact that the dimensionless roughness function is less than 1, then l'_{max} is always larger than l_{max}.

4.2.3. Modeling of the beam in liquids

The van der Waals force has been ignored in MEMS because it is relatively smaller than other forces such as electrostatic force and inertial force. The electrochemical force has not been considered in stiction problems because there was no notable research about stiction in liquids. But both of the forces are significant in the stiction problem of NEMS in liquids. Since there are electrochemical and van der Waals forces acting on the beam, its deflection $u(x)$ is the solution of

$$EI\frac{d^4u}{dx^4} = f_{EC} + f_{vdW} \tag{98}$$

Here we assume that the initial configuration of the beam is given by the solution to the beam problem when there are no applied forces. This assumption will be validated later. The deflection of the beam $u(x)$ in equation (81) by Mastrangelo and Hsu would be used for the initial deflection of the beam in liquids.

4.2.4. Minimization of energy in liquids

In addition to the elastic bending energy and the interfacial adhesion energy, the van der Waals work done and the electrochemical work done should be considered for the energy equilibrium problem of stiction of NEMS in liquids. As described in the previous section, the main difference between Mastrangelo and Hsu's work and the stiction of NEMS in liquids is the presence of external forces: van der Waals force and electrochemical force.

The van der Waals force per unit length between two parallel plates is given by

$$f_{vdW} = -\frac{A_h w}{6\pi(h_0 + u(x))^3} \tag{99}$$

The van der Waals force in equation (99) goes to infinity when the beam reaches to the substrate, $u(x) \to h_0$. This makes the numerical difficulties to calculate the van der Waals force near the adhered region. We assume that there is one ion size gap, which is denoted as a, between the adhered beam section and the substrate as shown in figure 53.
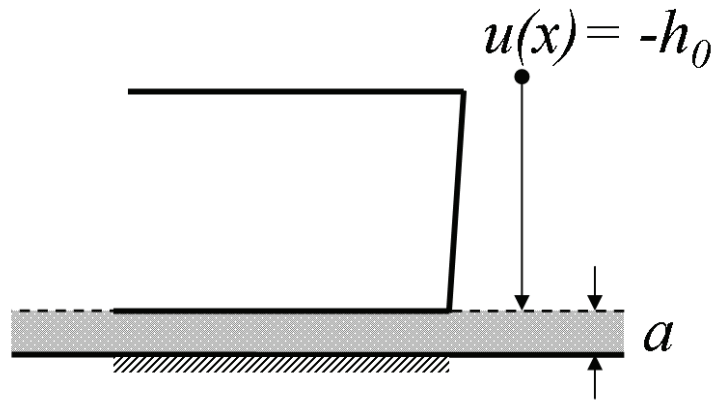
$$u(x) = -h_0$$

$$a$$

Figure 53. Adhered region with one ion size gap distance

Then the van der Waals force is given as

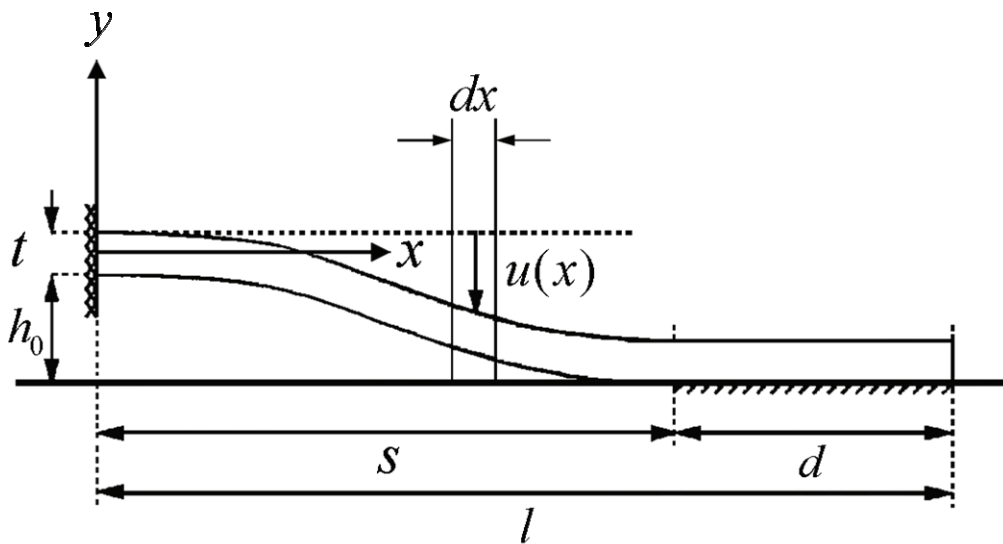$$f_{vdW} = -\frac{A_h w}{6\pi(h_0 + a + u(x))^3}$$

(100)

Figure 54. Beam segment *dx*

Figure 54 shows the finite segment of the beam dx which is assumed to be parallel to the substrate. The van der Waals work done for the beam segment dx is obtained by integrating the van der Waals force from the reference configuration, a straight beam without bending, to the current configuration, a bent beam with displacement $u(x)$.

$$dW_{vdW} = \int_0^{u(x)} f_{vdW} du' = \int_0^{u(x)} -\frac{A_h w}{6\pi(h_0 + a + u')^3} du' = \frac{A_h w}{12\pi}\left[\frac{1}{(h_0 + a + u(x))^2} - \frac{1}{(h_0 + a)^2}\right] \quad (101)$$

The van der Waals work done throughout the adhered beam section $s \leq x \leq l$ is already considered in the surface adhesion energy. So the van der Waals work done for the beam is obtained by integrating dW_{vdW} throughout the opened beam section $0 \leq x \leq s$.

$$W_{vdW} = \int_0^s dW_{vdW} dx \quad (102)$$

It should be noted that the van der Waals work done is a function of s.

As describe in section 3, the electrochemical force between two plates in liquids is significant in NEMS in liquids, but can not be solved as a closed form if MPB equation is not linearized because of the high nonlinearity. But the linearized equation is limited to low applied potential cases only. We use numerical methods to solve the nonlinear MPB equation. The process to obtain the electrochemical energy of a system by numerical methods will be explained with an example process in given particular parameters.
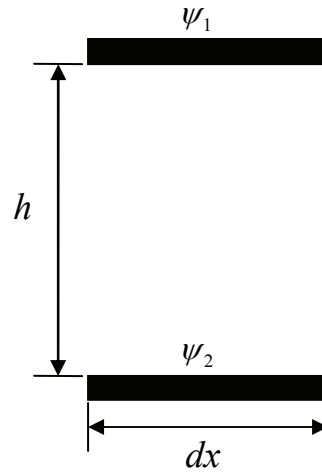
Figure 55. Segment dx of the two parallel plates

Figure 55 shows the beam and substrate in the segment dx in figure 54. The cantilever beam in the segment is assumed to be parallel to the substrate.

First, an 1D nonlinear MPB equation between the segments of two parallel plates (figure 54) in a given gap distance is solved numerically using COMSOL, a commercially available FEM software. The ion size a = 0.3nm is used for the MPB calculation. Then, the electric potential results obtained from the numerical calculation are substituted to the total pressure equation (34) in section 2.

Second, the first process is repeated with various gap distances. Figure 56 shows the electrochemical pressure distribution according to various gap distances when $\psi_1 = \psi_2 = 100\text{mV}$ and $c_b = 0.1\text{M}$.
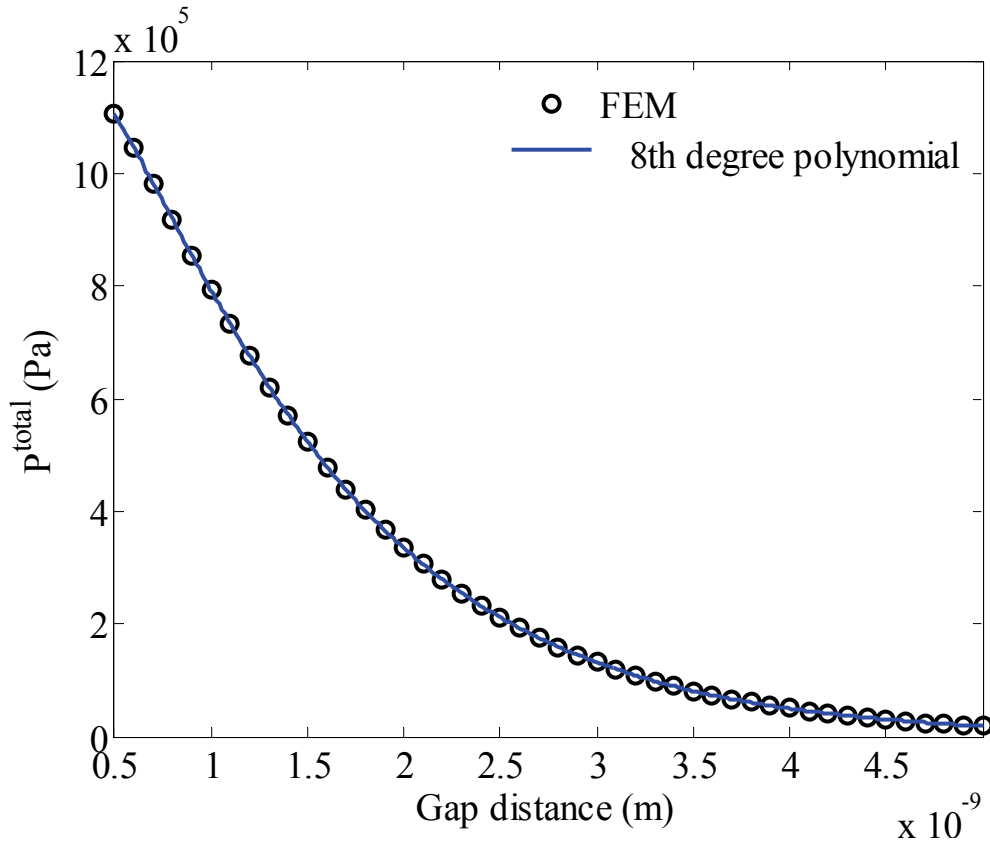
Figure 56. Electrochemical force distribution versus gap distance

By curve fitting, the electrochemical force is described as a polynomial equation form as a function of gap distance h.

$$P^{total} = C_1 h^8 + C_2 h^7 + C_3 h^6 + C_4 h^5 + C_5 h^4 + C_6 h^3 + C_7 h^2 + C_8 h + C_9 = \frac{f_{EC}}{w} \tag{103}$$

where the C_i is the polynomial constant. The electrochemical work done for the beam segment dx is obtained by integrating the electrochemical pressure curve from h to h_0 as shown in figure 45 and equation (104). It should be noted that the electrochemical work done is negative of the colored area in figure 57.
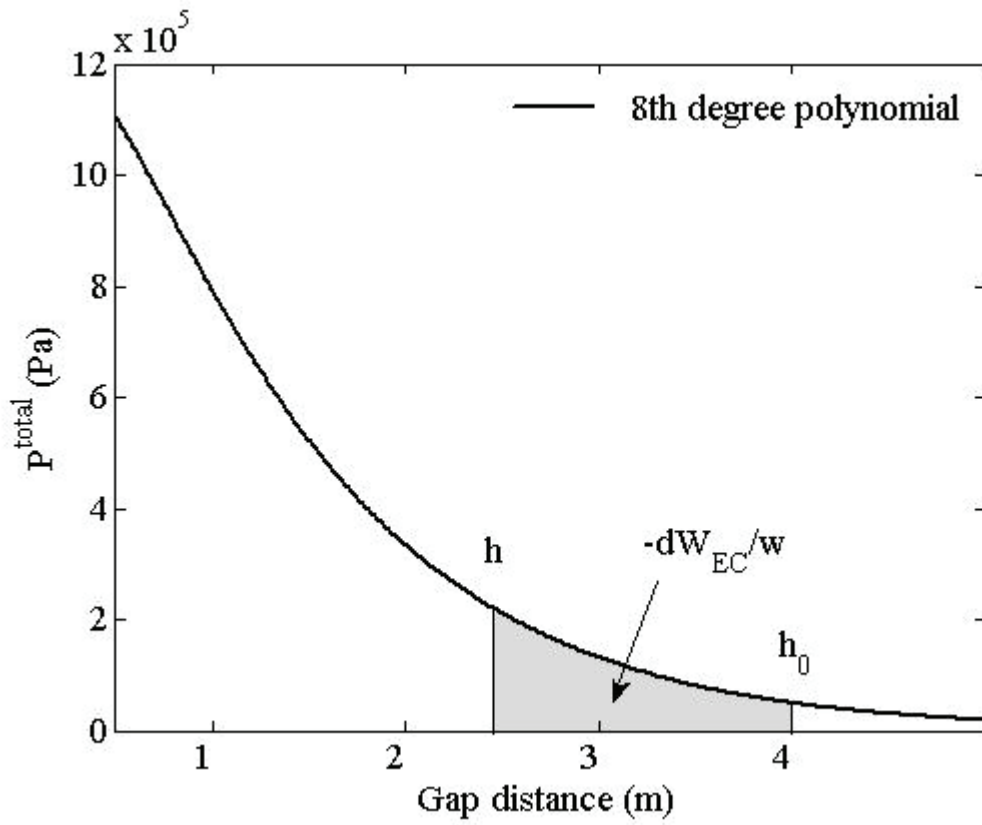
Figure 57. Electrochemical work done for the segment *dx*

$$dW_{EC} = \int_{h_0}^{h} f_{EC} dh = \int_{h_0}^{h_0+u(x)} f_{EC} dh \qquad (104)$$

The electrochemical work done for the entire beam is obtained by integrating dW_{EC} throughout the entire beam.

$$W_{EC} = \int_0^l dW_{EC} dx \qquad (105)$$

The total energy (or free energy) of the system is the sum of the elastic energy, the surface energy, the van der Waals work done and the electrochemical work done.

$$U_T = U_E + U_S - W_{EC} - W_{vdW} \tag{106}$$

System equilibrium values of s are determined by setting

$$\frac{dU_T}{ds} = 0 \, , \; \frac{d^2 U_T}{ds^2} > 0 \tag{107}$$

To characterize the system equilibrium, we determine the minimum value of U_T for various value of s assuming a fixed value of γ_s. A straightforward method to solve equation (107) is by the graphical method.

We plot U_T versus s assuming a polymer nano cantilever beam which has the material and geometrical constant as shown in table 5. The surface energy of common polymers is between 20 to 50mJ/m^2. However, the surface energy can be reduced by various surface treatments down to 0.012mJ/m^2 [57]. In this research, the surface energy is assumed to be 5mJ/m^2.

Table 5. Material and geometrical constant

E (Young's modulus)	153GPa	h_0 (initial gap distance)	4nm
t (Beam thickness)	4nm	L (Beam length)	120nm
w (Beam width)	2nm	γ_s (Surface energy)	5mJ/m^2

The elastic energy decreases exponentially as *s* increases as shown in figure 58. It should be noted that the reference state for the energy calculation is the straight beam which has no bending at all.
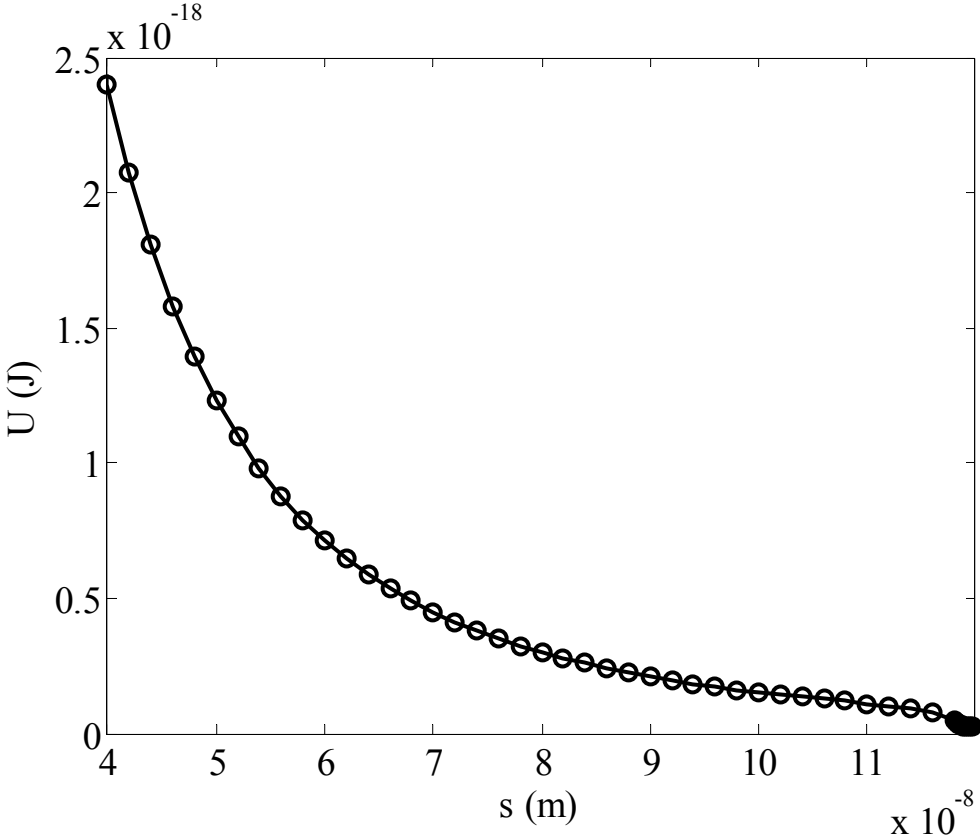
Figure 58. Elastic energy versus *s*

The elastic energy is only a function of h_0 and *s*. The elastic energy is the energy stored in the beam. If the beam is free from the stiction, the beam tries to go to the lowest energy state, the reference configuration which has no bending.
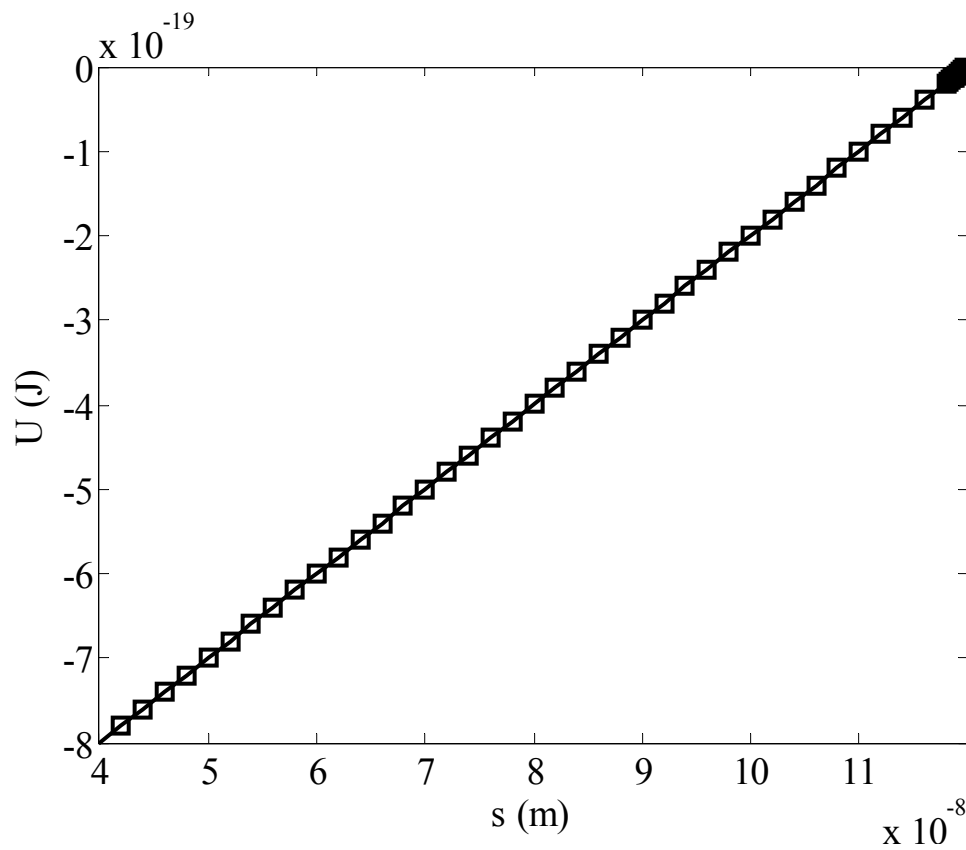
Figure 59. Surface energy versus *s*

The absolute value of the surface energy decreases linearly as *s* increases as shown in figure 59. The surface energy is a function of the attached distance $d = l - s$. The surface adhesion energy is the energy which is holding the beam to the substrate overcoming the elastic energy.
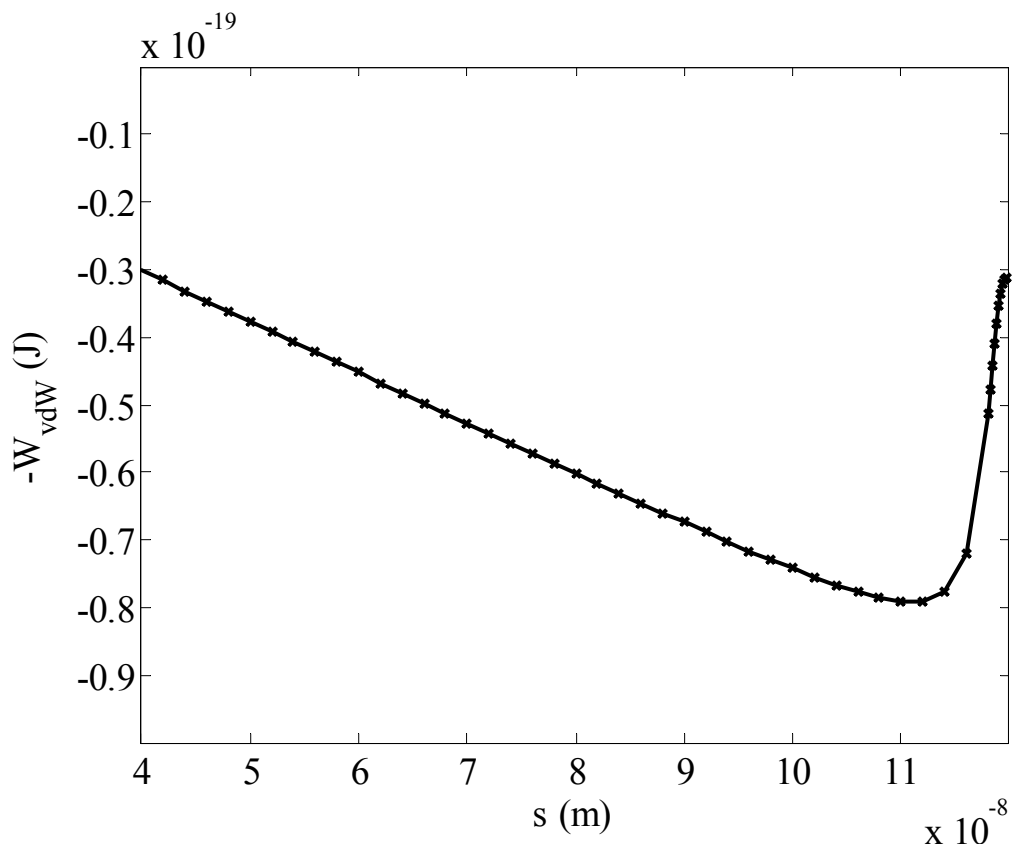
Figure 60. van der Waals work done versus *s*

The absolute value of van der Waals work done increases as s increases until the beam has s-shape as shown in figure 60. When the beam turns over to the arch-shape, the van der Waals work done dramatically decreases because the area where the distance between the beam and the substrate are significant is decreased. The van der Waals work done is a function of h_0 and *s*.
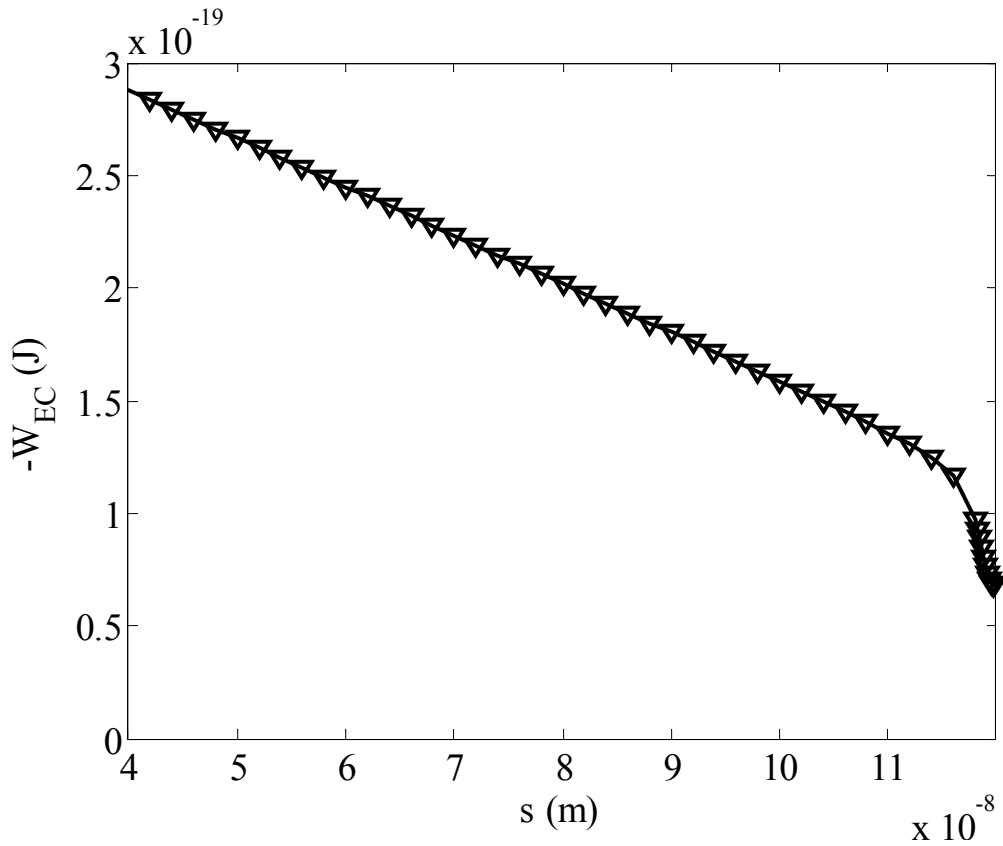
Figure 61. Electrochemical work done versus *s*

Figure 61 shows the electrochemical work done distribution versus *s*. The electrochemical work done decreases as *s* increases. In a given h_0, the electrochemical work done is a function of c_b and Ψ. The electrochemical work done curve shows linear distribution during the beam has s-shaped configuration and rapidly decrease in arc-shaped region. In section 4.3, parametric studies will be performed to find out the roles of electrochemical work done to the total energy curves and equilibrium positions.
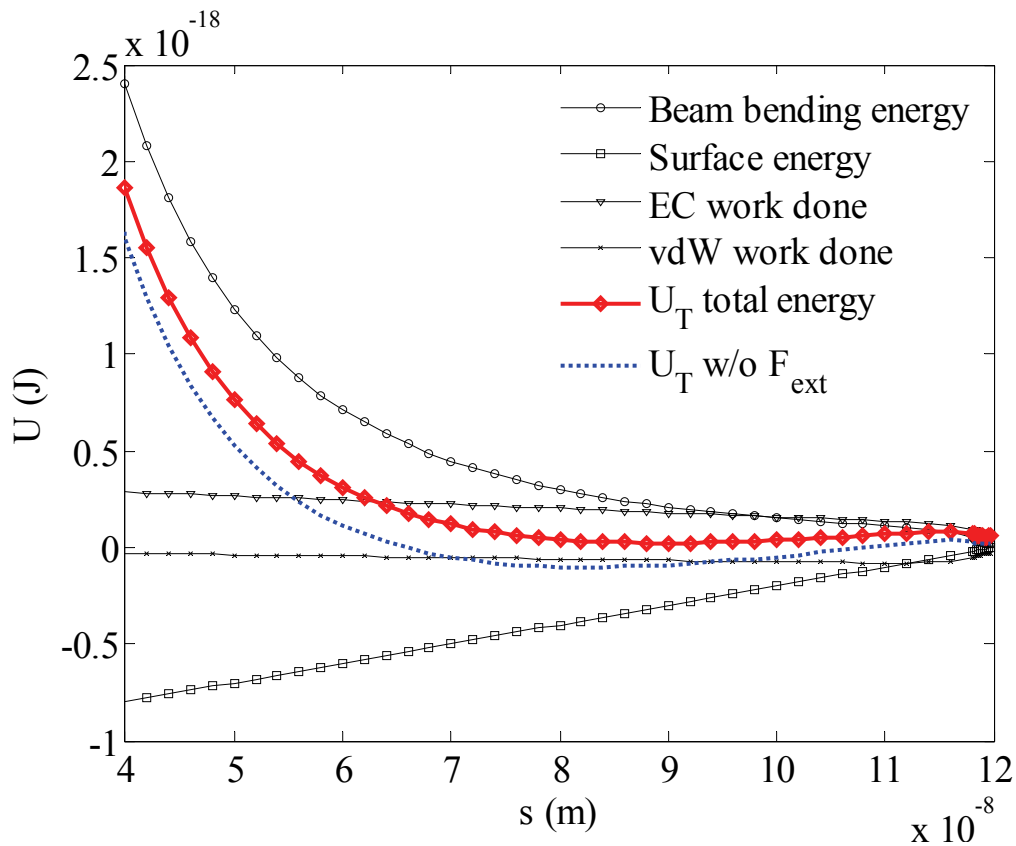
Figure 62. Energy curves versus *s*

Figure 62 shows each of the energies and the total energy distributions versus *s*. The dotted curve is the energy distribution without considering the van der Waals and electrochemical work done, and the diamond marked curve is the energy distribution considering all energies involved to the system. It is observed that the equilibrium position of the diamond marked curve is in right hand side of the equilibrium position of the dotted curve, but still exists in the middle of the beam length region. It means that the beam remains adhered to the substrate when the ion concentration is 0.1M and the applied potential is 50mV. In section 4.3.1, parametric studies will be performed to see

how the equilibrium position changes and if the stiction is released with various values of ion concentrations and applied potentials.
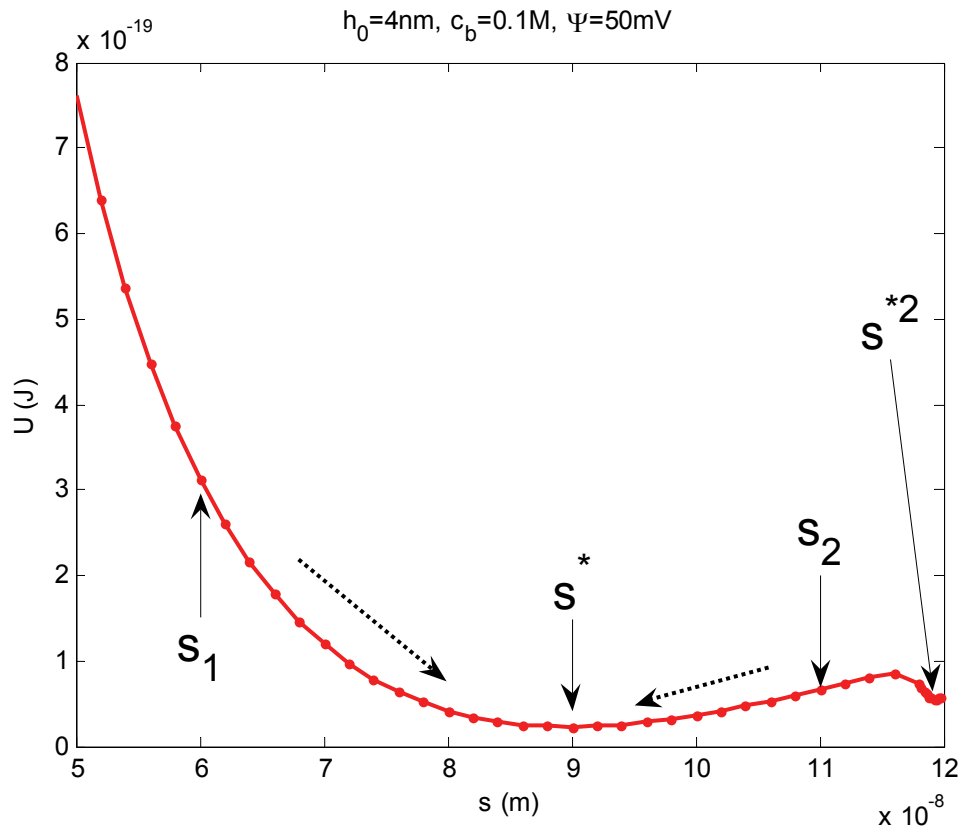
Figure 63. Total energy curve versus s

Figure 63 shows the total energy curve enlarged in the equilibrium position region. The equivalent beam shapes for four different s values are shown in figure 64. If the beam was in the state where s is s_1 or s_2, the beam is unstable and moves to the equilibrium energy state, where s is s^*, and stay adhered to the substrate having s-shaped configuration. To release the beam from the substrate, the total energy curve

should not have energy well and equilibrium position in the middle of the beam length. The energy curve shows another equilibrium position s^{*2} which is located in the beam tip and has very narrow well. The beam is also stable and has arc-shaped configuration as shown in figure 64.
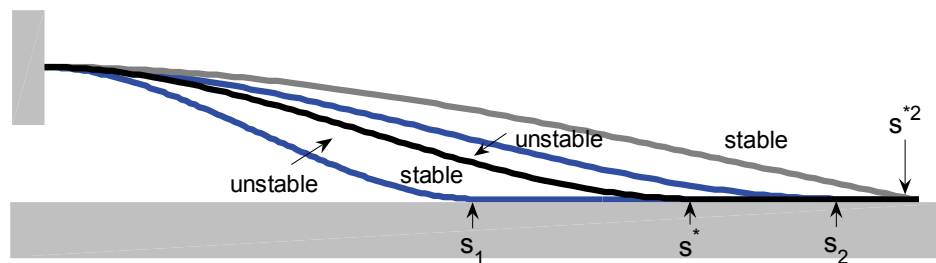
Figure 64. Equilibrium position of the cantilever beam

4.3. Result

4.3.1. Deflection of the adhered beam

As mentioned in section 4.2.3, the initial cantilever beam configuration adhered to the substrate in liquid electrolyte is assumed to be the same as the initial cantilever beam configuration without external forces. This assumption will be validated in this section.

The cantilever beam used in section 4.2.4 (see table 5) is used in this section again. The cantilever beam deflection due to the external forces is calculated with

various parameters when the beam is adhered to the substrate with *s*=43nm. Figures 65
and 66 show the beam deflection with three different applied potentials when the ion
concentrations are 0.1M and 1M, respectively. The maximum deflection of the beam
increases as the ion concentration and the applied potentials increase. When the ion
concentration is 1M and the applied potential is 100mV, the maximum deflection of the
beam is 0.27nm as shown in figure 66, which is very small relative to the beam
dimensions and the initial gap between the beam and the substrate. Therefore, the initial
configuration of the beam without external forces can be used as the initial configuration
of the beam in the liquid electrolyte.
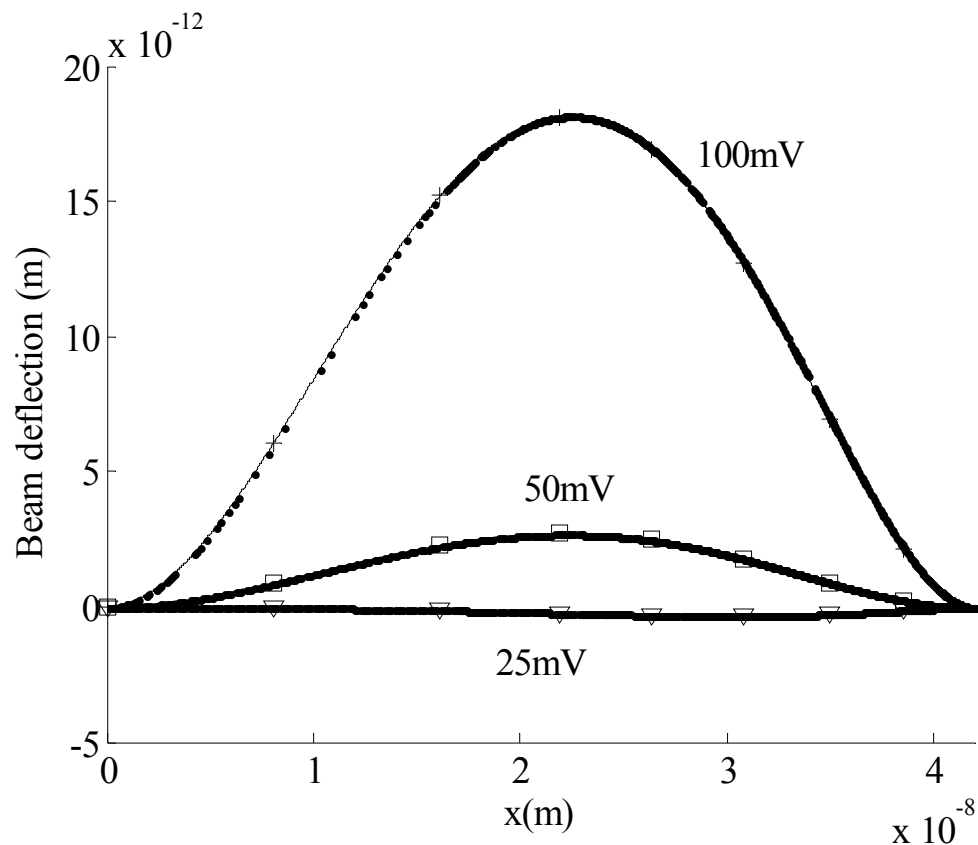
Figure 65. Beam deflection when $c_b = 0.1$ M
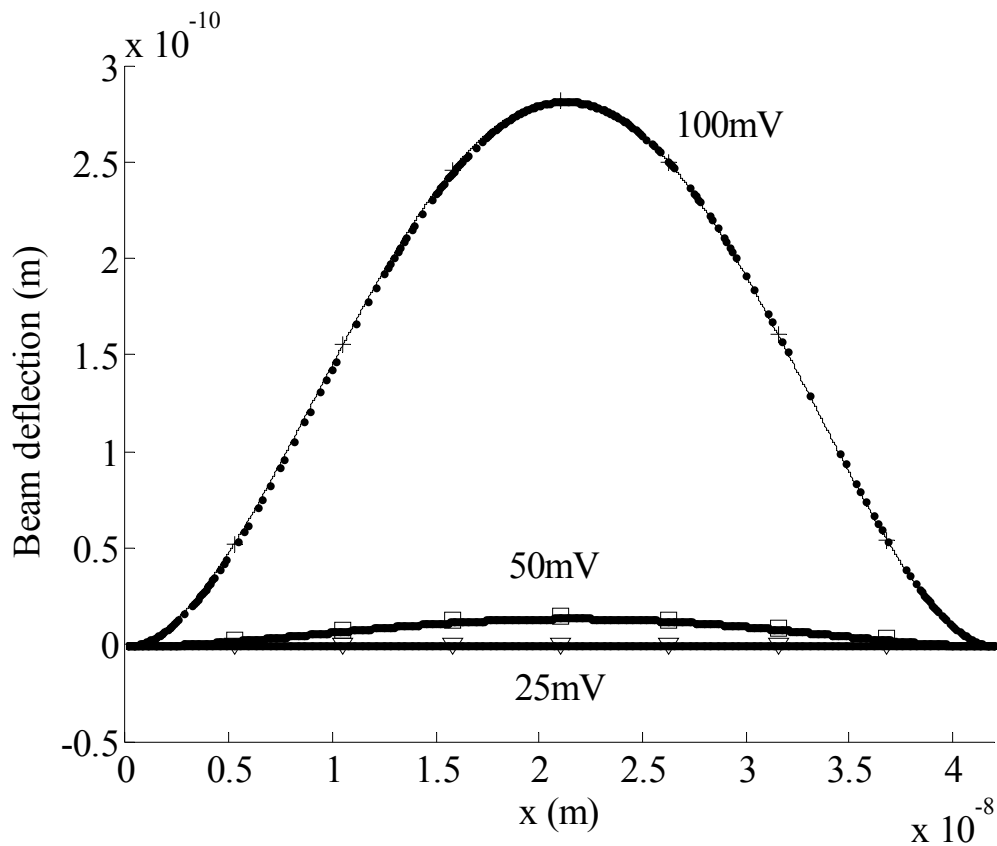
Figure 66. Beam deflection when $c_b = 1$ M

4.3.2. Effects of h_0, c_b, and Ψ on stiction

Parametric studies are performed with various values of the ion concentration and applied electric potential. Table 6 shows material and geometrical constants for the parametric studies. The aspect ratio of the beam thickness and length is 30 for the cantilever beam has s-shaped initial configuration. The beam is assumed to be made of silicon with a polymer coating.

Table 6. Material and geometrical constants for parametric studies

Constants	Values
E (Young's modulus)	153GPa
t (Beam thickness)	4nm
w (Beam width)	2nm
L (Beam length)	120nm
γ_s (Surface energy)	5mJ/m^2

Figures 67-78 show each energies and total energy distributions versus s when h_0 is 3nm. The parametric studies are performed for three different ion concentrations, 0.01M, 0.1M, 1M and for four different applied potentials, 25mV, 50mV, 75mV and 100mV.
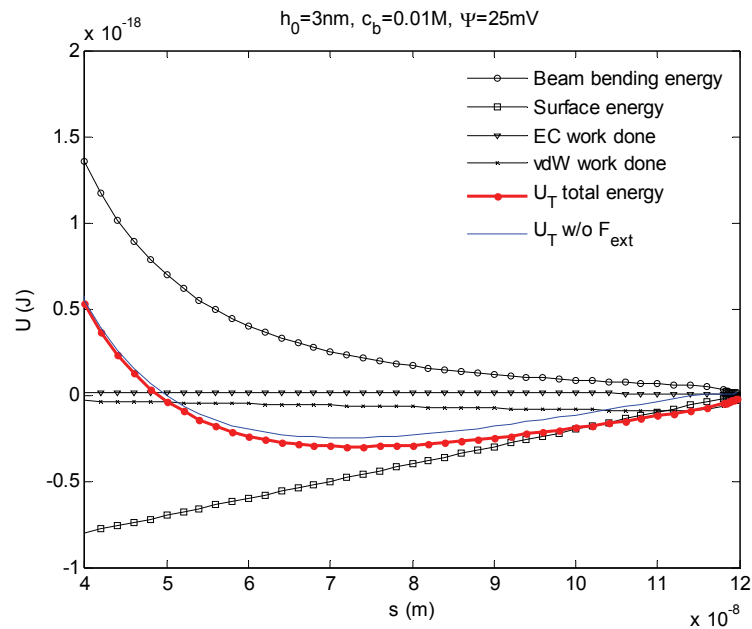
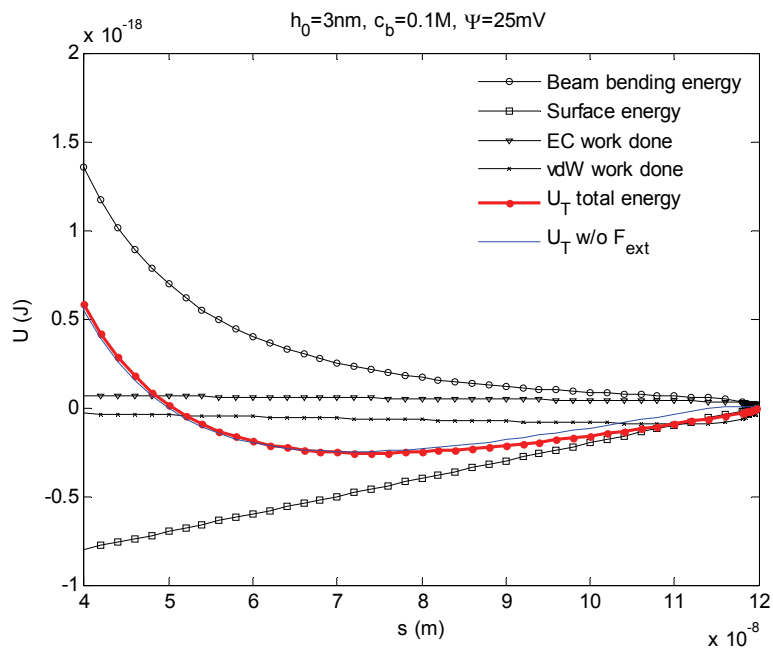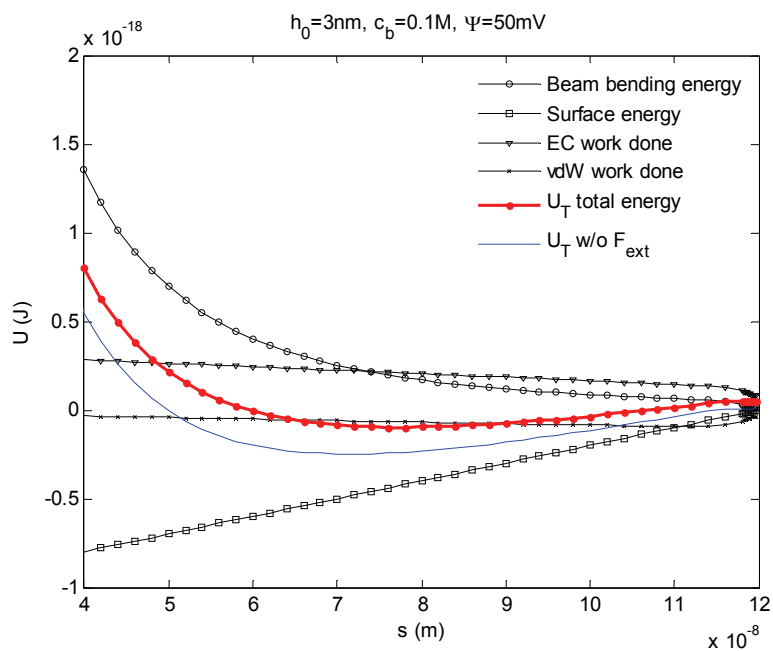Figure 67. Energy curves when $h_0 = 3\,\text{nm}, c_b = 0.01\,\text{M}, \Psi = 25\,\text{mV}$
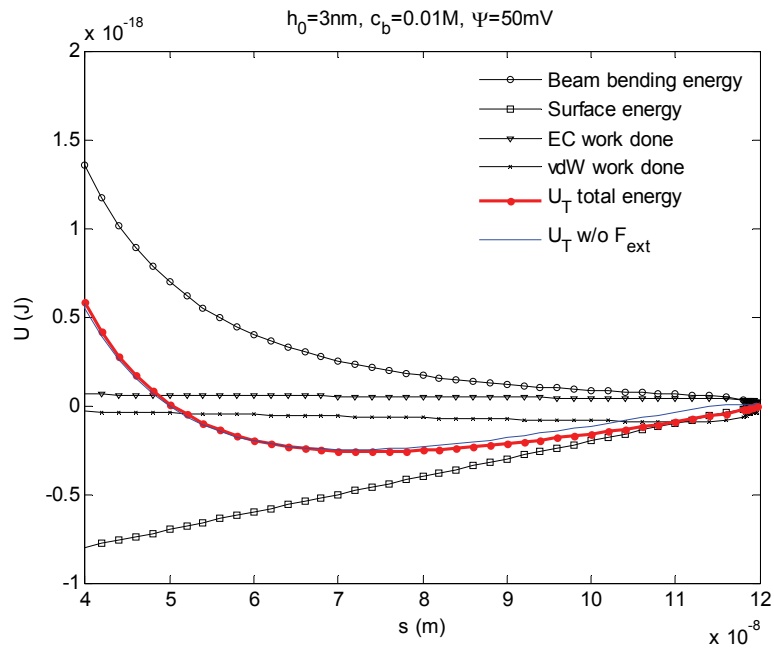
Figure 68. Energy curves when $h_0 = 3\,\text{nm}, c_b = 0.01\,\text{M}, \Psi = 50\,\text{mV}$
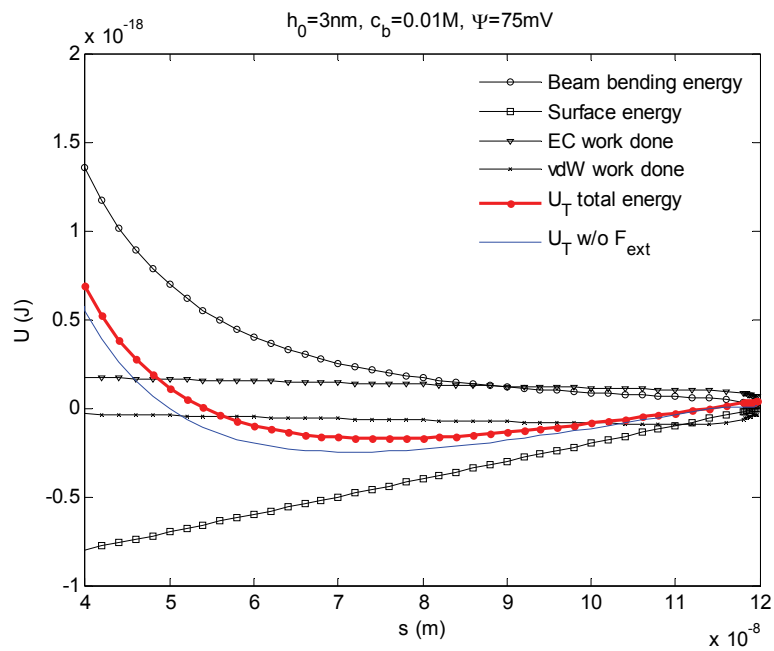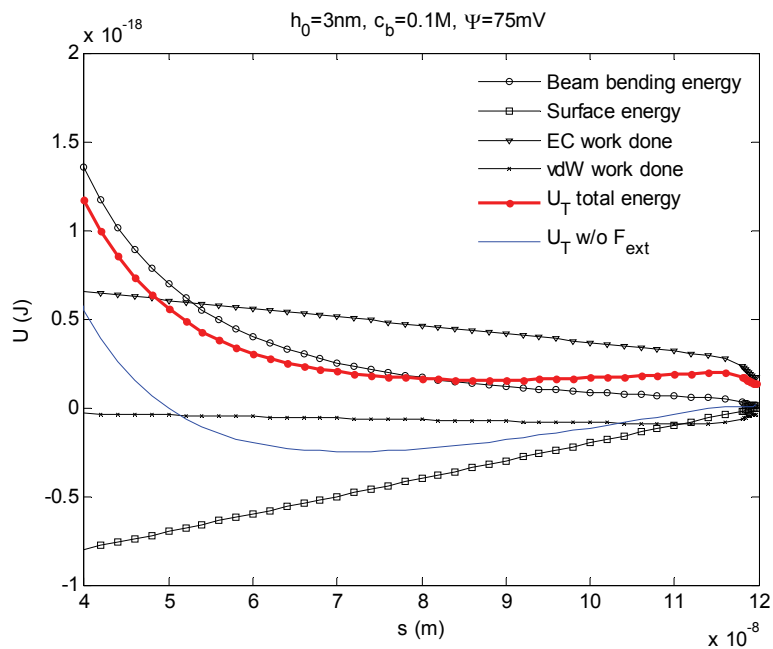

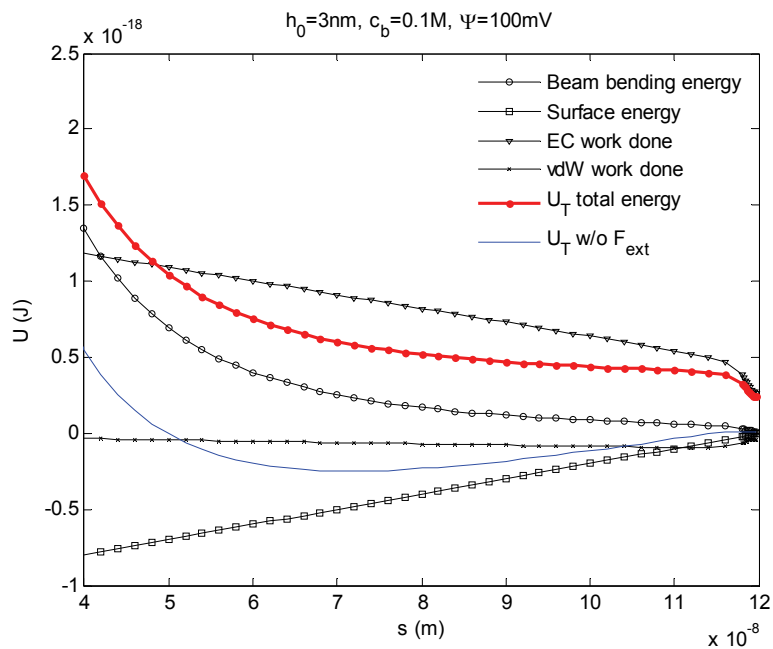Figure 69. Energy curves when $h_0 = 3\,\text{nm}, c_b = 0.01\,\text{M}, \Psi = 75\,\text{mV}$
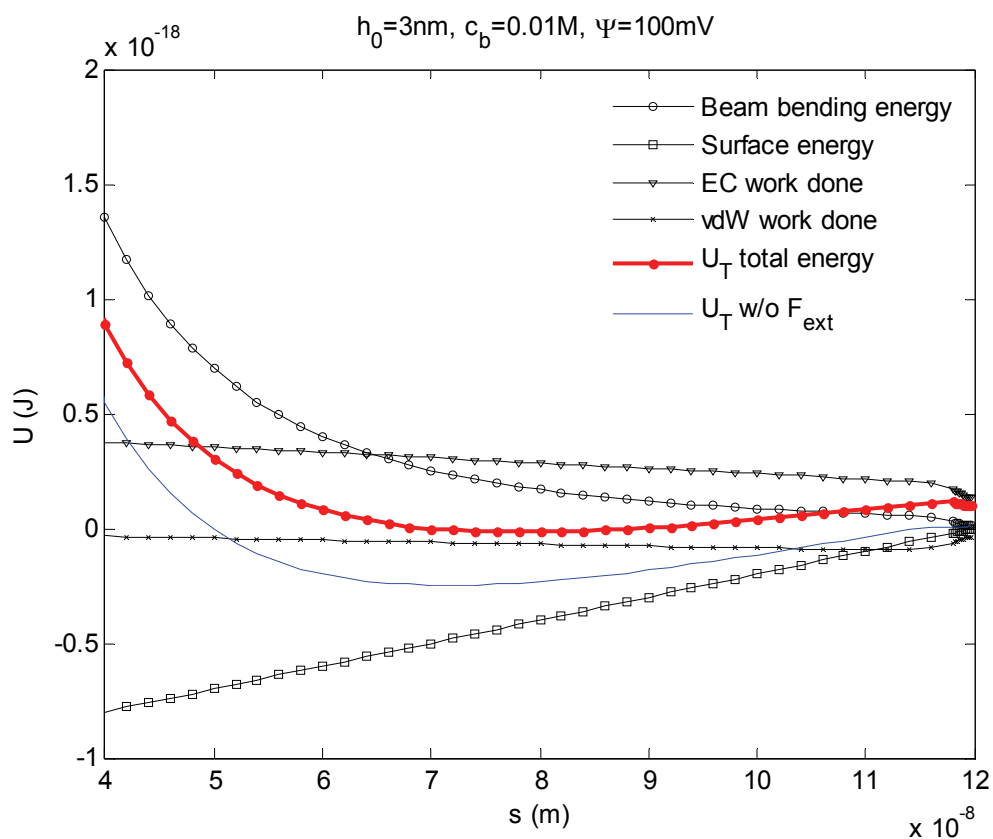
Figure 70. Energy curves when $h_0 = 3\,\text{nm}, c_b = 0.01\,\text{M}, \Psi = 100\,\text{mV}$

All total energy curves of the system which has 3 nm height and 0.01M ion concentration had equilibrium positions for every applied potential values. It means in low ion concentration the electrochemical work done is not large enough to remove the equilibrium positions. This beam would stay adhered to the substrate even the equilibrium position slightly moved to the right hand side by increasing the applied potentials.

Figure 71. Energy curves when $h_0 = 3\,\text{nm}, c_b = 0.1\,\text{M}, \Psi = 25\,\text{mV}$

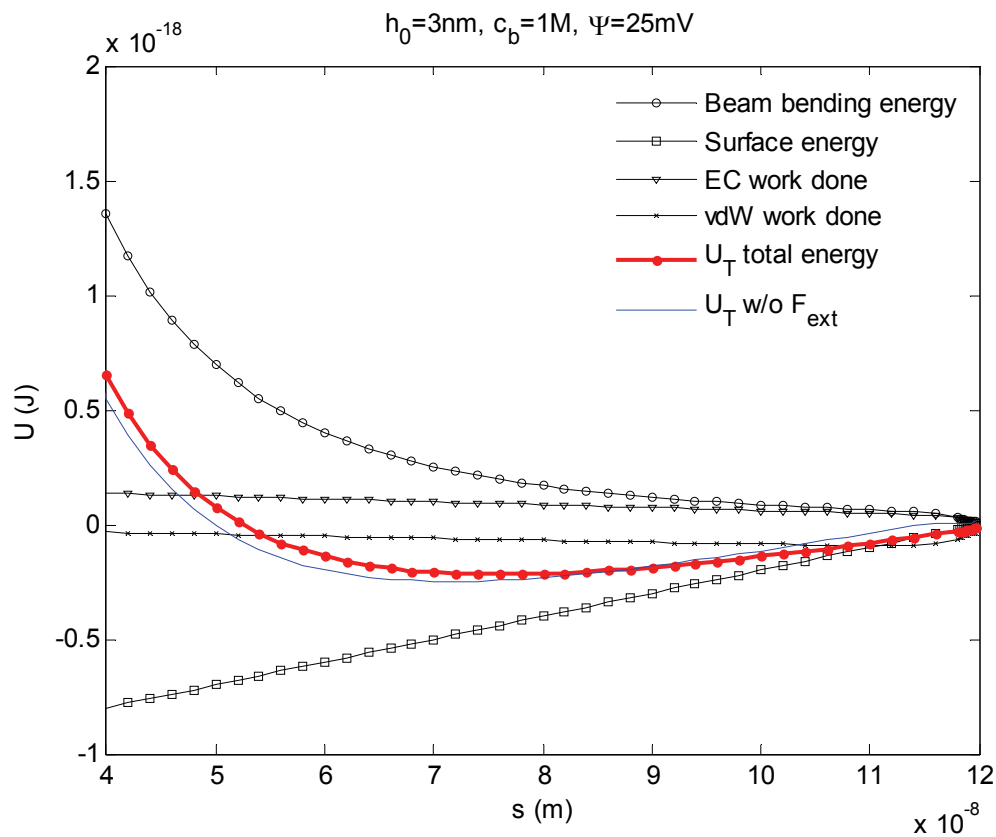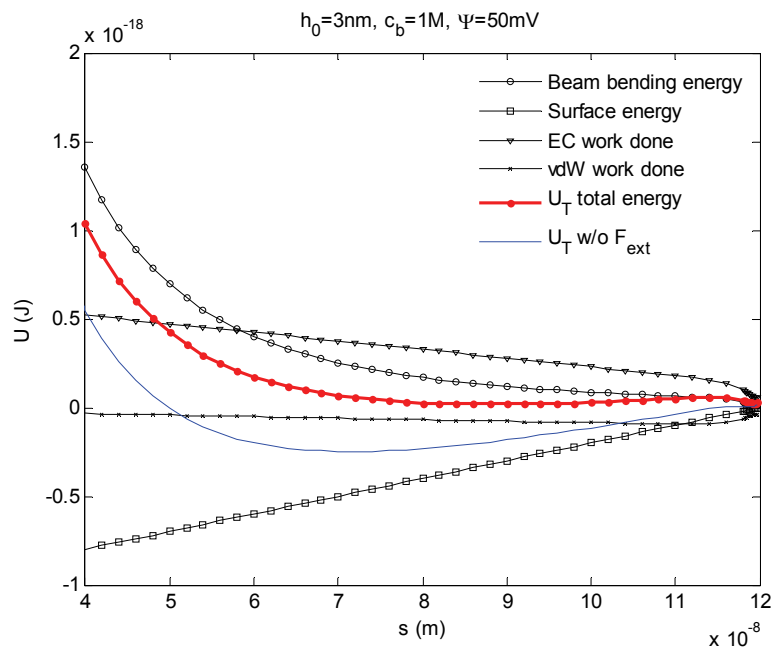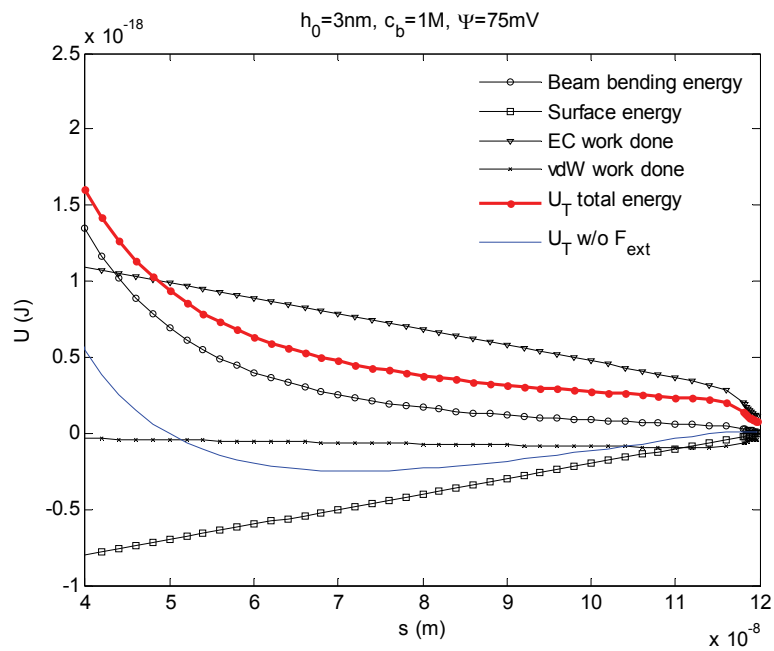Figure 72. Energy curves when $h_0 = 3\,\text{nm}, c_b = 0.1\,\text{M}, \Psi = 50\,\text{mV}$

Figure 73. Energy curves when $h_0 = 3\,\text{nm}, c_b = 0.1\,\text{M}, \Psi = 75\,\text{mV}$
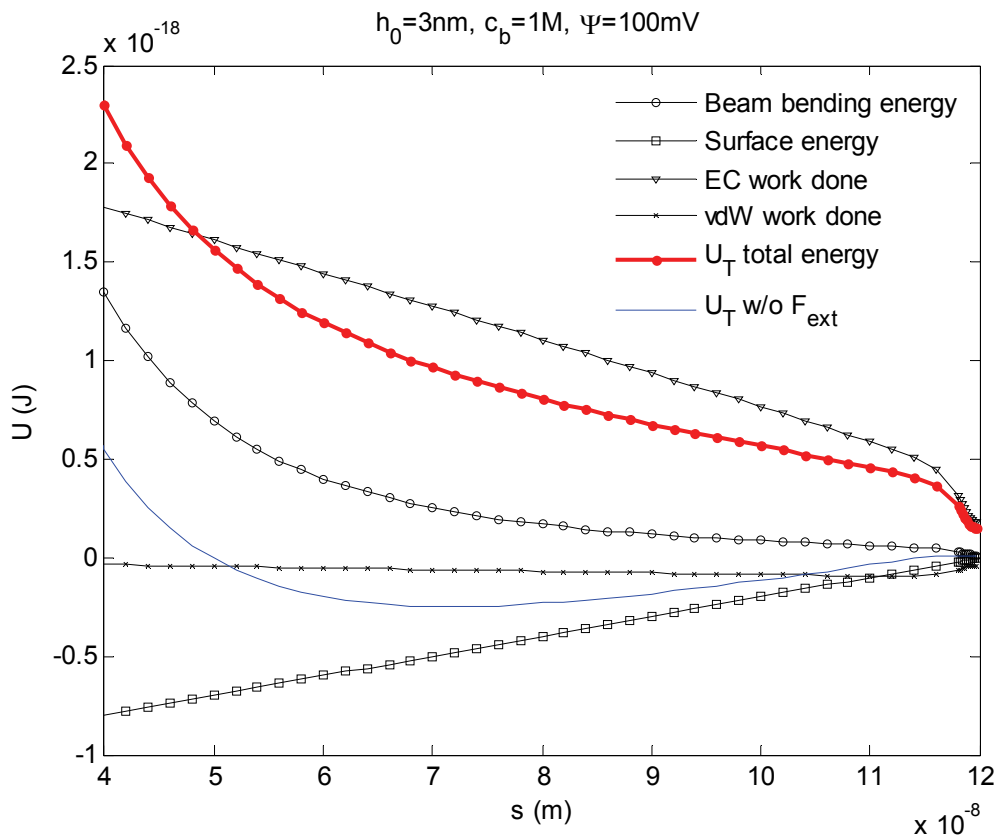

Figure 74. Energy curves when $h_0 = 3\,\text{nm}, c_b = 0.1\,\text{M}, \Psi = 100\,\text{mV}$

The equilibrium position of the total energy curves of the system which has 3nm height and 0.1M ion concentration keep moved to the right hand side and was removed when the applied potential was 100mV. Figure 74 shows that the total energy curve does not have a energy well in between the beam length. The stiction of this beam could be released with 100mV applied potential.

Figure 75. Energy curves when $h_0 = 3\,\text{nm}, c_b = 1\,\text{M}, \Psi = 25\,\text{mV}$

Figure 76. Energy curves when $h_0 = 3\,\text{nm}, c_b = 1\,\text{M}, \Psi = 50\,\text{mV}$

Figure 77. Energy curves when $h_0 = 3\,\text{nm}, c_b = 1\,\text{M}, \Psi = 75\,\text{mV}$

Figure 78. Energy curves when $h_0 = 3\,\text{nm}, c_b = 1\,\text{M}, \Psi = 100\,\text{mV}$

The equilibrium position of the total energy curves of the system which has 3nm height and 1M ion concentration keep moved to the right hand side and was removed when the applied potential was larger than 75mV. The stiction of this beam could be released with applied potentials larger than 75mV. It means that the stiction can be released by relatively low applied potential in high ion concentration.

Figures 79-90 show each energies and total energy distributions versus s when h_0 is 4nm.
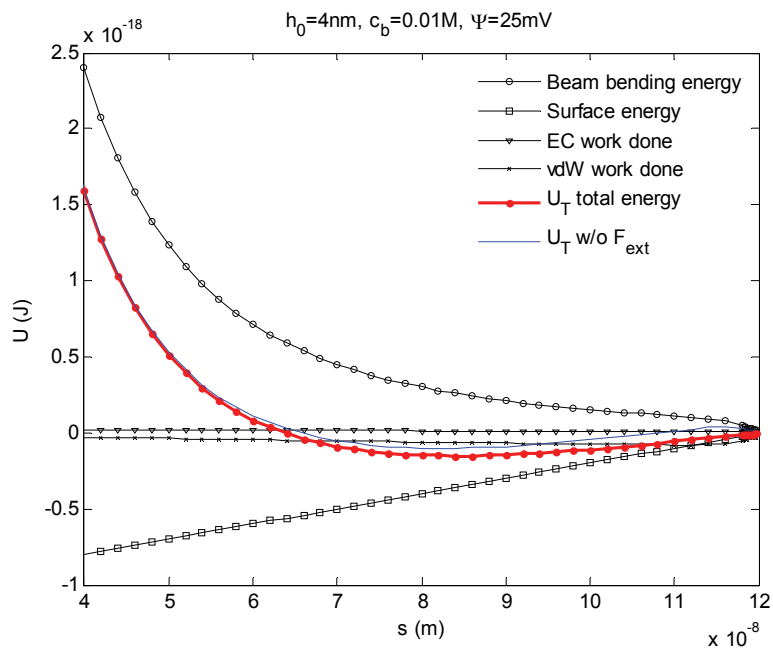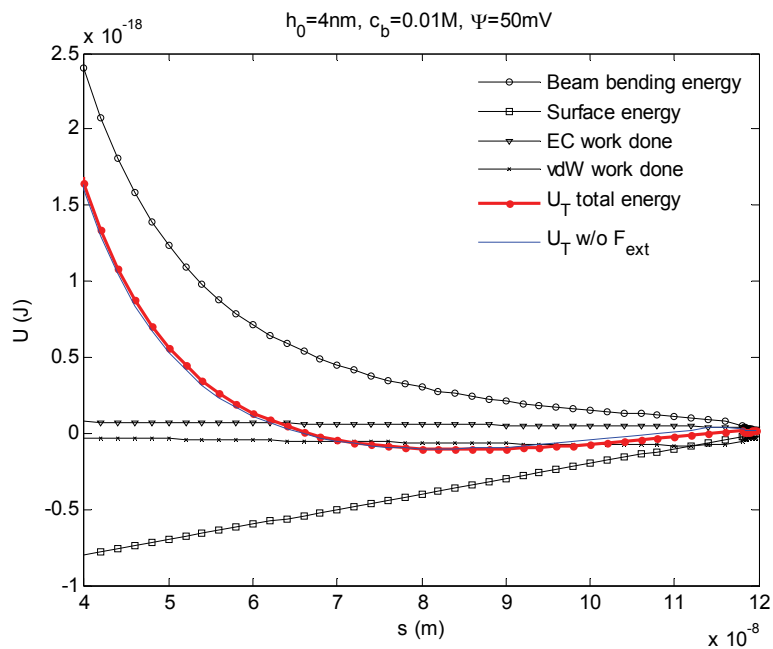
Figure 79. Energy curves when $h_0 = 4\,\mathrm{nm}, c_b = 0.01\,\mathrm{M}, \Psi = 25\,\mathrm{mV}$

Figure 80. Energy curves when $h_0 = 4\,\mathrm{nm}, c_b = 0.01\,\mathrm{M}, \Psi = 50\,\mathrm{mV}$
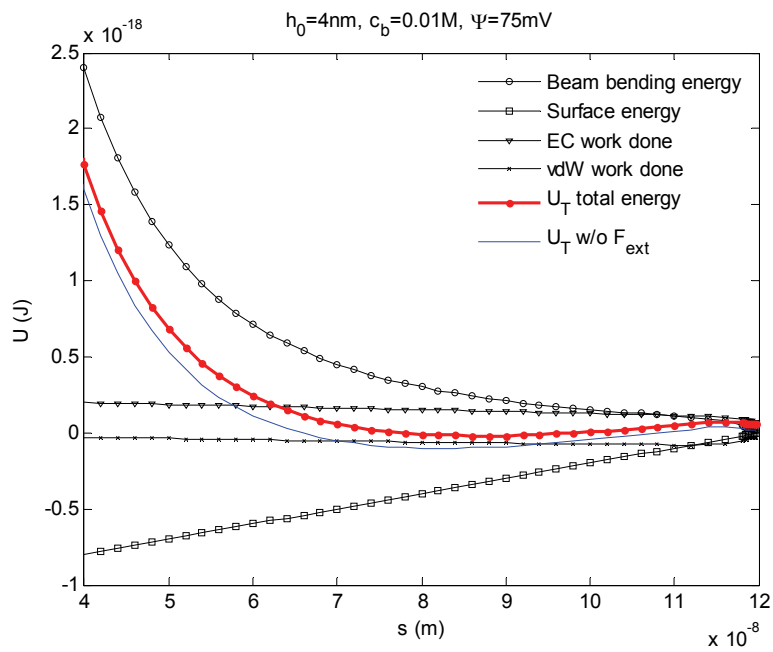
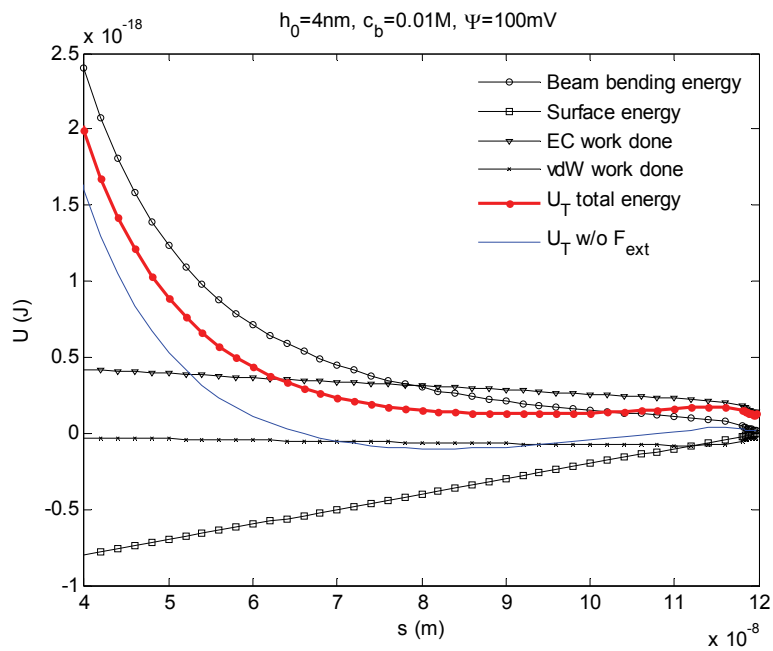Figure 81. Energy curves when $h_0 = 4\,\text{nm}, c_b = 0.01\,\text{M}, \Psi = 75\,\text{mV}$

Figure 82. Energy curves when $h_0 = 4\,\text{nm}, c_b = 0.01\,\text{M}, \Psi = 100\,\text{mV}$

All total energy curves of the system which has 4nm height and 0.01M ion concentration had equilibrium positions for every applied potential values. The elastic energies for 4nm height were bigger than those for 3nm height because more energies were needed to bend down the beam with longer height. The surface adhesion energy curves showed the same values with those of 3nm height system because the surface adhesion energy is not a function of height but only a function of s. In low ion concentration of 0.01M, the electrochemical work done is not large enough to remove the equilibrium positions. This beam would stay adhered to the substrate even the equilibrium position slightly moved to the right hand side by increasing the applied potentials.
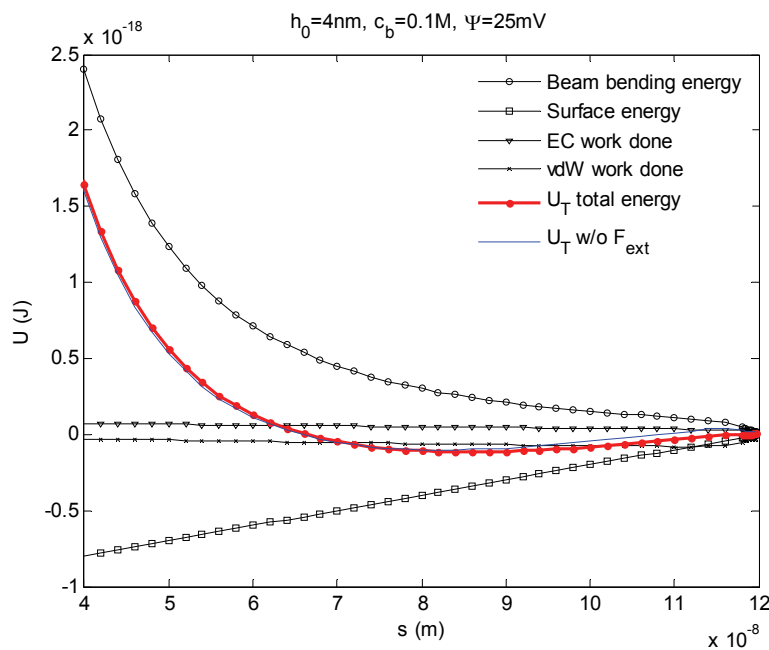

Figure 83. Energy curves when $h_0 = 4\,\mathrm{nm}, c_b = 0.1\,\mathrm{M}, \Psi = 25\,\mathrm{mV}$
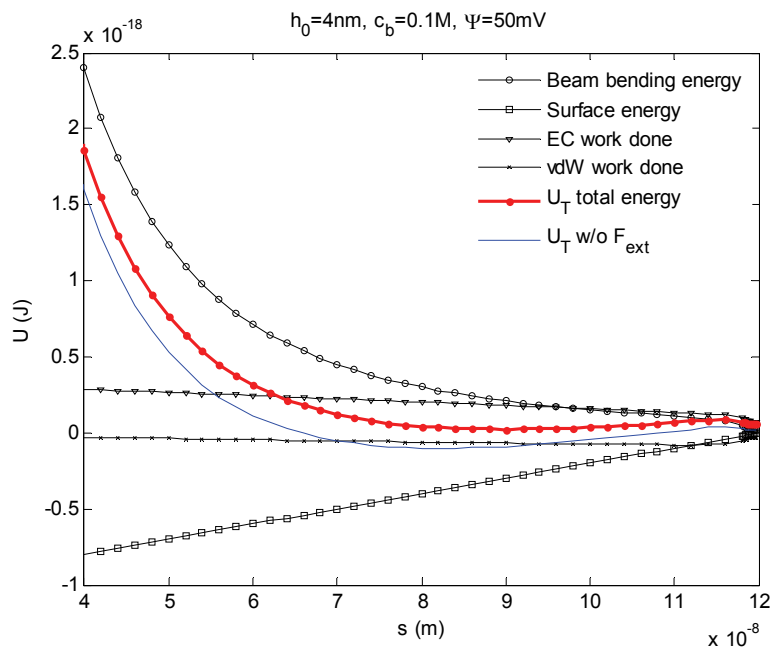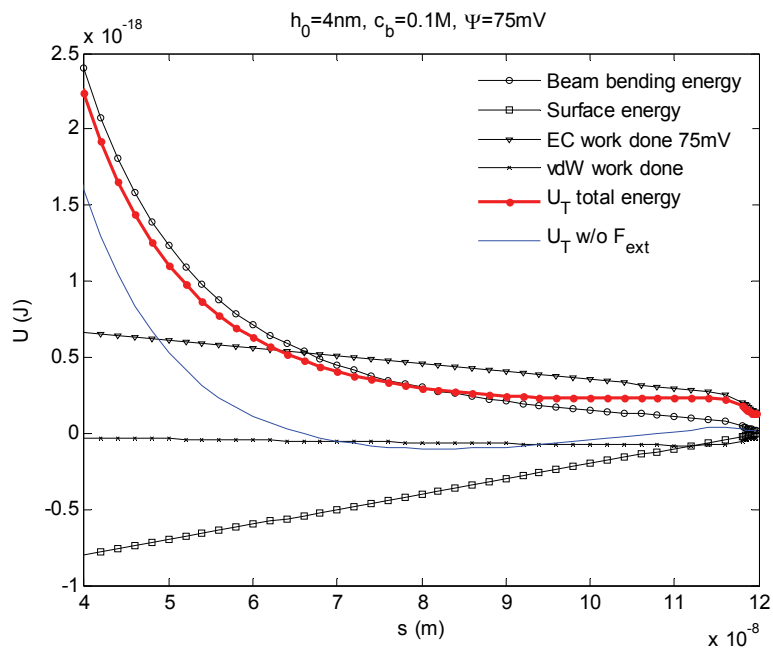
Figure 84. Energy curves when $h_0 = 4\,\text{nm}, c_b = 0.1\,\text{M}, \Psi = 50\,\text{mV}$

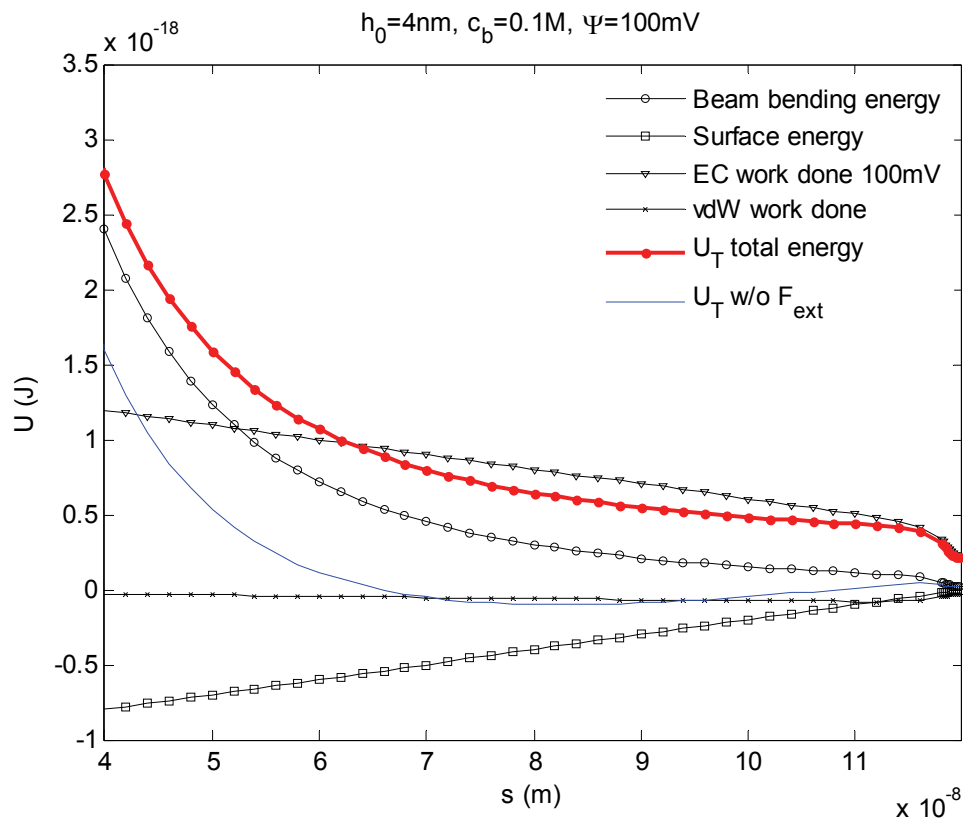Figure 85. Energy curves when $h_0 = 4\,\text{nm}, c_b = 0.1\,\text{M}, \Psi = 75\,\text{mV}$

Figure 86. Energy curves when $h_0 = 4\,\mathrm{nm}, c_b = 0.1\,\mathrm{M}, \Psi = 100\,\mathrm{mV}$

The equilibrium position of the total energy curves of the system which has 4nm height and 0.1M ion concentration keep moved to the right hand side and was removed when the applied potential was 100mV. Figure 86 shows that the total energy curve does not have a energy well in between the beam length. The stiction of this beam could be released with 100mV applied potential.
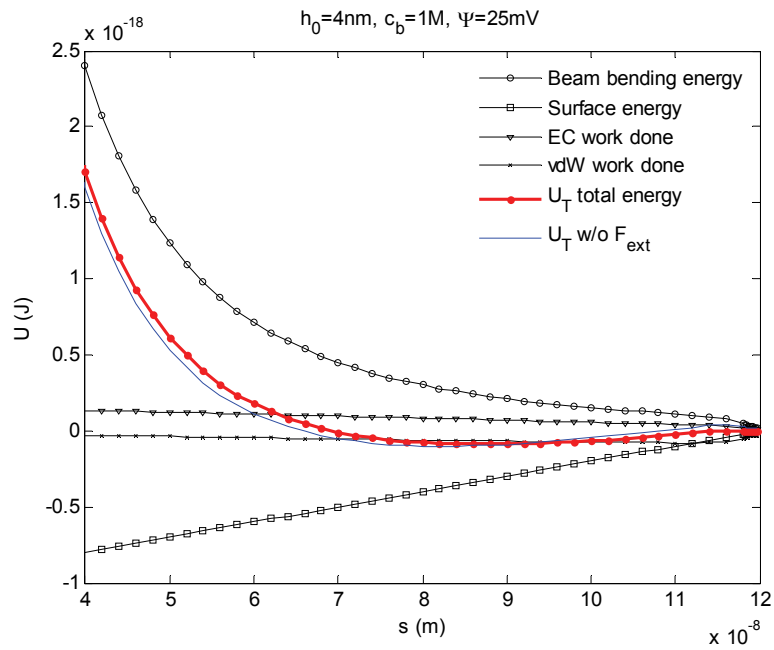
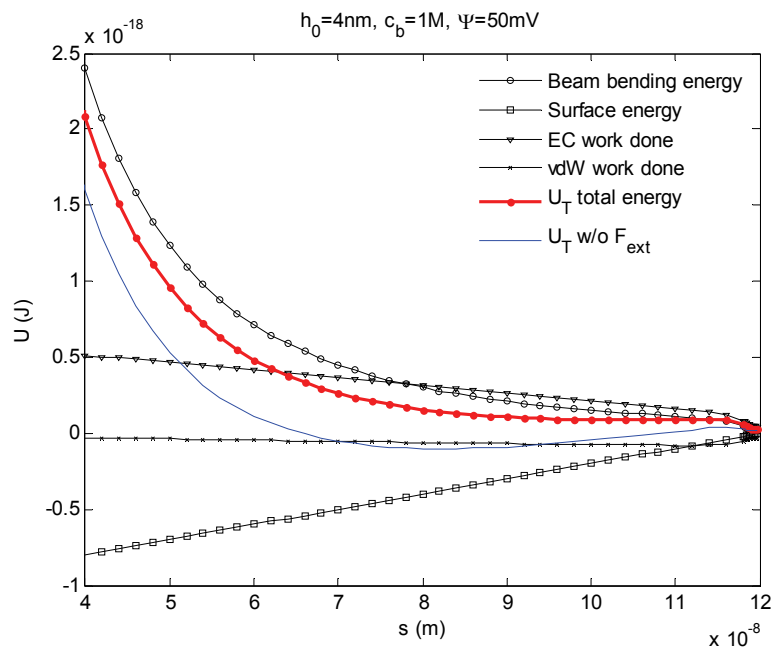Figure 87. Energy curves when $h_0 = 4\,\text{nm}, c_b = 1\,\text{M}, \Psi = 25\,\text{mV}$

Figure 88. Energy curves when $h_0 = 4\,\text{nm}, c_b = 1\,\text{M}, \Psi = 50\,\text{mV}$

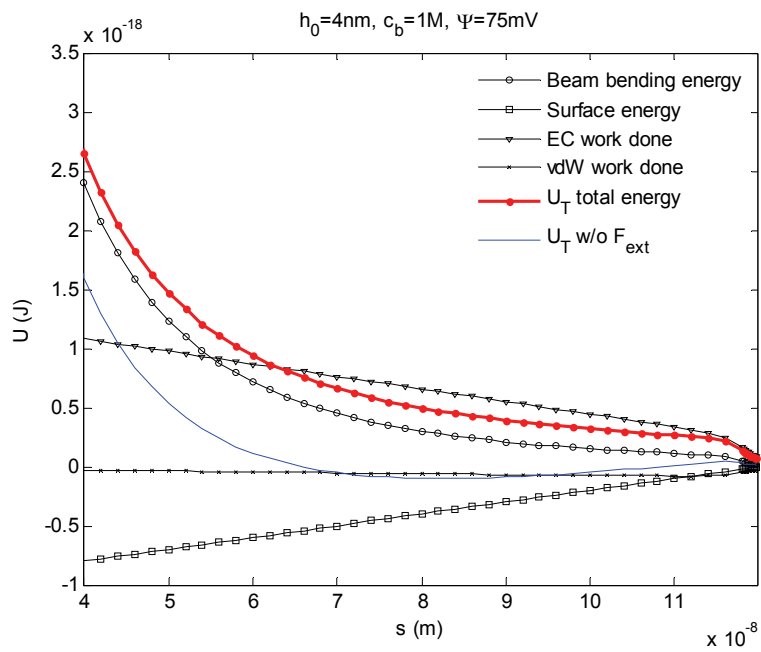Figure 89. Energy curves when $h_0 = 4\,\mathrm{nm}, c_b = 1\,\mathrm{M}, \Psi = 75\,\mathrm{mV}$

Figure 90. Energy curves when $h_0 = 4\,\mathrm{nm}, c_b = 1\,\mathrm{M}, \Psi = 100\,\mathrm{mV}$

The equilibrium position of the total energy curves of the system which has 4nm height and 1M ion concentration keep moved to the right hand side and was removed when the applied potential was larger than 75mV. The stiction of this beam could be released with applied potentials larger than 75mV.

Figures 91-102 show each energies and total energy distributions versus s when h_0 is 5nm.

Figure 91. Energy curves when $h_0 = 5\,\text{nm}, c_b = 0.01\text{M}, \Psi = 25\text{mV}$

Figure 92. Energy curves when $h_0 = 5\,\mathrm{nm}, c_b = 0.01\mathrm{M}, \Psi = 50\mathrm{mV}$

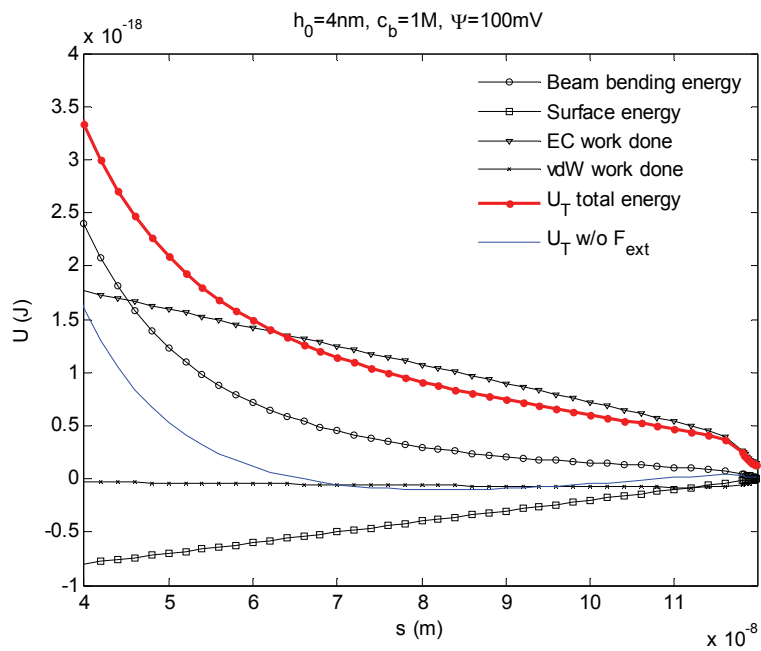Figure 93. Energy curves when $h_0 = 5\,\mathrm{nm}, c_b = 0.01\mathrm{M}, \Psi = 75\mathrm{mV}$

Figure 94. Energy curves when $h_0 = 5\,\text{nm}, c_b = 0.01\,\text{M}, \Psi = 100\,\text{mV}$

The equilibrium position of the total energy curves of the system which has 5nm height and 0.01M ion concentration keep moved to the right hand side and was removed when the applied potential was 100mV. The stiction of this beam could be released with lager than 100mV applied potential. The beams which have 3nm and 4nm heights could not be release in 0.01M ion concentration. But the higher bending energy because of the longer height helps the energy equilibrium position removed even in low ion concentration. The higher the height is, the easier it is to remove the equilibrium positions.
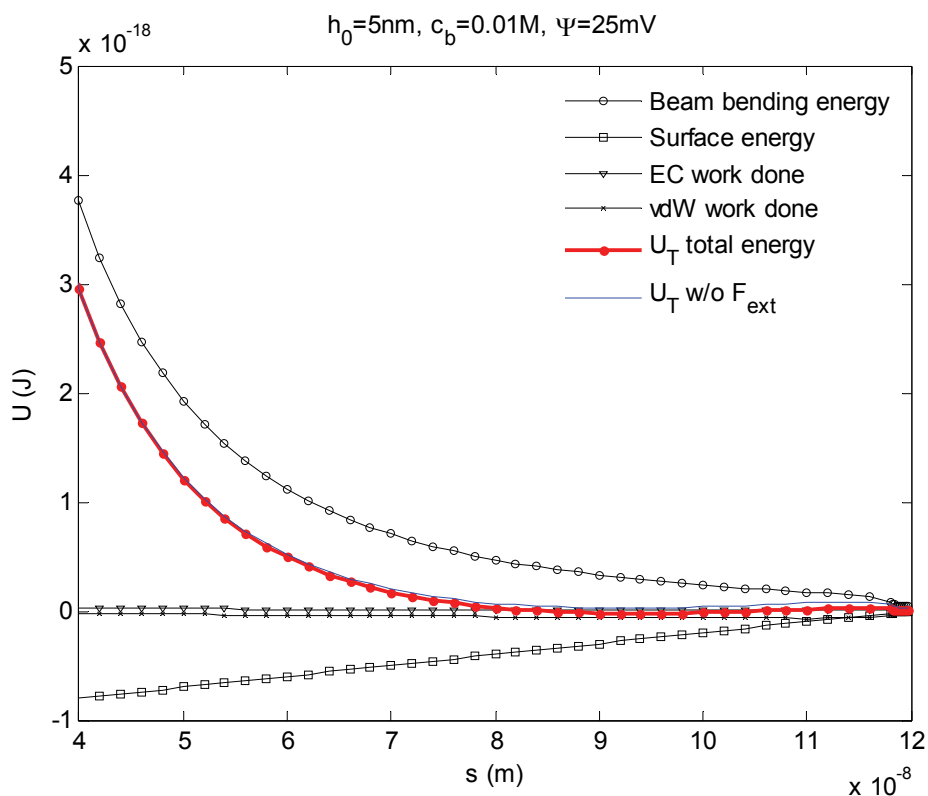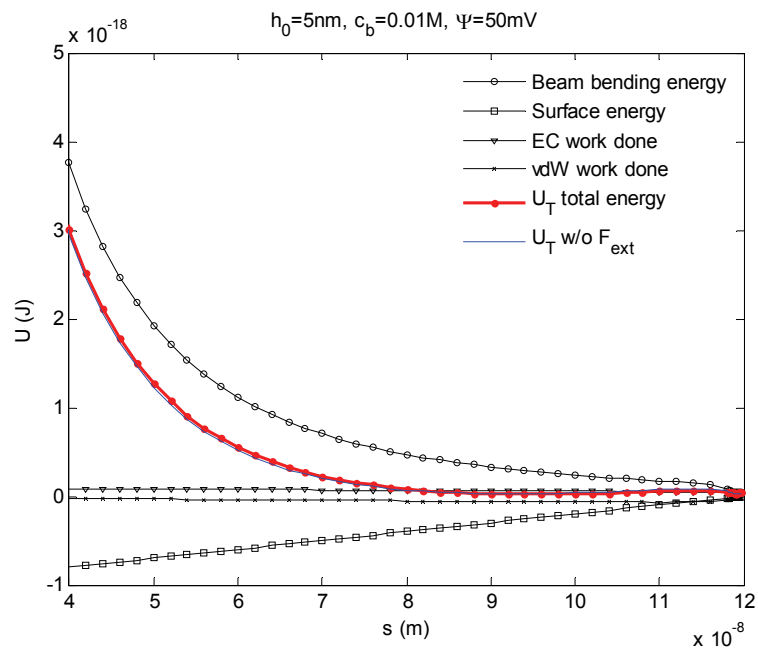
Figure 95. Energy curves when $h_0 = 5\,\text{nm}, c_b = 0.1\text{M}, \Psi = 25\text{mV}$

Figure 96. Energy curves when $h_0 = 5\,\text{nm}, c_b = 0.1\text{M}, \Psi = 50\text{mV}$

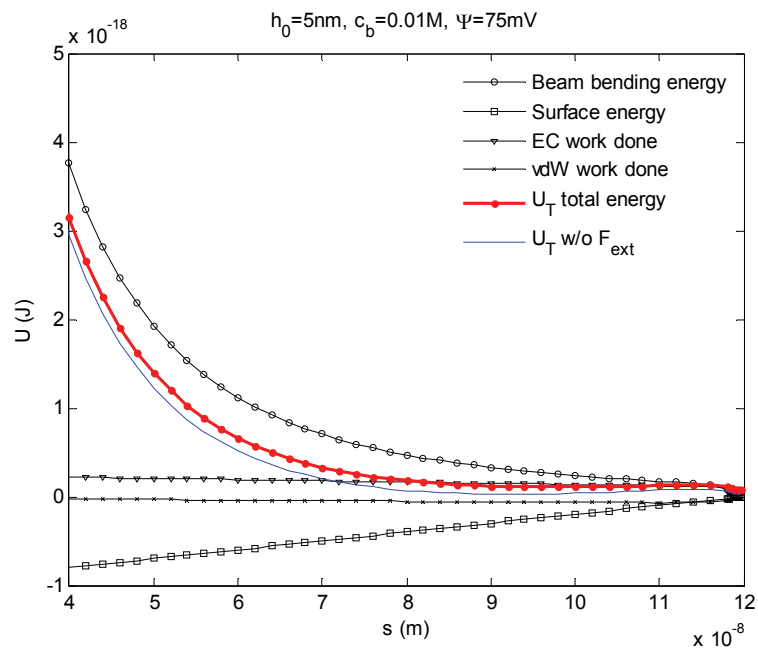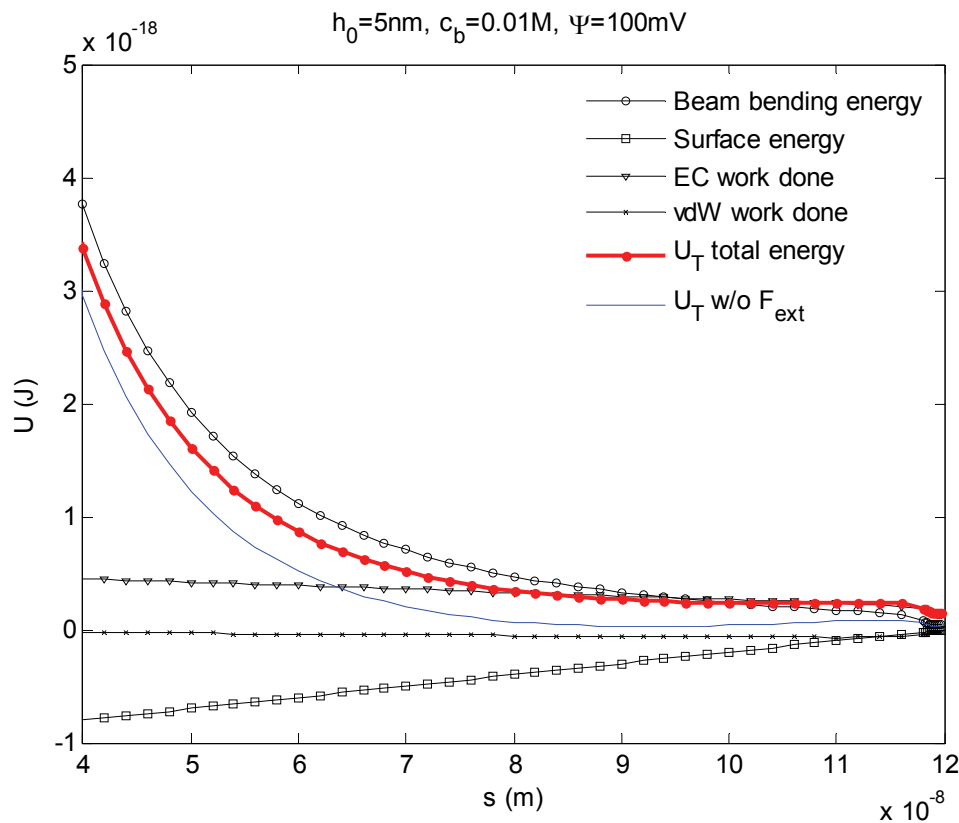Figure 97. Energy curves when $h_0 = 5\,\text{nm}, c_b = 0.1\,\text{M}, \Psi = 75\,\text{mV}$
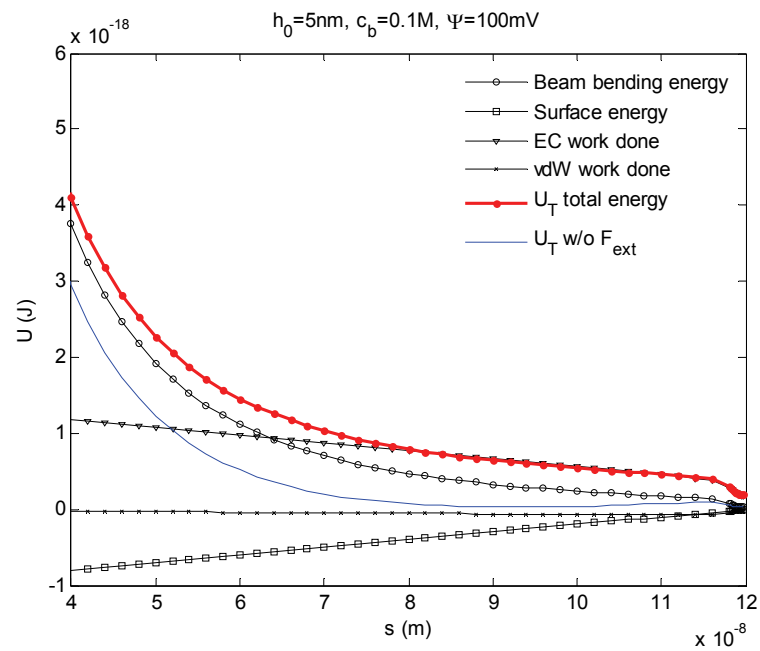
Figure 98. Energy curves when $h_0 = 5\,\text{nm}, c_b = 0.1\,\text{M}, \Psi = 100\,\text{mV}$

The equilibrium position of the total energy curves of the system which has 5nm height and 0.1M ion concentration keep moved to the right hand side and was removed when the applied potential was over 75mV. The stiction of this beam could be released with lager than 75mV applied potential.
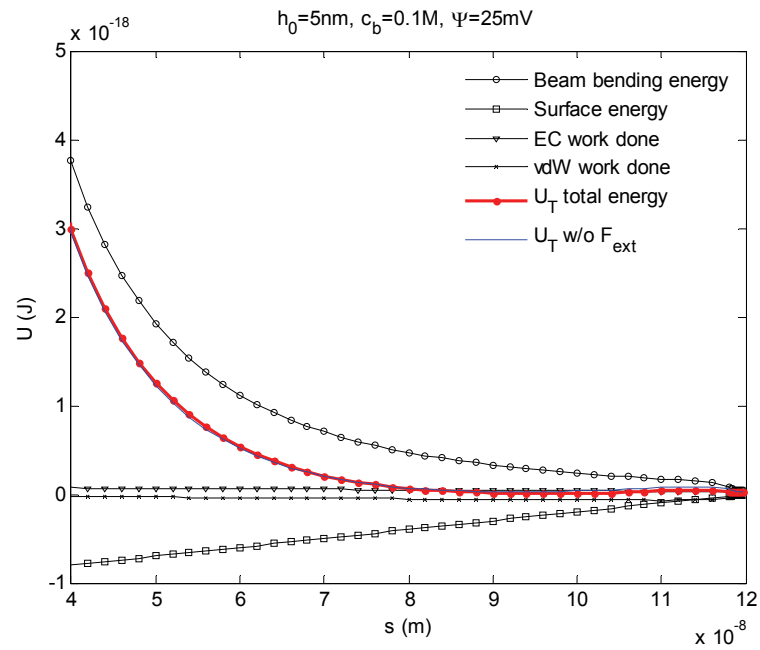

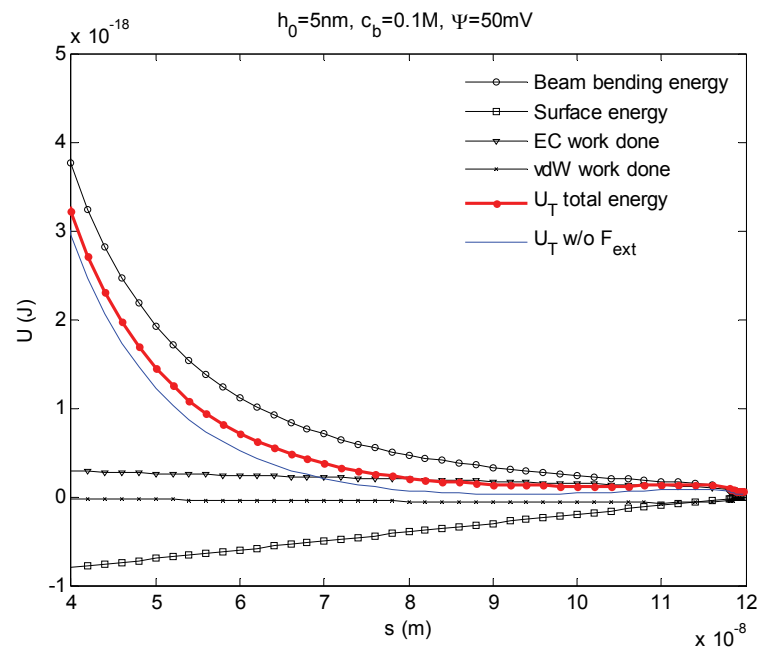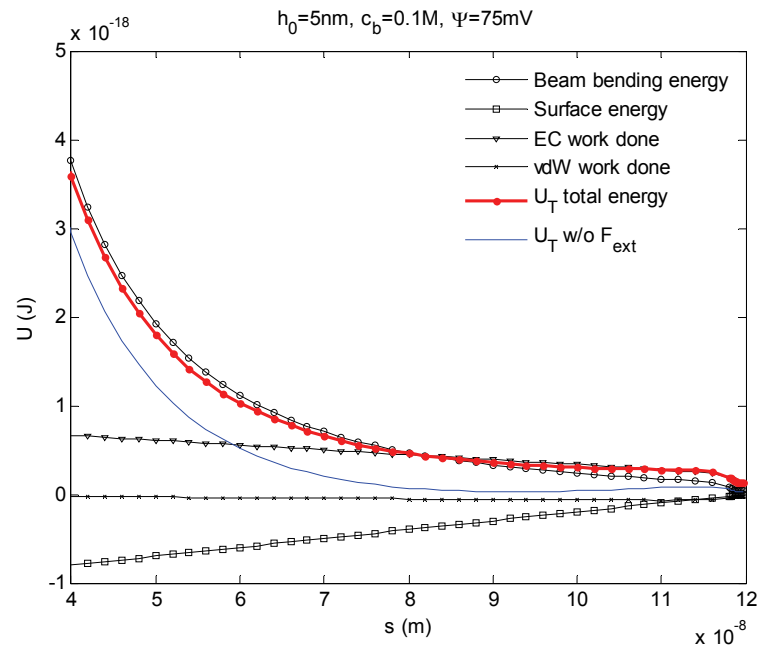Figure 99. Energy curves when $h_0 = 5\,\text{nm}, c_b = 1\,\text{M}, \Psi = 25\text{mV}$
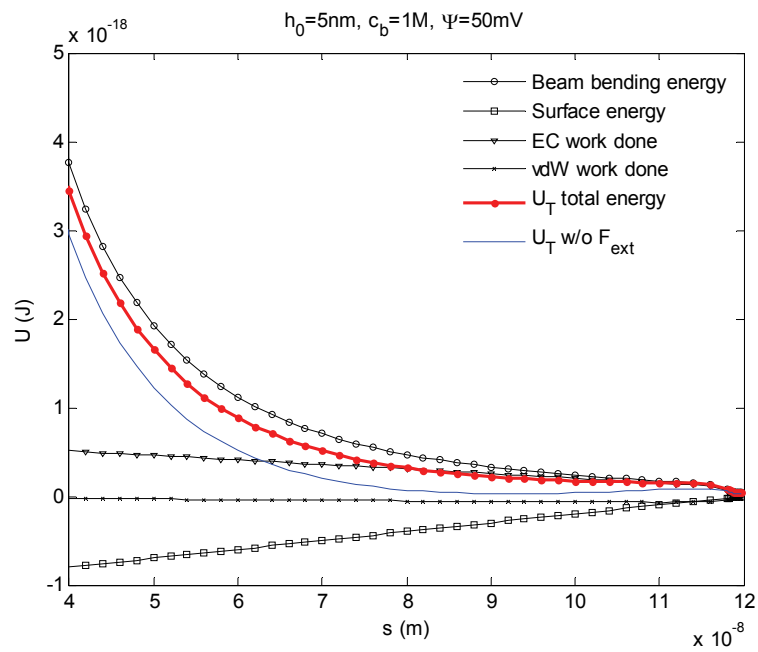
Figure 100. Energy curves when $h_0 = 5\,\text{nm}, c_b = 1\text{M}, \Psi = 50\text{mV}$
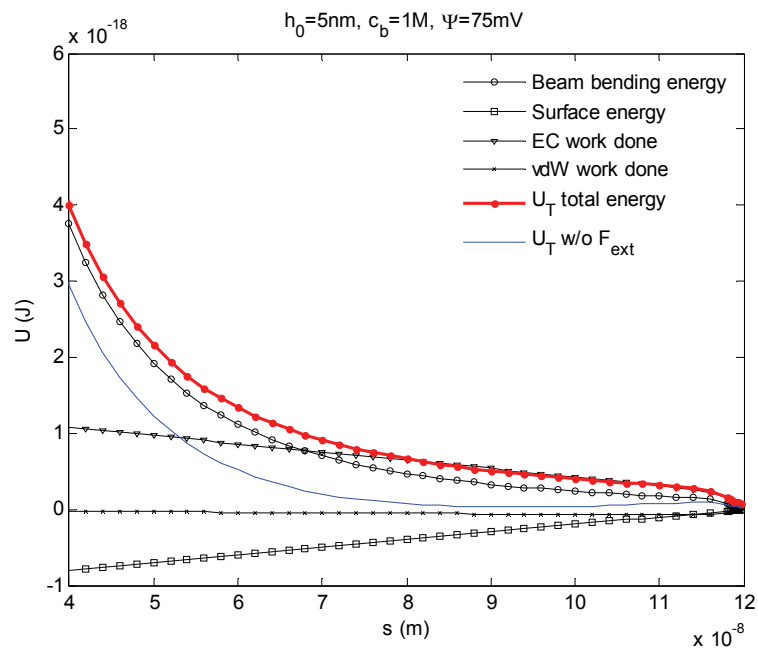
Figure 101. Energy curves when $h_0 = 5\,\text{nm}, c_b = 1\text{M}, \Psi = 75\text{mV}$
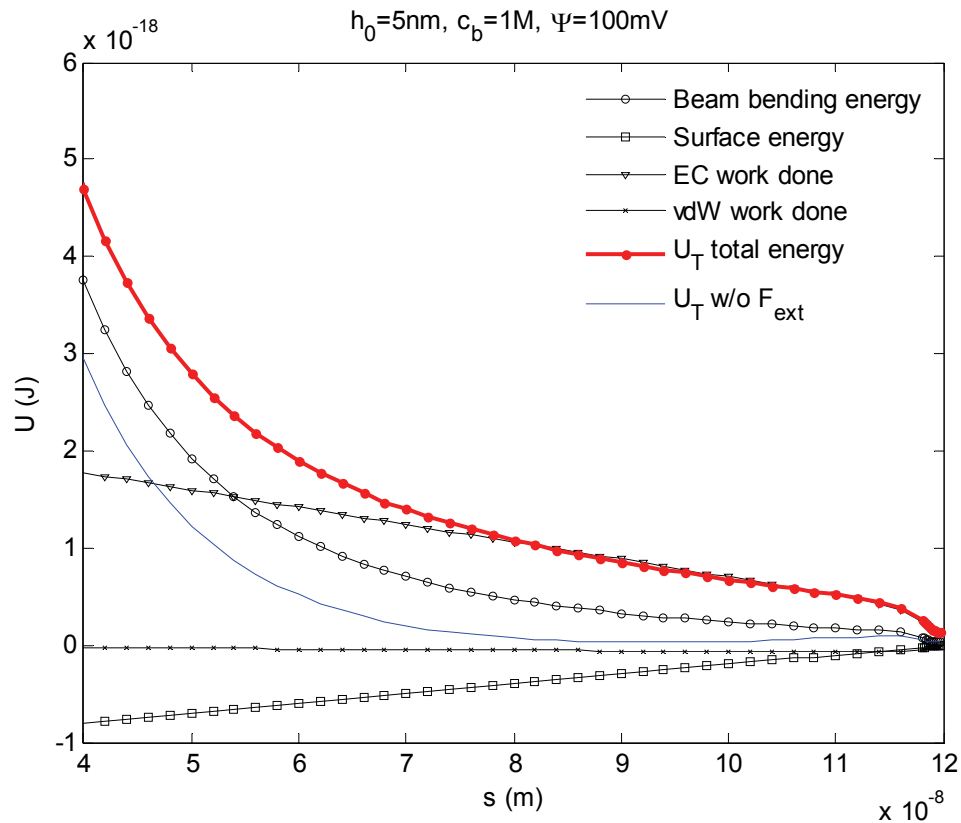
Figure 102. Energy curves when $h_0 = 5\,\mathrm{nm}, c_b = 1\mathrm{M}, \Psi = 100\mathrm{mV}$

The equilibrium position of the total energy curves of the system which has 5nm height and 1M ion concentration keep moved to the right hand side and was removed when the applied potential was larger than 50mV. The stiction of this beam could be released with applied potentials larger than 50mV.
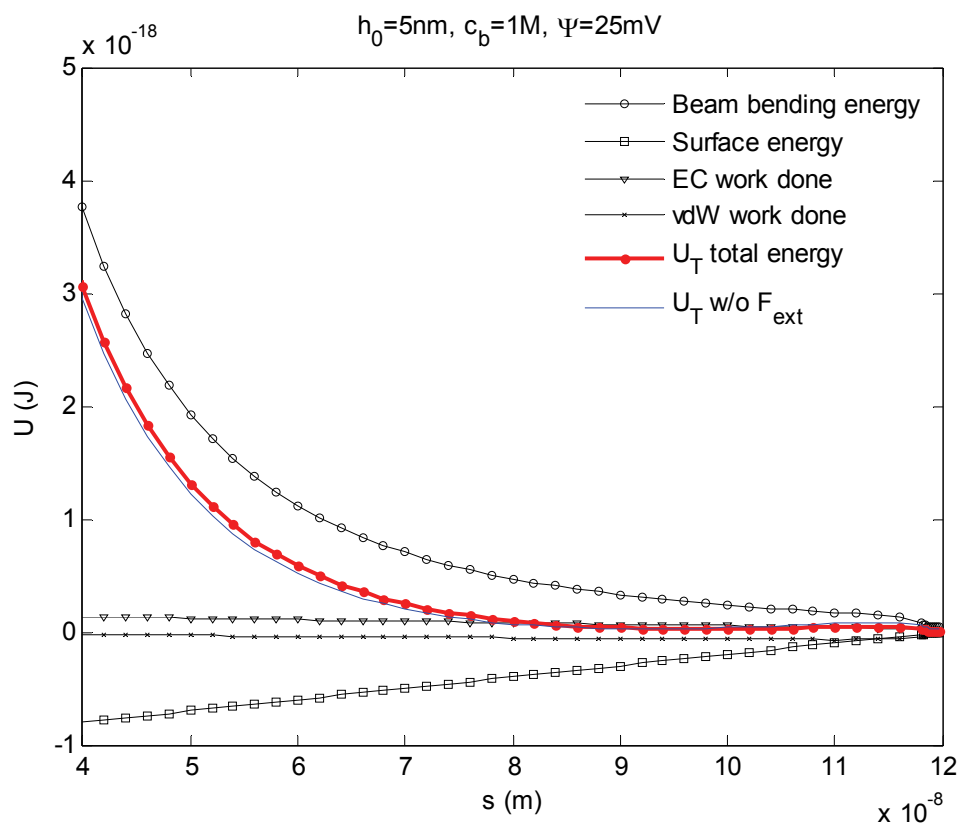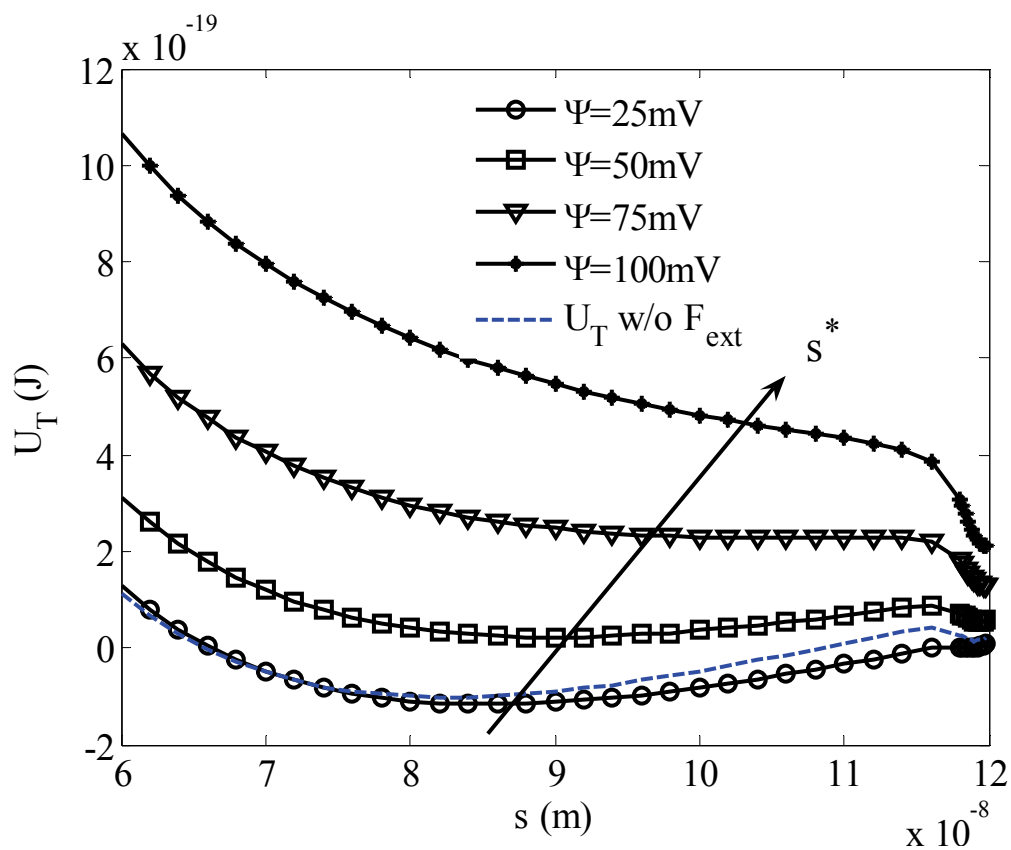
Figure 103. Total energy curves when $h_0 = 4\,\text{nm}$ and $c_b = 0.1\,\text{M}$

Figure 103 shows the total energy curves with four different applied potentials together when $h_0 = 4\,\text{nm}$ and $c_b = 0.1\,\text{M}$. The equilibrium position s^* keeps moved to the right hand and is finally removed when the applied potential is 100mV. In a given ion concentration value, the beam stiction can be release by increasing the applied potential.

Figure 104 shows electrochemical work done, W_{EC}, versus s when h_0 and c_b are fixed and Ψ is increasing from 25 to 100mV. In every case, the slope of the electrochemical work done curve versus s increased by increasing the ion concentration.
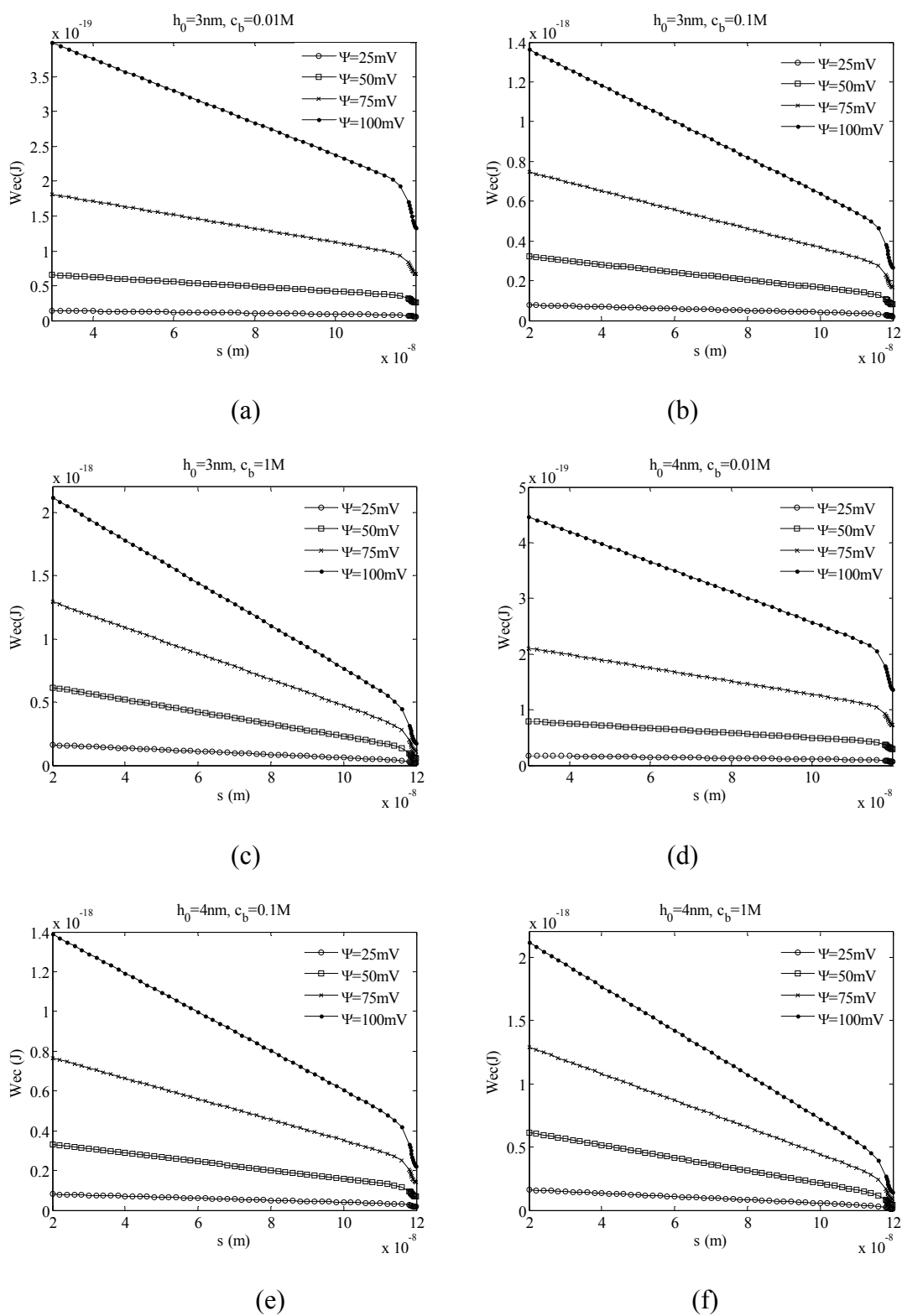
Figure 104. Electrochemical work done with different applied potentials

(g)

(h)

(i)
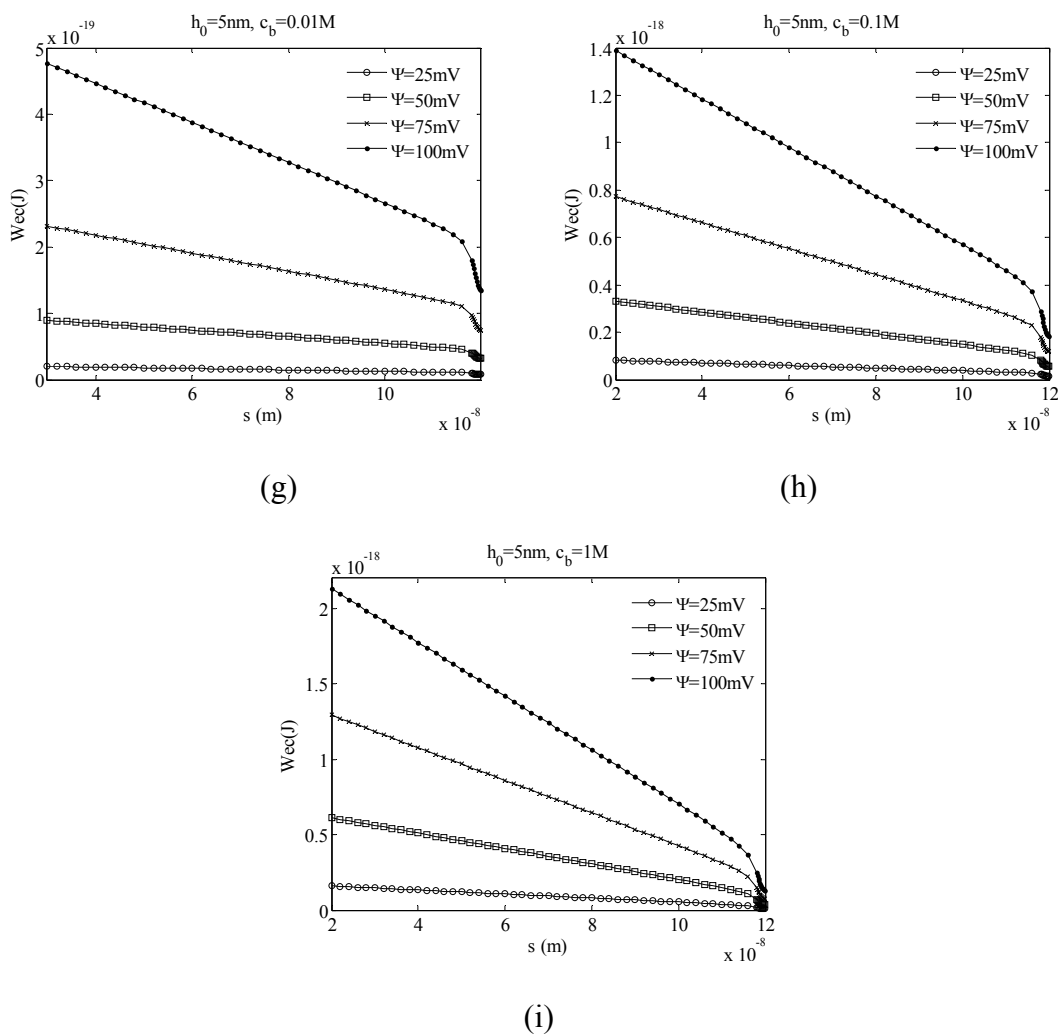
Figure 104. Continued

Figure 105 shows electrochemical work done, W_{EC}, versus s when h_0 and Ψ are fixed and c_b is increasing from 0.01M to 1M. In every case, the slope of the electrochemical work done curve versus s increased by increasing the ion concentration.
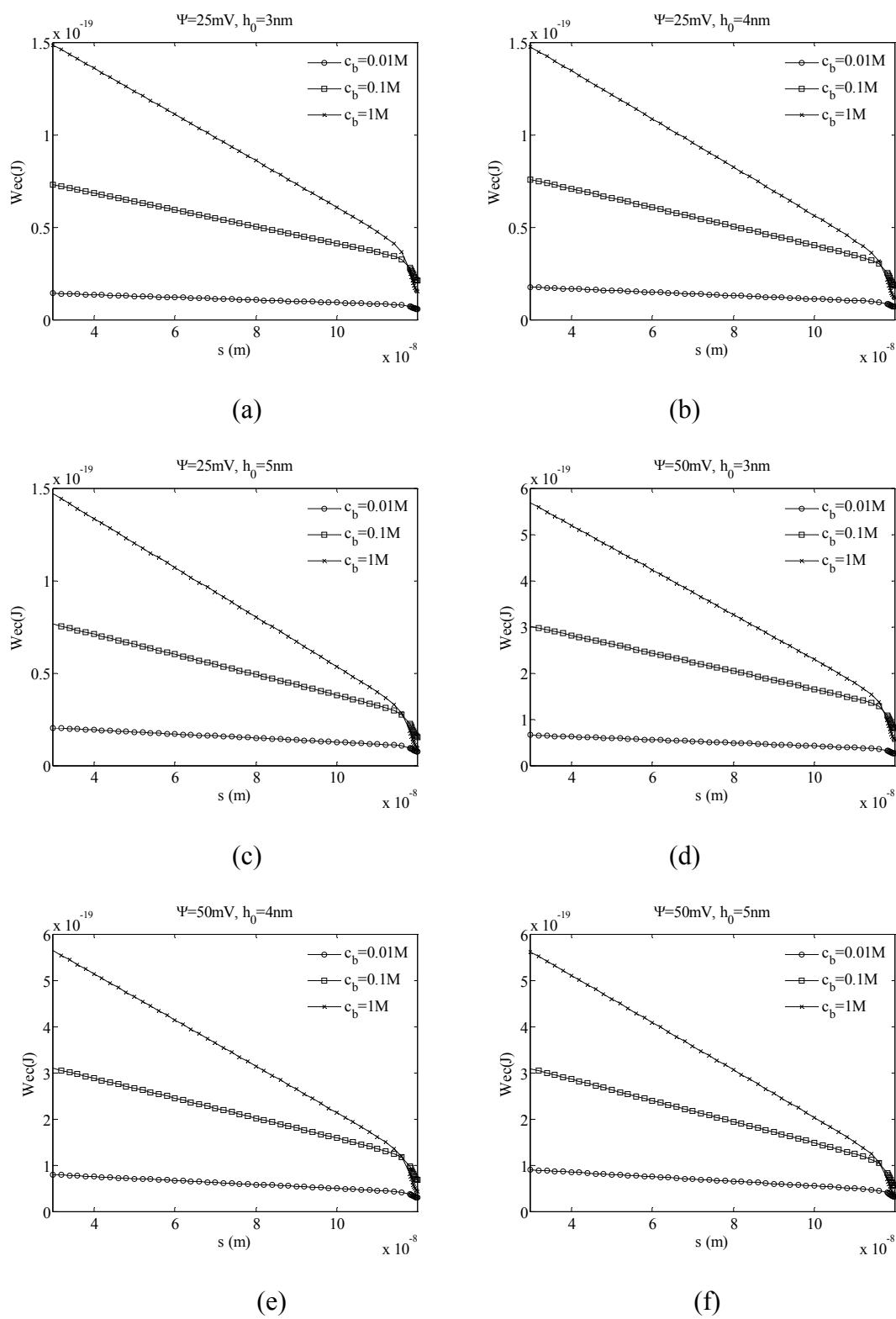
Figure 105. Electrochemical work done with different ion concentrations
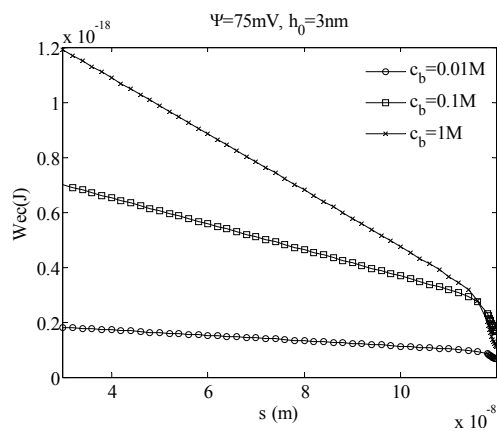
(g)
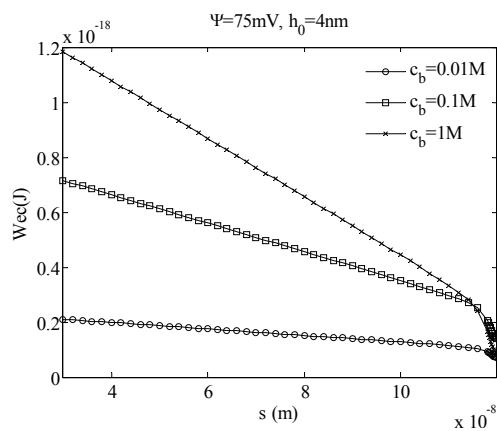
(h)
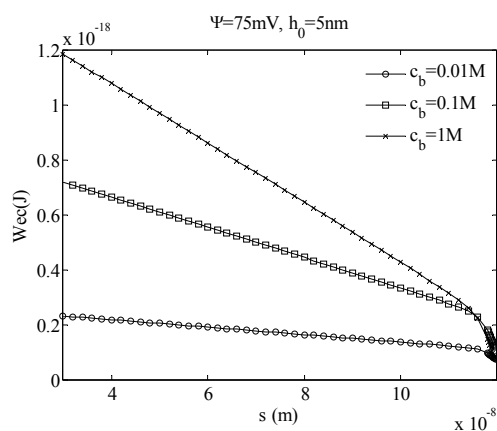
(i)
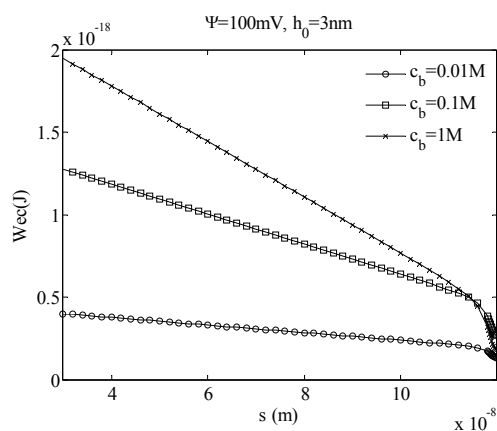
(j)
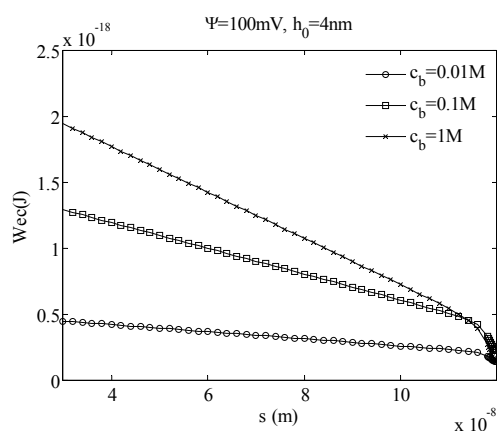
(k)
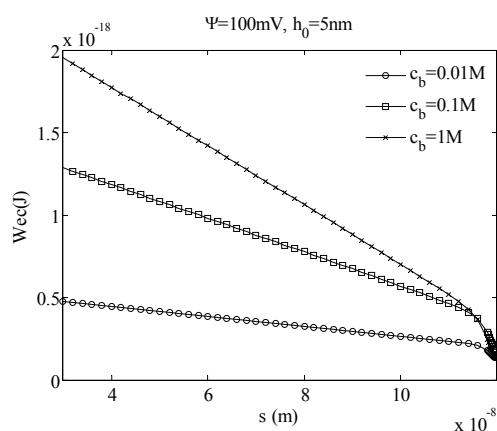
(l)

Figure 105. Continued

4.3.3. Detachment length

The stiction release was the primary concern in section 4.3.1. In this section, the method to find the maximum beam length, detachment length, without stiction will be studied. The detachment length is one of the most important design parameters in the design process if the environment is given. The effects of the slope of the external work done curve will be explained graphically.

The maximum cantilever beam length that will not stick to the substrate, or detachment length in gas was defined in equation (92). When the thickness of the beam is 4nm, the gap distance is 4nm, the Young's modulus is 153GPa and the surface adhesion energy is 5mJ/m^2, the detachment length of the beam in gas is 58.55nm. The same beam in liquids will be studied to find out the detachment length in different values of applied potentials. Energy method for six beams with different length will be studied to find out where the equilibrium position is removed.

Figure 106 shows the cantilever beam shapes in gas when the lengths of the beams are given as in table 7.

Table 7. Lengths of the beams

	Beam 1	Beam 2	Beam 3	Beam 4	Beam 5	Beam 6
Beam length(nm)	50	58.55	70	82.8	100	120

The beam 1 and the beam 2 have the length below the detachment length 58.55nm and are not stick to the substrate. The beam 3 and 4 show arc-shaped

configuration adhered to the substrate. The beam 5 and 6 are adhered to the substrate with S-shaped configuration.
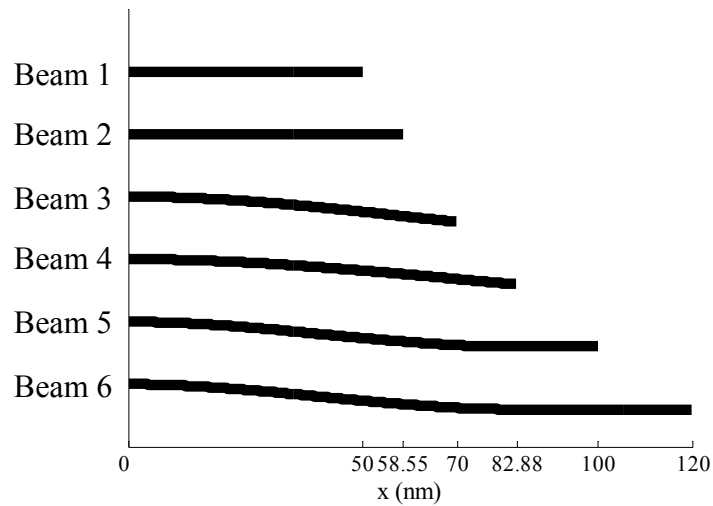
Figure 106. Beam configurations in gas for different lengths

The total energy curves when $c_b = 0.1\text{M}$, $\Psi = 50\text{mV}$ and $h_0 = 4\,\text{nm}$ with six different beams in liquids are given in figure 107. The equilibrium position exists when the beam is longer than 70nm. So, the detachment length is in between 58.55nm and 70nm.

Figure 107. Total energy curves with $c_b = 0.1\,\mathrm{M}$, $\Psi = 50\mathrm{mV}$ and $h_0 = 4\,\mathrm{nm}$ when the beam length is (a) 50nm, (b) 58.5nm, (c) 70nm, (d) 82.8nm, (e) 100nm, (f) 120nm

(e)　　　　　　　　　　　　　　　(f)

Figure 107. Continued

The external work done and the surface adhesion energy curves for each beam are given in figure 108(a) and the summation of those two are given in figure 108(b). The external work done curves show linear distributions and can be assumed to have slope S which is always negative. The slope of the surface adhesion energy curves is $\gamma_s w$ as given in equation (90). Because the absolute value of S is relatively smaller than $\gamma_s w$, the slope of the energy summation curves in figure 108(b) still show positive values.

(a)   (b)
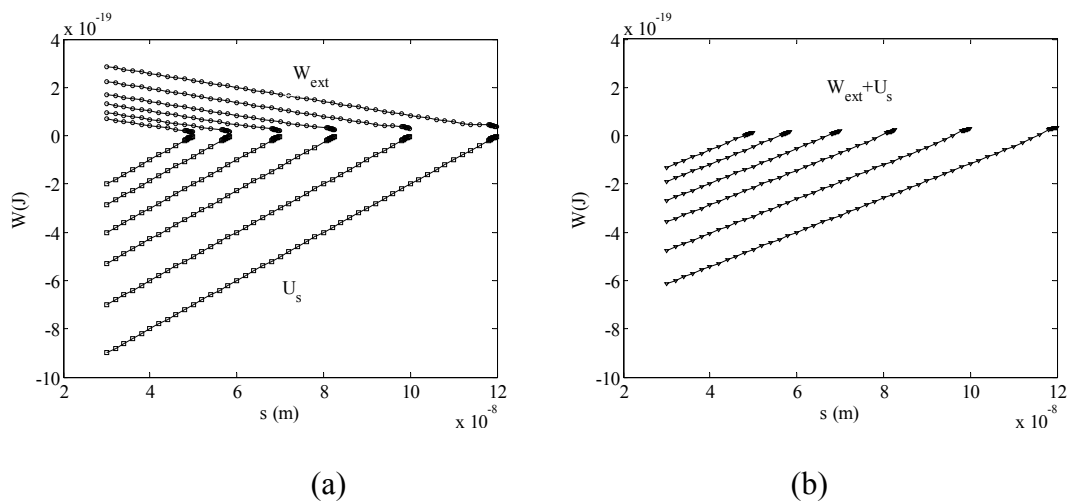
Figure 108. (a) W_{ext} and U_s (b) $W_{ext}+U_s$ when $c_b = 0.1M$, $\Psi = 50mV$ and $h_0 = 4nm$

The total energy curves when $c_b = 0.1M$, $\Psi = 75mV$ and $h_0 = 4nm$ with six different beams in liquids are given in figure 109. The equilibrium position exists when the beam is longer than 120nm. The detachment length is in between 100nm and 120nm.

(a)   (b)
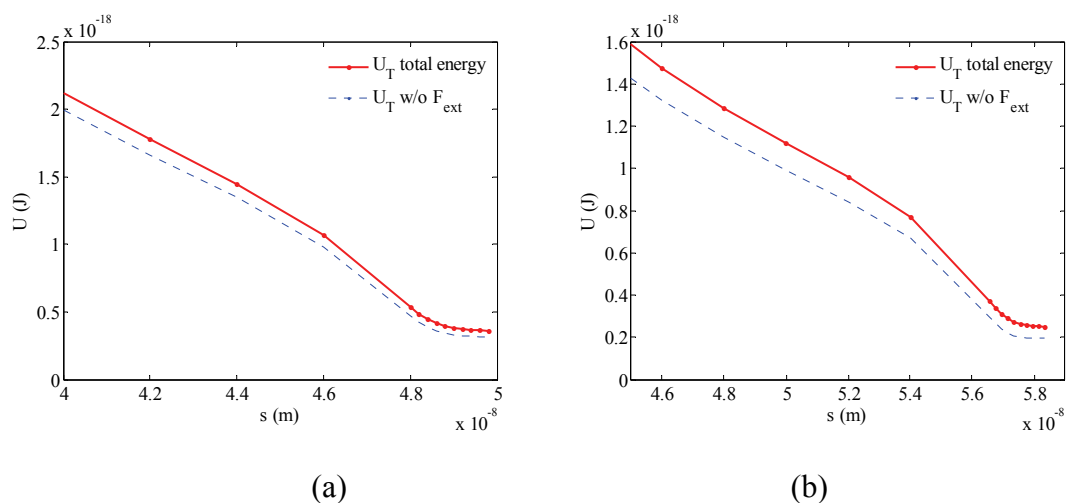
Figure 109. Total energy curves with $c_b = 0.1M$, $\Psi = 75mV$ and $h_0 = 4nm$ when the beam length is (a) 50nm, (b) 58.5nm, (c) 70nm, (d) 82.8nm, (e) 100nm, (f) 120nm
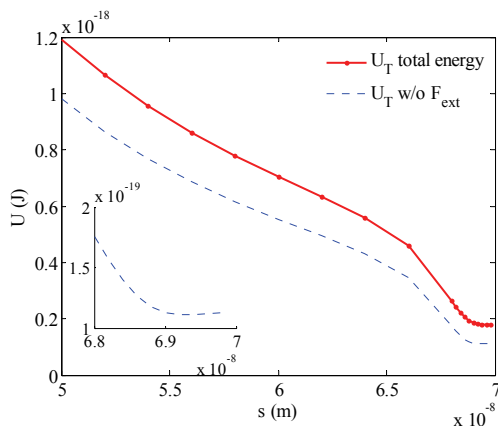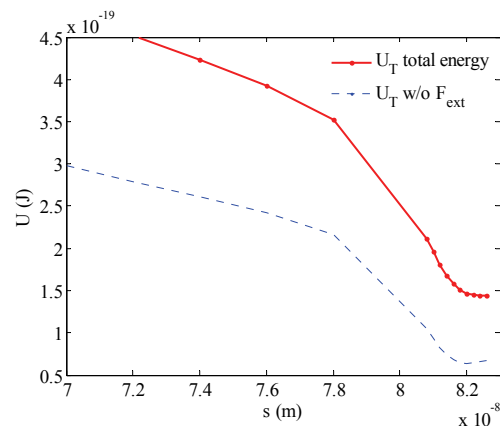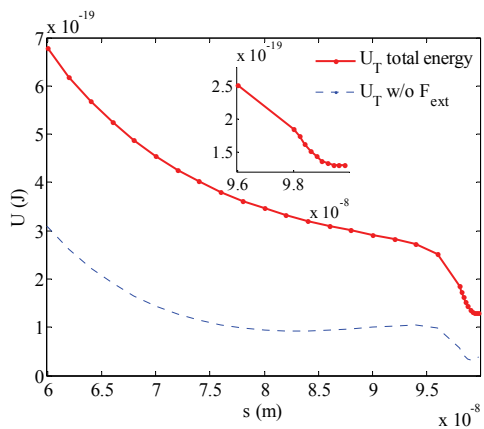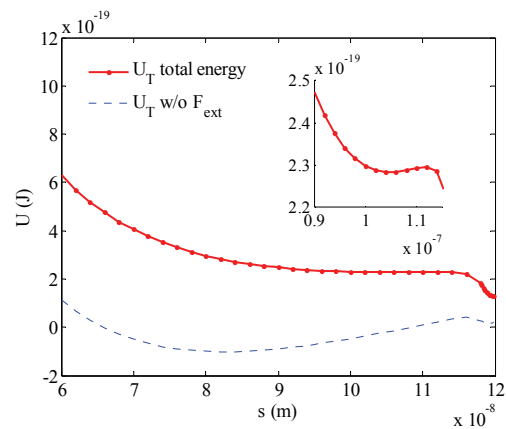
Figure 109. Continued

The external work done and the surface adhesion energy curves for each beams are given in figure 110(a) and the summation of those two are given in figure 110(b). Because the absolute value of S is just a little bit less than $\gamma_s w$, the slope of the energy summation curves in figure 110(b) show low but still positive values.

(a)   (b)
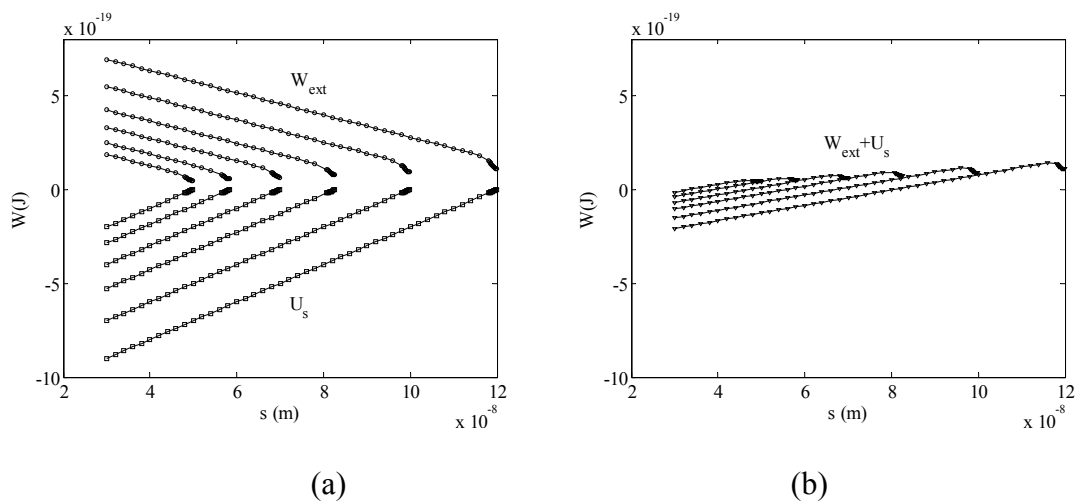
Figure 110. (a) W_{ext} and U_s (b) $W_{ext}+U_s$ when $c_b = 0.1M$, $\Psi = 75mV$ and $h_0 = 4nm$

The total energy curves when $c_b = 0.1M$, $\Psi = 100mV$ and $h_0 = 4nm$ with six different beams in liquids are given in figure 111. The equilibrium positions exist for all beams. It means that all beams do not stick to the substrate whatever the beam length is.

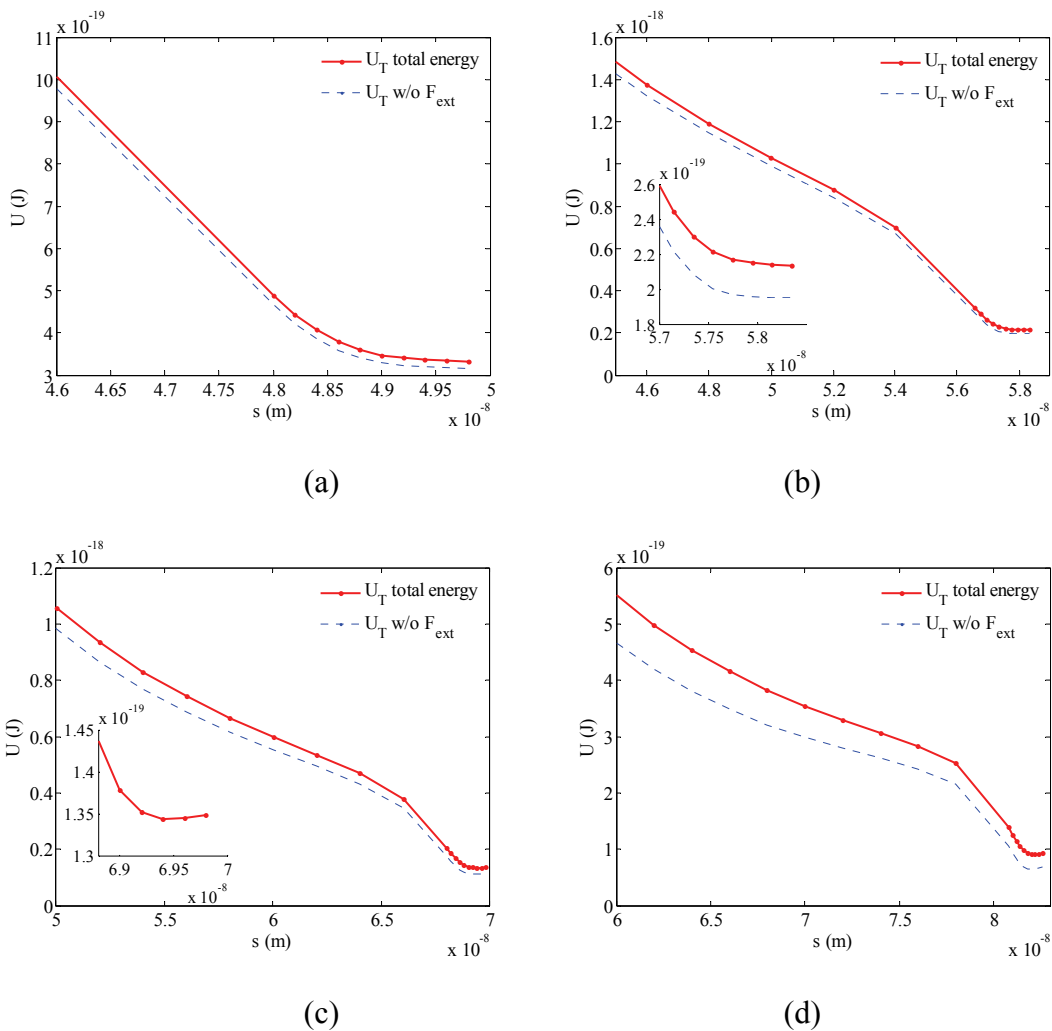
(a)   (b)
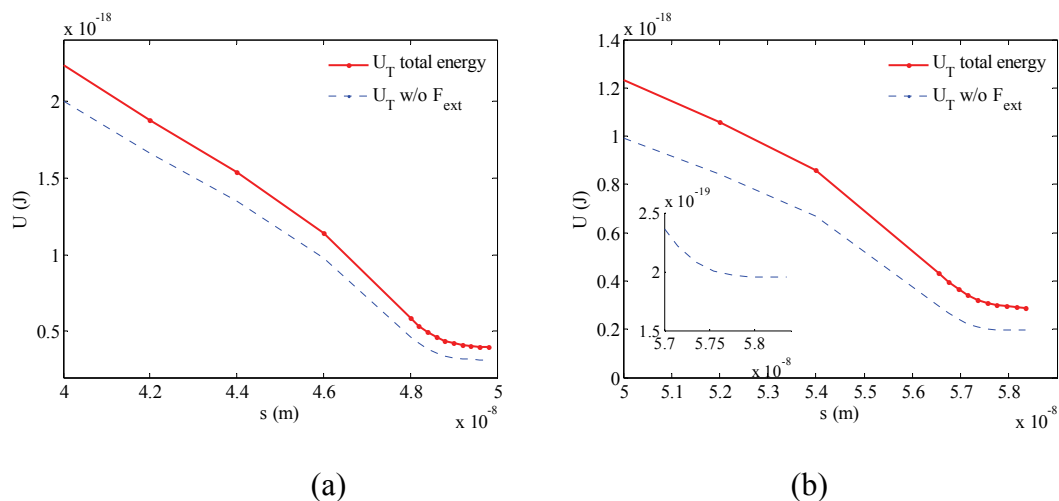
Figure 111. Total energy curves with $c_b = 0.1M$, $\Psi = 100mV$ and $h_0 = 4nm$ when the beam length is (a) 50nm, (b) 58.5nm, (c) 70nm, (d) 82.8nm, (e) 100nm, (f) 120nm
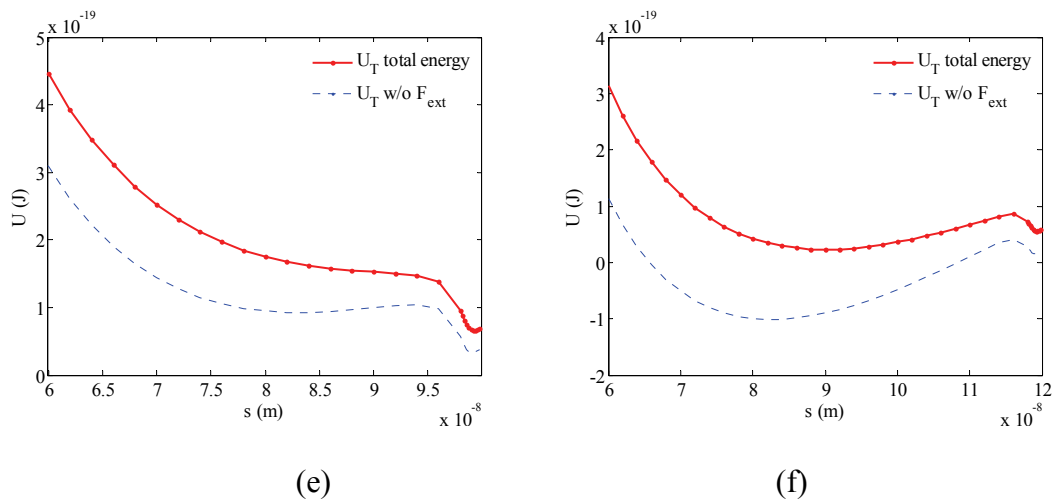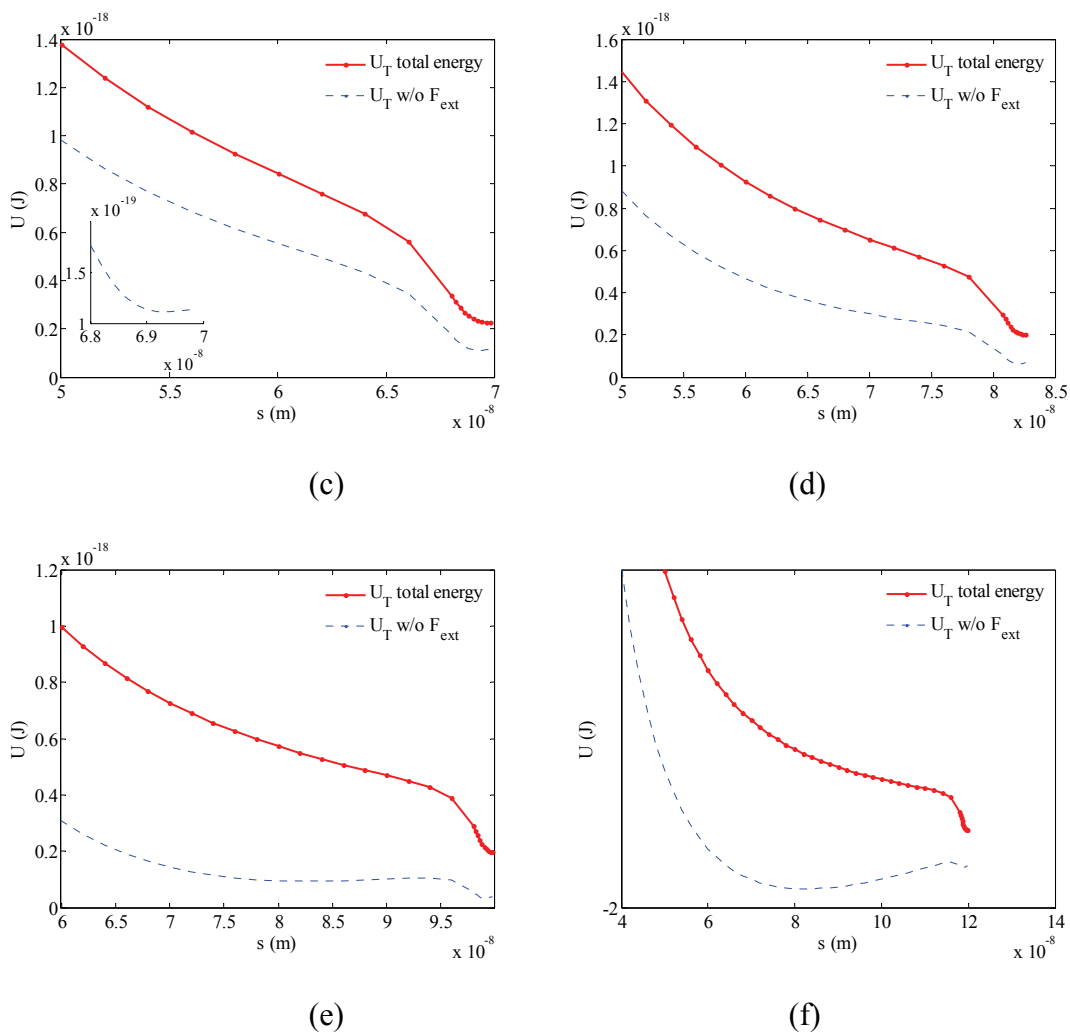
Figure 111. Continued

The external work done and the surface adhesion energy curves for each beam are given in figure 112(a) and the summation of those two are given in figure 112(b). Because the absolute value of S is larger less than $\gamma_s w$, the slope of the energy summation curves in figure 112(b) show negative values. It means that the external work done overcome the surface adhesion energy and the beams are free from stiction.

(a)   (b)
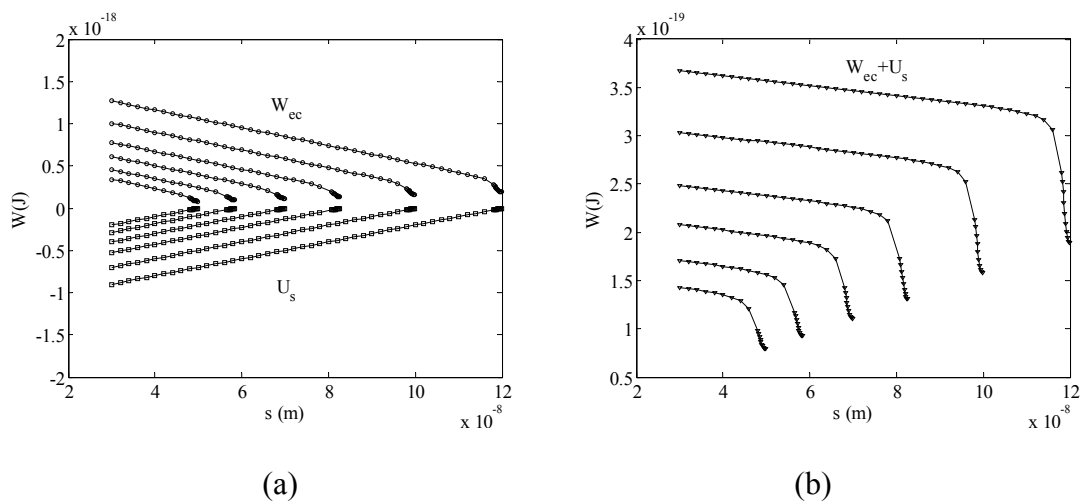
Figure 112. (a) W_{ext} and U_s (b) W_{ext}+U_s when $c_b = 0.1M$, $\Psi = 100mV$ and $h_0 = 4\,nm$

(a)   (b)
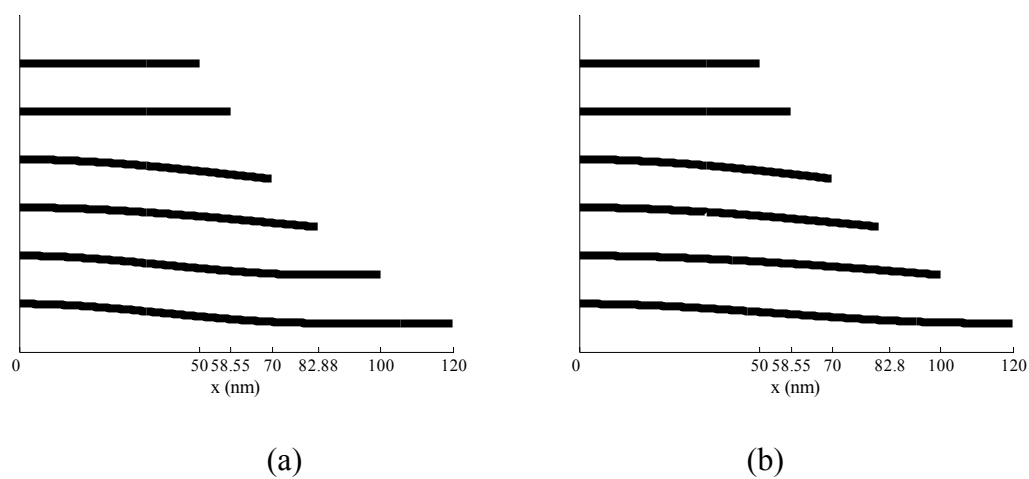
Figure 113. Beam configuration in (a) no external forces, (b) $\Psi = 50mV$, (c) $\Psi = 75mV$, (d) $\Psi = 100mV$

(c)   (d)
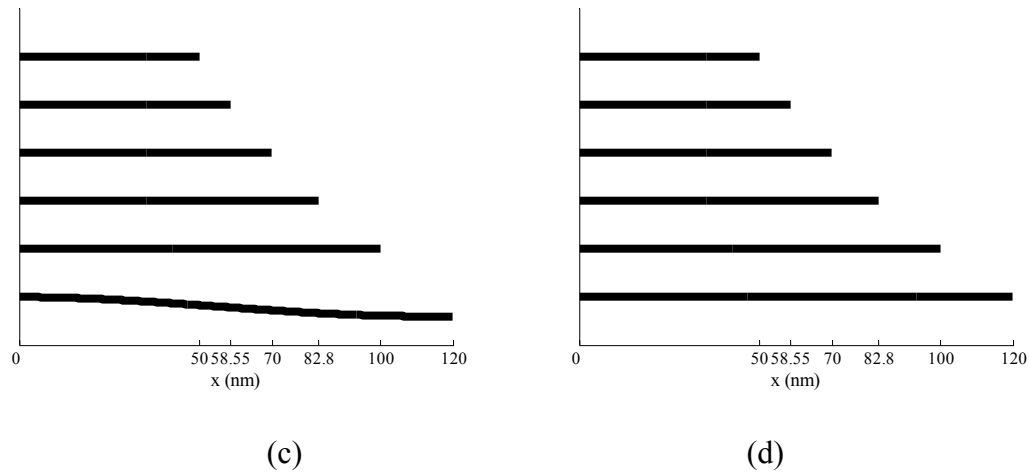
Figure 113. Continued

Figure 113 shows the beam configuration with four different applied voltages.

4.4. Summary

The standard beam stiction test used in gas was modified for NEMS in liquids by adding the van der Waals work done and the electrochemical work done. The equilibrium positions for the nano cantilever beam in liquids could be obtained graphically by numerical simulation using the COMSOL software. The parametric studies showed that the stiction occurred in a gas could be free by submersing the beams in liquid electrolyte and applying proper amount of electric potential. The stiction could be permanently free when the absolute value of the linear slope of external work done was greater than the slope of the surface adhesion energy curve. The maximum cantilever beam length that will not stick to the substrate, the detachment length, can be increased by increasing the ion concentrations and the applied electric potentials.

This research has developed useful numerical processing methods to find parameters to free the stiction of the beams and determine the detachment length of the beams in liquid electrolytes.

5. CONCLUSIONS AND FUTURE WORK

5.1. Conclusions

This dissertation brings together the work of the colloidal science community and the MEMS and NEMS electrostatic device community.

This research is the first study of the deflection, pull-in instability, and stiction of nanoscale beams in liquid electrolyte that includes the following features: elastic forces, electrostatic forces, osmotic forces, van der Waals forces, and adhesion (stiction) forces, in which the beam is modeled as a continuous structure, i.e. not a discrete spring.

The pressure between two parallel planar surfaces at identical electric potentials is calculated using both the classical Poisson-Boltzmann (PB) equation and the modified PB equation of Borukhov *et al* to account for finite ion size. The pressure predicted by the two models differs more as the bulk ion concentration, surface potential, and ion size increase. The ratio of the pressures predicted by the two models is relatively independent of the separation of the two plates.

A beam suspended horizontally over a substrate was modeled using simple beam theory. The linearized Poisson-Boltzmann equation was used to determine the electric potential distribution between the beam and the substrate. The electric potential was then used to determine the electric force, the ion concentrations, and the (linearized) osmotic force. The van der Waals force was included. It was determined that the problem is governed by four nondimensional parameters. The governing equations were solved

using the COMSOL finite element software. For a gas or vacuum, the finite element results were verified by comparing to published results.

The standard beam stiction problem for MEMS in gas was modified for NEMS in liquids by adding the van der Waals work and the electrochemical work. The equilibrium positions for the nano cantilever beam in liquids were obtained graphically by numerical simulation using COMSOL. Parametric studies demonstrated that stiction that occurs in a gas could be freed by submersing the beam in liquid electrolyte. The stiction could be permanently freed when the absolute value of the slope of the external work done curve was over the slope of the surface adhesion energy curve. The maximum cantilever beam length that will not stick to the substrate, the detachment length, can be increased by increasing the ion concentrations and the surface electric potentials. This research has developed a useful numerical processing method to find the parameters to free the stiction of the beams and determine the detachment length of the beams in liquid electrolyte.

5.2. Future Work

In section 2, the total pressure between two parallel plates in a liquid electrolyte was derived only when the two plates are at the same electric potential. Future work should calculate the pressure when the two plates are at different electric potentials and verify that the total pressure is uniform between the two plates.

The MPB equation used in this research was derived by assuming that the positive ion, the negative ion and the solvent molecule are same size. Future work should account for chemical species with different sizes.

This research did not include a finite element analysis of the fringing effect. Future work should include a finite element study of the fringing effect.

In this research, we developed a process to study the stiction problem in liquid electrolytes. Some parametric studies have been performed to show how the stiction problem in liquid electrolyte is solved. Future work should include more parametric studies to better determine how each parameter affects the beam bending and stiction.

REFERENCES

[1] C M Niemeyer 2001 Nanoparticles, proteins, and nucleic acids: biotechnology meets materials science *Journal of Chemical Education*. **40** 4128-4158

[2] C H Mastrangelo and C H Hsu 1993 Mechanical stability and adhesion of microstructures under capillary force-Part I: Basic theory *Journal of Microelectromechanical Systems* **2** (1): 33-43

[3] J Wu, G K Fedder and L R Carley 2004 Accelerometer A low-noise low-offset capacitive sensing amplifier for a 50-μg/√Hz monolithic CMOS MEMS accelerometer *IEEE Journal of Solid-State Circuits* 39 (5): 722-730

[4] M Saukoski, L Aaltonen, T Salo and K Halonen 2008 Interface and control electronics for a bulk micromachined capacitive gyroscope *Sensors and Actuators A* **147** 183-193

[5] W C Tang, T H Nguyen and R T Howe 1989 Laterally driven polysilicon resonant microstructures *Sensors and Actuators* **20** 25-32

[6] S L Miller, M S Rodgers, G L Vigne, J J Sniegowski, P Clews, D M Tanner and K A Peterson 1999 Failure modes in surface micromachined microelectromechanical actuation systems *Microelectronics Reliability* **39** 1229-1237

[7] R A Lawton 2000 Railure analysis of tungsten coated polysilicon micromachined microengines *Proceedings of SPIE MEMS Reliability for Critical Applications* **4180** 49-57

[8] D H Jun, W Y Sim and S S Yang 2007 A novel constant delivery thermopneumatic micropump using surface tensions *Sensors and Actuators A* **139** 210-215

[9] K Hane and M Sasaki 2008 Micro-mirrors *Comprehensive Microsystems* **3** 1-63

[10] D Kim and D J Beebe 2007 A bi-polymer micro one-way valve *Sensors and Actuators* A **136** 426-433

[11] A Agarwal, K Buddharaju, I K Lao, N Singh, N Balasubramanian and D L Kwong 2008 Silicon nanowire sensor array using top-down CMOS technology *Sensors and Actuators A* **145-146** 207-213

[12] A Loui, F T Goericke, T V Ratto, J Lee, B R Hart and W P King 2008 The effect of piezoresistive microcantilever geometry on cantilever sensitivity during surface stress chemical sensing *Sensors and Actuators A* **147** 516-521

[13] H Chang, J M Tsai, H Tsai and W Fang 2006 Design, fabrication, and testing of a 3-DOF HARM micromanipulator on (1 1 1) silicon substrate *Sensors and Actuators A* **125** 438-445

[14] M Saito, K Nakagawa, K Yamanaka, Y Takamura, G Hashiguchi and E Tamiya 2006 A new design of knife-edged AFM probe for chromosome precision manipulatin *Sensors and Actuators A* **130-131** 616-624

[15] P Kim and C M Lieber 1999 Nanotube nanotweezers *Science* **286** 2148-2150

[16] S Huang, H Tao, I Lin and X Zhang 2008 Development of double-cantilever infrared detectors: fabrication, curvature control and demonstration of thermal detection *Sensors and Actuators A* **145-146** 231-240

[17] C Ke and H D Espinosa 2006 In situ electron microscopy electromechanical characterization of a bistable NEMS device *Small* **2** (12): 1484-1489

[18] I Borukhov, D Andelman and H Orland 2000 Adsorption of large ions from an electrolyte solution: a modified Poisson-Boltzmann equation *Electrochimica Acta* **46** 221-229

[19] G Gouy 1910 Constitution of the electric charge at the surface of an electrolyte *France Journal of Physics* **9** 457-467

[20] D L Chapman 1913 A contribution to the theory of electrocapillarity *Philosophical Magazine* **25** 475-481

[21] A J Bard, L R Faulkner 2001 *Electrochemical Methods : Fundamentals and Applications* 2nd Edition (John Wiley, New York)

[22] W B Russel, D A Saville and W R Schowalter 1989 *Colloidal Dispersions* (Cambridge University Press, Cambridge)

[23] E J W Verwey and J T G Overbeek 1948 *Theory of the Stability of Lyophobic Colloids*" (American Elsevier Publishing Company, New York) 66-76

[24] J Isrelachvili 1992 *Intermolecular and Surface Forces* (Academic Press, New York)

[25] O Stern 1924 The theory of the electrolytic double-layer *Journal of Electrochemistry* **30** 508-516

[26] I Borukhov, D Andelman and H Orland 1997 Steric effects in electrolytes: a modified Poisson-Boltzmann equation *Physical Review Letters* **79** (3): 435-438

[27] D A Porter and K E Eastering 1981 *Phase Transformations in Metals and Alloys* (Champman & Hall, London)

[28] L Y Li 2004 Transport of multicomponent ionic solutions in membrane systems *Philosophical Magazine Letters* **84** (9): 593-599

[29] J Fritz, M K Baller, H P Lang, T Strunz, E Meyer, H J Güntherodt, E Delamarche, C. Gerber and J K Gimzewski 2000 Stress at the solid-liquid interface of self-assembled monolayers on gold investigated with a nanomechanical sensor *Langmuir* **16** 9694-9696

[30] L A Pinnaduwage, V I Boiadjieve, J E Hawk, A C Gehl, G W Fernando and L C R Wijewardhana 2008 An energy conservation approach to adsorbate-induced surface stress and the extraction of binding energy using nanomechanics *Nanotechnology* **19** 105501

[31] O B Degani and Y Nemirovsky 2002 Modeling the pull-in parameters of electrostatic actuators with a novel lumped two degrees of freedom pull-in model *Sensors and Actuators* **A97-98** 569-578

[32] S Akita and Y Nakayama 2001 Nanotweezers consisting of carbon nanotubes operating in an atomic microscope *Applied Physics Letters* **79** (11): 1691-1693

[33] M Dequesnes, S V Rotkin and N R Aluru 2002 Calculation of pull-in voltages for carbon-nanotube-based nanoelectromechanical switches *Nanotechnology* **13** 120-131

[34] S V Rotkin 2002 Analytical calculations for nanoscale electromechanical systems *Electrochemical Society Proceedings* **6** 90-97

[35] W H Lin, Y P Zhao 2003 Dynamic behavior of nanoscale electrostatic actuators *Chinese Physics Letters* **20** 2070-2073

[36] A Ramezani, A Alasty and J Akbari 2007 Closed-form solutions of the pull-in instability in nano-cantilevers under electrostatic and intermolecular surface forces *International Journal of Solids and Structures* **44** 4925-4941

[37] T L Sounart and T A Michalske 2003 Electrostatic actuation without electrolysis in microfludic MEMS *IEEE, Transducers, the 12th International Conference on Solid State Sensors, Actuators, and Microsystems* (Boston, USA, June 2003) **8-12**, 615-618

[38] A S Rollier, B Legrand, D Collard and L Buchaillot 2006 The stability and pull-in voltage of electrostatic parallel-plate actuators in liquid solutions *Journal of Micromechanics and Microengineering* **16** (4): 794-801

[39] B. Legrand, A S Rollier, D Collard and L Buchaillot 2006 Suppression of the pull-in instability for parallel-plate electrostatic actuators operated in dielectric liquids *Applied Physics Letters* **88** (3) 34105

[40] W A Ducker and T J Senden 1992 Measurement of forces in liquids using a force microscope *Langmiur* **9** 1831-1836

[41] T Ishino, H Hieda, K Tanaka and N Cemma 1994 Electrical double-layer forces measured with an atomic force microscope while electrochemically controlling surface potential of the cantilever *Japanese Journal of Applied Physics* **33** 1552-1554

[42] R Raitai, M Grattarola and J B H Butt 1996 Measuring electrostatic double layer forces at high surface potentials with the atomic force microscope *Journal of Physical Chemistry* **100** 16700-16705

[43] A C Hillier, S Kim and A J Bard 1996 Measurement of double-layer forces at the electrode/electrolyte interface using the atomic force microscope: potential and anion dependent interactions *J. Phys. Chem.* **100** 18808-18817

[44] A Doppenschmidt and H Butt 1999 Measuring electrostatic double-layer forces on HOPG at high surface potentials *Colloids and Surfaces* **149** 145-150

[45] M Giesbers, J M Kleijn and M A Stuart 2002 The electrical double layer on gold probed by electrokinetic and surface force measurements *Journal of Collid and Interface Science* **248** 88-95

[46] J Wang and A J Bard 2001 Direct atomic force microscopic determination of surface charge at the gold/electrolyte interface-the inadequacy of classical GCS theory in describing the double layer charge distribution *Journal of Physical Chemistry B* **105** 5217-5222

[47] J G Boyd, D Kim 2006 Nanoscale electrostatic actuators in liquid electrolytes *Journal of Colloid and Interface Science* **301** 542-548

[48] S Timoshenko 1987 *Theory of Plates and Shells* (McGraw Hill, New York)

[49] W H Lin, Y P Zhao 2003 Dynamic behavior of nanoscale electrostatic actuators *Chinese Physics Letters* **20** 2070-2073

[50] M H Bao 2001 Micromechaical transducers: pressure sensors, accelerometers, and gyroscopes *Handbook of Sensors and Actuators* **8** 144-145

[51] H Guckel and D W Burns 1989 Fabrication of micromechanical devices from polysilicon films with smooth surfaces *Sensors and Actuators* **20** 117-122

[52] Y Zhao 2003 Stiction and anti-stiction in mems and nems *Acta Mechanica Solida Sinica* **19** (1): 1-10

[53] M P Boer and T A Michalske 1999 Accurate method for determining adhesion of cantilever beams *Journal of Applied Physics* **86** (2): 817-827

[54] Y Zhao, L S Wang and T X Yu 2003 Mechanics of adhesion in MEMS-a review *Journal of Adhesion Science and Technology* **17** (4): 519-546

[55] W M Spengen and P R Wolf 2002 A physical model to predict stiction in MEMS *Journal of Micromechanics and Microengineering***12** 702-713

[56] C H Mastrangeloo and C H Hsu 1992 A simple experimental technique for the measurement of the work of adhesion of microstructures *IEEE Solid State Sensor and Actuator Workshop* (Hilton Head, USA, June 1992) 208-214

[57] R Maboudian, W R Ashurst and C Carraro 2002 Tribological challenges I micromechanical systems *Tribology Letters* **12** (2): 95-100

VITA

Jae Sang Lee

Permanent address

289-33 Nock-Won A.P.T. 101-1203, Eunhang-Dong, Syheung-Si, Kyong-Ki-Do, Korea 429-836

Email address : aeroalto@gmail.com

Personal

Place of birth: Seoul, Korea

Education

Ph.D   Aerospace Engineering (December 2008)
        Texas A&M University, College Station, TX.

M.S.   Aerospace Engineering (December 2003)
        Texas A&M University, College Station, TX.

B.S.   Aerospace Engineering (February 1998)
        Seoul National University, Seoul, Korea.

Professional Experience

Graduate Research Assistant (Jan. 2003 ~ May. 2008)
SMART Research Group, Texas A&M University, College Station, TX.

MRB Engineer (Jul. 1998 ~ Jul. 2001)
Design Group, Structural Engineering Section, Engineering
Team, Aerospace Division, Korean Air